Norwegian University of
Science and Technology

Design, fabrication and characterisation of silicon nitride nanophotonic biosensor components

Idunn Knain

Master of Science in Electronics

Submission date:	June 2016
Supervisor:	Astrid Aksnes, IET
Co-supervisor:	Jens Høvik, IET
	Kay Gastinger, NTNU Nanolab

Norwegian University of Science and Technology
Department of Electronics and Telecommunications

Problem Description

The purpose of this master thesis is to design, fabricate and characterise nanophotonic components. One part of the thesis is to design and simulate silicon nitride nanophotonic components as part of a (bio)sensor using COMSOL Multiphysics based on finite element method (FEM). A literature study will be done to support the decisions and assumptions done in this work. The literature study is important since it will lay the fundament at NTNU Nanolab for optical components based on a silicon nitride platform.

The waveguide structures designed will be processed in the NTNU Nanolab. To be able to use the equipment, cleanroom courses and training are needed. Methods that will be used which require training beyond the basic clean room and chemical courses are plasma enhanced chemical vapour deposition (PECVD), inductively coupled plasma-reactive ion etching (ICP-RIE), electron beam lithography (EBL) and scanning (transmission) electron microscope (S(T)EM). Since silicon nitride is a relatively new material used for optical structures at NTNU Nanolab, work must be done to optimise the fabrication methods done using silicon nitride.

The fabricated waveguides and components will be optically characterized if time permits. Hopefully, the design and fabrication methods will ensure that the waveguides are in working condition and it is possible to couple light through them. The final part of the thesis is to design a plan for characterisation of the losses in the waveguide structure and assess the optical quality. The optical setup for experimental purposes will be improved and utilised to characterise the waveguide structures produced. Improvements include new laser sources to be added to the setup.

Abstract

This master thesis is dedicated to silicon photonic components; their design, fabrication and characterisation. Waveguides are the fundamental component in the new and exciting field of interferometric biosensors. Their property to confine light and their high sensitivity towards refractive index changes makes them suitable parts of sensitive, miniaturised and fast diagnostic devices. Silicon nitride has been chosen as the core material as it is transparent to the chosen wavelength at 632.8 nm has low losses.

Much work has been done on designing and optimising the waveguide design. The properties behind the various photonics components have been found through simulations done using the finite element method simulation software COMSOL Multiphysics. The optimal dimensions were found to insure single-mode conditions. Propagation and bend losses were estimated as well as coupling between parallel waveguides.

In addition to carrying out simulations of waveguides to minimise losses, experimental characterisation is also needed to validate the performance. Test plans for finding propagation, bend and taper losses were proposed. A paper-clip design was made which is a cut-back method used to characterise propagation loss by measuring waveguides of different lengths. Losses due to side-wall roughness are found by measuring propagation loss depending on waveguide core width.

Fabrication methods for silicon nitride waveguides were investigated and optimised. Equipment used to fabricate the waveguides were plasma enhanced chemical vapour deposition, inductively coupled plasma-reactive ion etching and electron beam lithography. When a coupling test was carried out, it was apparent that the material properties of the silicon nitride and the silicon dioxide resulted in large losses in the waveguide. The etch recipes tried in this thesis gave various etch rates and resulted in anisotropic waveguides with only approximately 90° walls. Sidewall roughness was also observed.

Sammendrag

Denne masteroppgaven er dedikert til silisium fotoniske komponenter, deres design, fabrikasjon og karakterisering. Bølgeledere er de grunnlegende komponentene i det nye og spennende feltet interferometriske biosensorer. Egenskapen å begrense lyset inne i kjernen og den hÃÿye sensitivitet for forandringer i brytningindeks gjør bølgeledere til ideelle komponenter i en sensitiv, miniatyrisert og rask diagnose enhet. Silisium-nitrid var valgt som material i bølgeleder-kjernen i denne oppgaven på grunn av det ”transparent” for den valgte bølgelengden 632.8 nm og har lavt tap.

Mye arbeid er lagt i å designe og optimalisere bølgeleder-designet. Egenskapene til de forskjellige fotoniske komponentene ble funnet ved simuleringer gjort i simulerings programmet COMSOL Multiphysics, som er basert på ” the finite element method”. De optimale dimensjonene ble funnet for å sikre singel-mode betingelser. Forplantning og sving tap ble estimert samt kobling mellom to parallelle bølgeledere.

I tillegg til å utføre simuleringene pÃĕ bølgeledere for å minimalisere tap, er karakterisering også nødvendig for å validere ytelsen. Testplaner for å finne forplantning, sving og ”taper” tap ble foreslått. Et binders-design ble laget. Dette er en ”cutback”, skjære tilbake, metode hvor man måler forplantnings tapet i bølgeledere av forskjellig lengde. Tap som er på grunn av ruhet i sideveggene er funnet ved å måle forplantningstapet i bølgeledere av forskjellige bredder.

Fabrikasjons metoder for silisium nitrid bølgeledere ble undersøkt og optimalisert. Utstyret som ble brukt til å fabrikkere disse var ”plasma enhanced chemical vapour deposition”, ”inductively coupled plasma-reactive ion etching” og ”electron beam lithography”. Da en koplingstest ble utført, var det klart at material egenskapene til silisium-nitridet og silisium-oksidet resulterte i store tap i bølgelederne. Etseoppskriftene brukt gav forskjellige etsehastigheter og de resulterte i anisotropiske bølgeledere men veggene er ikke eksakt 90°. Mye sideveggsruhet ble også observert.

Preface

This master thesis will contain a detailed description and the results from the work done as part of the degree MSc in Electronics at the Department of Electronics and Telecommunications at the Norwegian University of Science and Technology (NTNU). Prior to this master thesis, project work was done on designing and simulating a grating coupler in COMSOL Multiphysics. The skills learned from this experience are utilised in this work to further design and simulate other silicon nanophotonic components and fabricate them. The experimental work and this text is the individual work of the author. Work not done by the author will be credited to the rightful individual.

Acknowledgement

I would like to thank professor Astrid Aksnes for being a great supervisor who has both challenged me and helped me through the tough days. Her guidance and feedback has been very helpful and I have learnt a lot from the experience. Further, I would like to thank Jens Høvik for his help with both COMSOL and in the NTNU Nanolab. He also has done a great job working on the optical experimental setup. Kay Gastinger also deserves a big thanks for his insight at the NTNU Nanolab and his in-depth questions and interest along the way.

Various NTNU Nanolab engineers have also been helpful on not only giving the training needed on the equipment, but also giving advise and arrange chemical-courses just for our group since some of us had not worked much with chemistry before. Birgitte McDonagh and Mark Chiappa were always happy to help whenever I was stuck or just needed some advice. The Research Council of Norway is acknowledged for the support to the Norwegian Micro- and Nano-Fabrication Facility, NorFab. Last, but not least I would like to thank the rest of the MSc students Morten Hage, Magnus Mariero and Lars Grønmark Holmen for all the discussions and sharing of experiences we have done. It made this very fun and enjoyable having so many friendly and caring people around me.

Contents

Contents **1**

List of Figures **4**

List of Tables **8**

1 Introduction **11**

2 Theory **15**
2.1 Maxwell's equations . . . 15
2.1.1 The transverse electromagnetic plane wave . . . 16
2.1.2 Boundary conditions . . . 17
2.1.3 Polarization . . . 18
2.2 Waveguides . . . 18
2.2.1 Waveguide modes . . . 21
2.2.2 Optical loss in waveguides . . . 21
2.2.3 Silicon-on-insulator . . . 23
2.2.4 Silicon nitride . . . 24
2.2.5 Coupling to waveguides . . . 25
2.2.6 Coupling techniques . . . 26
2.2.7 Tapered coupling . . . 27
2.2.8 Grating coupling . . . 27
2.2.9 Floquet theory . . . 29

3 Methods and Tools **31**
3.1 Simulations in COMSOL . . . 31
3.1.1 Simulation methods . . . 31
3.2 Waveguide characterisation methods . . . 35
3.2.1 The cut-back method . . . 35
3.2.2 Alternative methods for measuring loss in waveguides . . . 36
3.2.3 Propagation loss due to waveguide dimension reduction . . . 36
3.3 Fabrication equipment and processes . . . 37

3.3.1 Plasma enhanced chemical vapour deposition 37
3.3.2 Inductively coupled plasma- reactive ion etching 38
3.3.3 Electron beam lithography 38
3.3.4 Scriber 42
3.4 Characterisation equipment 42
3.4.1 Scanning (transmission) electron microscope 42
3.4.2 Reflectometer 43
3.5 Experimental setup 45

4 Design and simulation 49
4.1 Waveguide design 49
4.2 Test structure design 51
4.2.1 Taper design 54
4.2.2 Propagation loss measurements in bends 56
4.3 Mask design 57
4.4 Grating coupler 61
4.4.1 Grating coupler simulations 61

5 Fabrication Process 65
5.1 Fabrication process 66

6 Results and Discussion 71
6.1 COMSOL simulations 71
6.1.1 Waveguide design and propagation loss simulations 71
6.1.2 Dimensions 72
6.1.3 Fabrication effects on a fully etched slot grating coupler . . . 73
6.2 Processes and fabrication 78
6.2.1 Silicon dioxide deposition 78
6.2.2 Silicon nitride deposition 80
6.2.3 Electron beam lithography procedure 82
6.2.4 Etching procedure 84
6.3 Characterisation and coupling 88

7 Conclusions 91
7.1 Future work 92

Bibliography 95

A PECVD recipes 101

B ICP-RIE recipes 103

C Sample fabrication summary **105**

D COMSOL models **107**
D.1 Waveguide cross-section simulation 107
D.2 Waveguide simulation with effective index 113

List of Figures

2.1 Wavefronts 17
2.2 The three main types of channel waveguides 19
2.3 A guided ray in a symmetric waveguide and the $\vec{k}$ vector diagram. . 20
2.4 The field distributions for TE guided modes in a dielectric waveguide, from p. 254 [1]. 22
2.5 The ranges of attenuation coefficients of SiO_2 single-mode and multimode fibres, from p. 298 [1]. 23
2.6 Examples of defects in a structure that may result in propagation losses by diffusion, from p. 74 [2]. 24
2.7 A illustration of a silicon-on-insulator (SOI) structure. 25
2.8 A prism coupler, where the phase matching condition is: $\beta_m \approx \beta_{prism} = n_p k_0 \sin\theta_p$, from p. 587 [3]. 26
2.9 A typical taper design, where θ is the local half angle. 27
2.10 An illustration of part of a typical grating coupler where G is the grating period and w the duty cycle [4]. 27
2.11 A typical experimental setup for grating coupling between a SOI waveguide and an optical fibre, from p. 5 [5]. 28

3.1 An illustration of how the geometry is divided into sections and the "Surface Integration" function found in COMSOL. 32
3.2 A cross-section waveguide mesh with a predefined "Physics-controlled mesh". 34
3.3 An illustration of a waveguide shaped as a paper-clip. 36
3.4 An illustration of the PECVD machine [6]. 37
3.5 An illustration of the ICP-RIE machine [7]. 39
3.6 A schematic diagram of an EBL, [8]. 40
3.7 Spin curves: the resist thickness dependence on the spin speed for the CSAR 6200(.4, .9 and .13) [9]. 41
3.8 An illustration of the physical process in the S(T)EM, [10]. 43
3.9 An illustration of the mechanism and parts in the S(T)EM, [11]. . 44
3.10 An illustration of the experimental optical setup. 46

4.1 Mode plot of the first 6 modes with a silicon nitride (Si_3N_4) core of 200 nm x 500 nm. 50
4.2 An illustration of two waveguides with different physical lengths but the same distance between input and output. 52
4.3 The paper-clips dimensions. x is half of the length of the short straight waveguide and y is the bend-radius. 53
4.4 A waveguide with a bend with 35 μm bend radius. The bend is 180° and the waveguide dimensions are 200 nm x 500 nm. 53
4.5 An illustration of a tapered waveguide. First, there is an input-waveguide before it narrows slowly down at an angle θ to the height of the main waveguide core. 55
4.6 A clipping of a taper at the beginning of a waveguide. The white part is the waveguide and the green part on the sides are the 8 μm wide exposed area. 57
4.7 The paper-clip tapered mask created in Clewin 4. 58
4.8 The taper test-mask created in Clewin 4. 59
4.9 The bends loss test-mask created in Clewin 4. 60
4.10 One grating period of the proposed grating. 62
4.11 The study space for the simulation of the finite grating. 63

5.1 Silicon dioxide (SiO_2) PECVD deposition on top of a 500 μm thick silicon wafer. The SiO_2 is 2 μm thick. Not to scale. 66
5.2 Si_3N_4 PECVD deposition on top of the 2 μm thick SiO_2 film. The Si_3N_4 is 200 nm thick. Not to scale. 67
5.3 Some of the steps in the EBL and etch process, not to scale. 69

6.1 The third mode, showing that two modes are guided in the core, for a waveguide with dimensions 200 nm $\times$ 600 nm. 73
6.2 A graphic of the simulated gratings normalised E-field. 74
6.3 Free space wavelength dependence on duty cycle. The total duty cycle shift is $\pm$ 5% 75
6.4 Free space wavelength dependence on incident angle. 76
6.5 Plot of incident angle vs. the wavelength in free space when the duty cycle is 5% smaller than original design duty cycle of 535.52 nm. 76
6.6 Duty cycle vs. the percentage of light coupled from the waveguide to the fibre. 77
6.7 A cross-section picture of sample 1. The sample here is shown upside down with the SiO_2 film on the top and the Si_3N_4 film at the bottom. 79
6.8 A S(T)EM photo of the cross section of a 200 nm Si_3N_4 layer on top of a silicon wafer, sample 8. 81

6.9 A S(T)EM photo of sample 1, a waveguide with a bend radius of 35 μm. . . . 82
6.10 S(T)EM picture of sample 1 and sample 6 showing a section of the waveguide. . . . 83
6.11 A S(T)EM photo of sample 6, a close up of the dirty spots found in the exposed areas next to the waveguide. . . . 83
6.12 An atomic-force microscopy (AFM) photo of sample 2 showing the taper and part of the main waveguide. The height of the waveguide was found to be 183 nm. . . . 84
6.13 Cross-section S(T)EM photos of samples 1 and 8. . . . 85
6.14 A S(T)EM photo where charge effects can be seen. . . . 86
6.15 Photos of sample 8 taken with an optical microscope and photos of the broken waveguides taken in S(T)EM. . . . 87
6.16 Direct fibre coupling configuration. . . . 88
6.17 The sample holder. . . . 89
6.18 The coupling achieved into the rib waveguide. . . . 90

C.1 A summary of the samples further investigated. Approx. means that the reflectometer was not able to measure accurately when having both SiO_2 and Si_3N_4 layers on top of the silicon wafer. (*) No SiO_2 layer on these samples. . . . 106

D.1 ”New Model” menu and how to choose dimensions, physics model and type of study. . . . 108
D.2 ”Model builder”. . . . 109
D.3 Geometry settings and material settings for air. . . . 109
D.4 The entire geometry for the waveguide cross-section and the air domains. . . . 110
D.5 The entire geometry for the waveguide cross-section and the air domains. . . . 111
D.6 The mesh created with user settings. . . . 112
D.7 The setting for the two rectangles *Waveguide* and *Port* defined under ”Geometry”. . . . 114
D.8 The complete ”Geometry” of the waveguide seen from above. . . . 114
D.9 The ”Material” menu in the ”Model Builder” showing the two material names for this model. . . . 114
D.10 An illustration of where *Port1* is defined. . . . 115
D.11 The grey domains are areas not included in the simulation because the ports need to be defined at the simulation boundary. . . . 115
D.12 ”Model builder” for ”Mesh”, ”Study” and ”Result”. . . . 116

D.13 The ”Size” settings, ”Study” entry in ”Model Builder” and the settings for ”Boundary Mode Analysis” *Port1*. 117

List of Tables

3.1 The refractive indices in the different regions. 33
3.2 List of equipment comprising the optical characterisation setup . . . 47

4.1 The actual waveguide length with bends. The length from input to output is kept at 1 cm for all waveguides. The various widths investigated to find the loss due to side-wall roughness are also presented. 51
4.2 The power ratio between the input and the output port is presented. 1 = 100 % transmission. The results are from COMSOL "Derived values" when performing a parametric sweep over the bend-radius's listed. 52
4.3 The percentage of power coupled out at the output of the second waveguide when light is coupled into waveguide number one. 1 = 100% 54
4.4 The various lengths of the taper (T) and the input-waveguide (In-W) ensure that the angles and the waveguide (W) and sample lengths are constant. The lengths are found using equation 4.2.2 with factor 200 instead of 500. 55
4.5 The taper-test lengths and the input-waveguide lengths when the main waveguide is 4 mm long and 450 nm wide. The lengths are found using equation 4.2.2 with *factor* instead of 500. 56
4.6 The various bend radiuses which will be used in a bend-loss measurement. 56
4.7 The taper, input-waveguide and waveguide length for each width with a *factor* of 300. 58

5.1 List of chemicals used in the NTNU Nanolab. 67
5.2 Steps included in the pattering of the sample presented as a recipe. 68

6.1 The "Surface Integrals" ($\iint$) of the electric field distribution in each region of the waveguide as shown in figure 3.1b. The dimensions are 200 nm x 500 nm, height and width respectively. The unit is $\frac{kg^2 \times m^4}{(s^6 \times A^2)}$. 72

6.2 Growth times and the thicknesses of SiO_2 measured by the reflectometer. The thickness is measured at the centre of the sample and the number in the parenthesis is the thickness measured towards the edge of the sample. 78
6.3 Growth times and the thickness of Si_3N_4. 80
6.4 Description of samples investigated in the coupling experiments. . . 89

A.1 Basic silicon dioxide PECVD process by Oxford Instruments, PLASMALAB SYSTEM 100: *Process data sheet* found 101
A.2 Improved uniformity/high quality silicon nitride PECVD process by Oxford Instruments, PLASMALAB SYSTEM 100: *Process data sheet* 101

B.1 The etch recipes used in this thesis. Taken from the recipe database on the ICP-RIE computer. OI stands for Oxford Instruments. . . . 103

D.1 Parameters for the cross section of a waveguide with SiO_2 cladding and a core of Si_3N_4. 108
D.2 The parameters entered in COMSOL for the waveguide simulation. 113

Chapter 1

Introduction

Photonics was first used as a term comprising technologies and sciences using, creating and modifying light in the 1960s. Some well known applications are LEDs, lasers and solar-panels. With the speed of light, light enables fast information transport through fibres and other optical systems. Other applications might use photons to create energy or gather specific information when a photon interacts with a material. New applications are being created rapidly. Photonics is one of the six Key Enabling Technologies (KETs), which means that it is one of the technologies thought to provide the basis of innovation in a range of products across all industrial sectors [12]. The European Commission believes that countries and regions managing to ”fully exploits KETs will be at the forefront of creating advanced and sustainable economies” [12].

Photonics has proven to be very promising for the medical field. It creates a more efficient and safer way to diagnose, perform surgery or do non-invasive imaging. An application which is portable, easy-to-use and highly sensitive can therefore enable real-time diagnostics for more accurate cures, faster initiation of treatment and shorten the time patients might infect others around them. Photonics can be integrated into biosensors, which are analytical devices that comprise a biological material either retained or immobilised at the sensor surface. These devices provide a quantitative and specific response in the presence of an analyte. Some advantages from miniaturisation of biosensors are fast responses, low cost, improved signal to noise and surface-volume.

In the past six decades, microelectronics has been at the forefront of the modern information revolution. The electronic industry is driven to become faster and more complex, and at the same time using smaller and smaller components. These components are also expected to run at lower and lower energy levels and require less power. ”Recent progress in silicon compatible photonics is driving high density

integration of photonic and electronic components manufactured by complementary metal-oxide-semiconductor (CMOS)-based technology on the same platform" [13]. The physical limitations of metallic interconnections is tried to be overcome by merging electronics and photonics, as photonics can transfer optical data at a higher rate than metal wiring. The information lies in the light being passed through systems such as a laser, waveguide, modulator or photodetecor. The silicon photonics industry has low processing costs and silicon wafers is of higher quality than other semiconductor materials.

A photonic biosensor has the potential to offer reliable, sensitive and miniaturised diagnostics as well as all the other advantages of biosensors mentioned earlier. To make diagnostics independent of skilled personnel, large technical equipment and time, a photonic biosensor can be incorporated on a chip, and can then be called a lab-on-a-chip application. Other lab-on-a-chip applications are environmental monitoring and food industry, veterinary and industrial process control. In the past three decades, photonic sensors using refractive index measurements have been extensively researched but not many products are yet commercially available. When a sensor surface is covered by an immobilised analyte selectively captured by a bio-recognition agent, the refractive index in the sensor will change. This makes it possible, among other things, to detect changes in the transmitted light. It is stated in Gonzalez et al. (2011) [14], that interferometry is found to have a broader dynamic range and higher sensitivity compared to other label-free measurements.

An interferometric biosensor, which uses waveguide structures such as Mach-Zehnder Interferometers or Ring-Resonators, is therefore an interesting and promising device to investigate. Waveguides guide the light by confining it in the core which has a higher refractive index than the cladding material. One difference between electronics and photonics is that generally, photonics require more process steps than electronics, where some components can be produced in parallel resulting in a single integrated platform. Therefore, it is important to create fabrication techniques which are reliable, accurate and reproducible. This thesis will optimise designs and fabrication processes of waveguides which are the basic and fundamental components of this sensor.

The chosen materials in this thesis are silicon (wafer), silicon oxide (cladding) and silicon nitride (core). In telecommunications, wavelengths typically used are 1310–1550 nm and for these wavelengths silicon has been the selected material of the waveguide core. This material combination is called silicon-on-insulator (SOI) and is a common material structure used for optical sensors integrated on chips.

However, it is found that silicon nitride is more compatible with visible and near-infra-red wavelengths which are more suitable for biological applications. Silicon nitride (Si_3N_4) is transparent to visible and near-infra-red wavelengths, compared to infra-red (IR)-light which is absorbed by the water molecules in biomaterials. Dhakal et al. (2014) [15] stated that using Si_3N_4 will enable Raman spectroscopy and fluorescence spectroscopy.

This thesis will further investigate photonic components which are to be part of a nanophotonic biosensor. The design, fabrication and characterisation methods will be optimised. The author of this thesis has no previous experience or knowledge about the NTNU Nanolab facility and the fabrication methods used. As a result, the first few months were used to become familiarised with the equipment and processes needed to fabricate waveguides in silicon nitride. Methods fabricating SOI waveguides have been investigated in previous work by other cleanroom users, but silicon nitride has not been used extensively for optical components. Therefore, the processes involving silicon nitride needed to be developed and optimised.

First, the theory behind photonic waveguides and other relevant information needed is presented in chapter 2. Chapter 3 will explain the methods and tools used by the author to perform the work done. A chapter is designated to the waveguide design, chapter 4, which is done by simulating the components in COMSOL Multiphysics and performing a literature study. The author of this thesis has experience using this simulation tool through the work done in the project thesis [16]. Further, chapter 5 describes the fabrication process done by the author in details. The discussion of the results are made simultaneously as presenting them, because it resulted in a better flow in the thesis. This is presented in chapter 6 and a short conclusion to summarise it all up is found in chapter 7. The work done in this thesis will hopefully prove helpful to future master students interested in this exciting field or others fascinated with this topic.

Chapter 2

Theory

In this section, an overview of the theory needed to be able to understand an optical wavgeuide and to describe and design a grating coupler will be presented. First, we need to look at some electromagnetic principles, then go into more detail about waveguides and characteristics of a grating coupler. Much of the theory presented here can be found in [1]. Section 2.1 and parts of section 2.2 (2.2.1, 2.2.3, 2.2.5,2.2.6, 2.2.8 and 2.2.9) are taken from the project thesis [16] with a few changes.

2.1 Maxwell's equations

To look at grating coupler from an electromagnetic perspective, we need Maxwell's equations. According to classical theory, light is the flow of electromagnetic radiation through a medium or free space. How an electromagnetic wave propagates as a wave through a medium or vacuum is described by a set of differential equations. In the case of monochromatic electromagnetic waves in an optical medium, the electric and magnetic field takes the form of harmonic functions and are characterised by their angular frequency. The fields are expressed as

$$\vec{E}(\vec{r},t) = \vec{E}_0(\vec{r}) cos(\omega t + \phi(\vec{r})) \tag{2.1.1}$$

$$\vec{H}(\vec{r},t) = \vec{H}_0(\vec{r}) cos(\omega t + \phi(\vec{r})) \tag{2.1.2}$$

where $\vec{E}_0$ and $\vec{H}_0$ represent the electric- and magnetic field amplitudes, respectively. The fields are also described in terms of displacement $\vec{r}$, angular frequency ω and the phase $\phi(\vec{r})$.

Maxwell Equation's for a monochromatic field in a source-free medium

$$\nabla \times \vec{E} = -j\omega\vec{B} \tag{2.1.3}$$

$$\nabla \times \vec{H} = j\omega\vec{D} \tag{2.1.4}$$

$$\nabla \cdot \vec{D} = 0 \tag{2.1.5}$$

$$\nabla \cdot \vec{B} = 0 \tag{2.1.6}$$

We also have that

$$\vec{D} = \varepsilon_0\vec{E} + \vec{P} \tag{2.1.7}$$

$$\vec{B} = \mu_0(\vec{H} + \vec{M}) \tag{2.1.8}$$

ε represents the dielectric permittivity and μ is the magnetic permeability. The vector $\vec{B}$ is the magnetic flux density, $\vec{D}$ is the electric flux density, $\vec{P}$ is the polarization density and finally $\vec{M}$ is the magnetization density.
In a linear, non-dispersive, homogeneous and isotropic media, equations 2.1.7 and 2.1.8 become $\vec{D} = \varepsilon\vec{E}$ and $\vec{B} = \mu\vec{H}$, respectively. By using these relations and equations 2.1.1 and 2.1.2 we obtain these four equations

Maxwell Equation's for monochromatic light in a linear, non-dispersive, homogeneous and isotropic source free medium

$$\nabla \times \vec{E} = -j\omega\mu\vec{H} \tag{2.1.9}$$

$$\nabla \times \vec{H} = j\omega\varepsilon\vec{E} \tag{2.1.10}$$

$$\nabla \cdot \vec{E} = 0 \tag{2.1.11}$$

$$\nabla \cdot \vec{H} = 0 \tag{2.1.12}$$

2.1.1 The transverse electromagnetic plane wave

Transverse electromagnetic (TEM) waves are used to help describe the modes in a waveguide. A TEM plane wave is a monochromatic electromagnetic wave with electric- and magnetic field complex-amplitude vectors:

$$\vec{H}(\vec{r}) = \vec{H}_0 e^{-j\vec{k}\cdot\vec{r}} \tag{2.1.13}$$

$$\vec{E}(\vec{r}) = \vec{E}_0 e^{-j\vec{k}\cdot\vec{r}} \tag{2.1.14}$$

Providing the magnitude of the wave vector $\vec{k}$ is $k = nk_0$, where n is the refractive index (RI), the components of $\vec{H}(r)$ and $\vec{E}(r)$ satisfy Helmholtz equation. Helmholtz equation is a time-independent form of the wave equation

$$\nabla^2 U + k^2 U = 0 \tag{2.1.15}$$

where k is defined as $nk_0 = \omega\sqrt{\varepsilon\mu} = \frac{w}{c}$ and U represents the complex amplitude of either a component of $\vec{E}$ or $\vec{H}$. By substituting equations 2.1.14 and 2.1.13 into Maxwell's relations we see that:

$$\vec{k} \times \vec{H}_0 = -\omega\varepsilon\vec{E}_0 \tag{2.1.16}$$

$$\vec{k} \times \vec{E}_0 = \omega\mu\vec{H}_0 \tag{2.1.17}$$

A wave is a TEM wave if $\vec{E}$ is perpendicular to $\vec{H}$ and $\vec{k}$, which leads to $\vec{H}$ being perpendicular to $\vec{E}$ and $\vec{k}$. All of this gives us a wave that has a wave-front normal to the wave-vector $\vec{k}$, se fig 2.1.

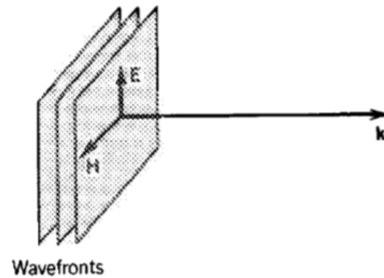

Figure 2.1: Wavefront. from p. 170 [1].

2.1.2 Boundary conditions

Boundary conditions are needed to determine the reflectance and transmittance of waves at the boundaries and the propagation of waves in different structures, like the waveguide. The tangential components of the electric and the magnetic fields must be continuous in the case of an absence of free electric charge and currents. This also leads to that the normal components of the electric and magnetic flux

densities must be continuous at the boundary between two media.

$$E_1 t = E_2 t \tag{2.1.18}$$

$$H_1 t = H_2 t \tag{2.1.19}$$

$$D_1 n = D_2 n \tag{2.1.20}$$

$$B_1 n = B_2 n \tag{2.1.21}$$

2.1.3 Polarization

Polarization is important when looking at how light interacts with matter. How the light is reflected at boundaries and absorbed in different media, is dependent on polarization. It is also important for how light scatters from matter and the refractive index of anisotropic materials depends on the polarization. The magnetic- and electric fields are perpendicular to the propagation direction, and will therefore only have components in the x and y directions. The electric field can be expressed as

$$\vec{E}(z,t) = \mathrm{Re}\{\vec{J}e^{j\omega t - j\beta z}\} \tag{2.1.22}$$

where the Jones vector is defined as:

$$\vec{J} = A_x\hat{x} + A_y\hat{y} \tag{2.1.23}$$

The Jones vector can describe linear, circular and elliptic polarization depending on the coefficients. An optical system is described by a transfer matrix, **T**, so we can express the light transmitted as $\vec{J_2} = T \cdot \vec{J_1}$. When light moves from one media to another, the amount of light being reflected or refracted is described by Fresnel equations. What happens, depends on how the electric field ad magnetic field are oriented. For a transverse electric (TE) wave, if the wave is propagating in the $\hat{z}$ direction, there will be no electric field $\vec{E} = E\hat{x}$ in the direction of propagation. For a transverse magnetic (TM) wave, $\vec{H} = H\hat{x}$, there is no magnetic field in the propagation direction.

2.2 Waveguides

There are two types of waveguides, mirrored and dielectric waveguides. In this report, we are only considering a dielectric waveguide. A dielectric waveguide is an optical structure that has the ability to confine light within its boundaries by total internal reflection. Total internal reflection happens when the angle of incidence at the boundaries is smaller than the critical angle, $\theta_c = \frac{\pi}{2} - \sin^{-1}(\frac{n_2}{n_1})$

where n_1 is the refractive index (RI) in the core and n_2 is the RI in the cladding. This shows that the critical angle depends on the RI of the two materials. Total internal reflection is possible when a high RI material is surrounded by a material with a lower RI. One will get a better confinement factor with a larger difference in refractive index. The confinement factor is the ratio between the power in the core and the total power. When the light is confined in two dimensions, it is called a channel waveguide or 2D waveguide. Three types of channel waveguides are shown in figure 2.2. A fibre is a waveguide with a circular core and cladding around it.

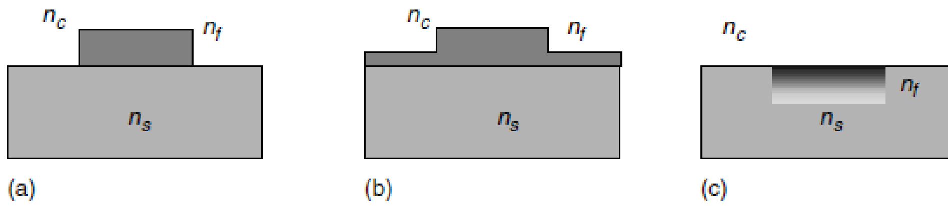

Figure 2.2: The three main types of channel waveguides: (a) stripe waveguide, (b) rib waveguide, (c) buried waveguide, from p. 57 [17]. The dark grey area is what is referred to as the core

In a waveguide where light is confined inside the core, see figure 2.3a, there is a certain amount of modes that are allowed to propagate. From the $\vec{k}$ diagram in 2.3b, we get that the z components are the propagation constants

$$\beta_m = n_1 k_0 \cos\theta_m \tag{2.2.1}$$

where $\cos\theta_m$ lies between 1 and $\cos\theta_c$, where $\theta_c = \cos^{-1}\frac{n_2}{n_1}$. The relationship between the width of the core d and number of modes allowed to propagate is

$$M \doteq \frac{2d\sin\theta_c}{\lambda} \tag{2.2.2}$$

where $\lambda = \frac{\lambda_0}{n_1}$ and $\doteq$ means that the result is rounded up to the nearest integer. $NA = n_1 \sin\theta_c$ is called the numerical aperture and is known as the acceptance cone. The numerical aperture is defined as

$$NA = \sqrt{n_1^2 - n_2^2} \tag{2.2.3}$$

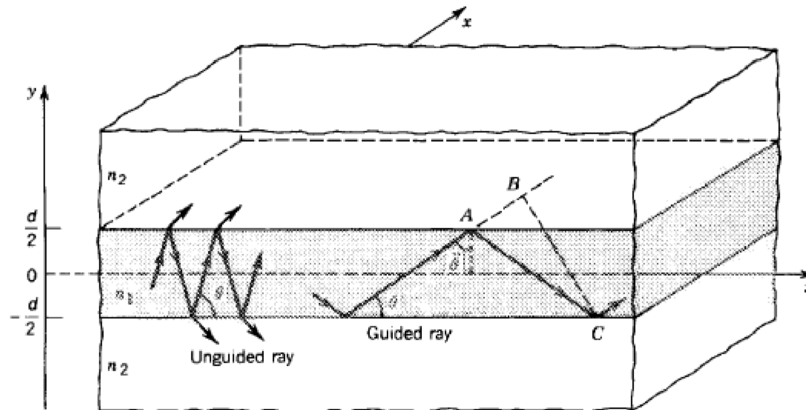

(a) Guided ray in a symmetric waveguide, the guided ray is confined within the core, from p. 249 [1].

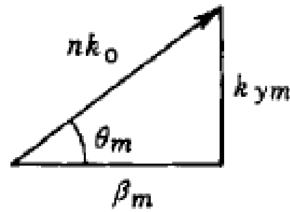

(b) The $\vec{k}$ vector diagram for the propagation in core, k_0 is the wave vector for the planar wave and β_m is the propagation constant for the guided mode, from p. 243 [1].

Figure 2.3: A guided ray in a symmetric waveguide and the $\vec{k}$ vector diagram.

2.2.1 Waveguide modes

To find the field distributions, the field inside the core is said to consist of two TEM plane waves travelling with an angle of θ_m and $-\theta_m$. Since they have the same amplitude and phase shift, the electric-field complex amplitude is therefore

$$E_x(y,z) = a_m u_m(y) e^{-j\beta z} \tag{2.2.4}$$

where a_m is a constant and

$$u_m(y) \propto \begin{cases} \cos(k_y y), & m = 0,2,4,... \\ \sin(k_y y), & m = 1,3,5,... \end{cases} -\frac{d}{2} \leq y \leq \frac{d}{2}$$

where $k_y = \frac{2\pi \sin\theta_m}{\lambda}$. The field in the cladding needs to match the internal field at $y = \pm\frac{d}{2}$, so we need to take into consideration the boundary conditions mentioned in section 2.1.2. The wave in the top and bottom cladding will decay exponentially and are expressed as

$$u_m(y) \propto \begin{cases} e^{-\gamma_m y}, & m = 0,2,4,... \qquad y > \frac{d}{2} \\ e^{\gamma_m y}, & m = 1,3,5,... \qquad y < -\frac{d}{2} \end{cases}$$

By substituting equation 2.2.4 into Helmholtz equation 2.1.15, we get an equation for the core

$$[\frac{d^2}{dy^2} + (k_0^2 n_1^2 - \beta_m^2)]u_m(y) = 0 \tag{2.2.5}$$

and in the cladding we get

$$[\frac{d^2}{dy^2} + (k_0^2 n_2^2 - \beta_m^2)]u_m(y) = 0 \tag{2.2.6}$$

where $(\beta_m^2 - k_0^2 n_2^2) = \gamma_m$ and γ_m is known as the extinction coefficient. The relationship between the angular frequency ω and the propagation constant β_m is called the dispersion relation. From the dispersion relation we can find information about the phase velocity and the group velocity. The mode field distribution of a guided TE mode is shown in figure 2.4. The TM modes are found in a similar way with the magnetic field in the x-direction, H_x(y,z).

2.2.2 Optical loss in waveguides

Light propagating in a waveguide will experience attenuation and loss as it travels in the waveguide. Depending on the material, light of certain wavelengths can be absorbed, radiated or scattered and the light will be exponentially attenuated as

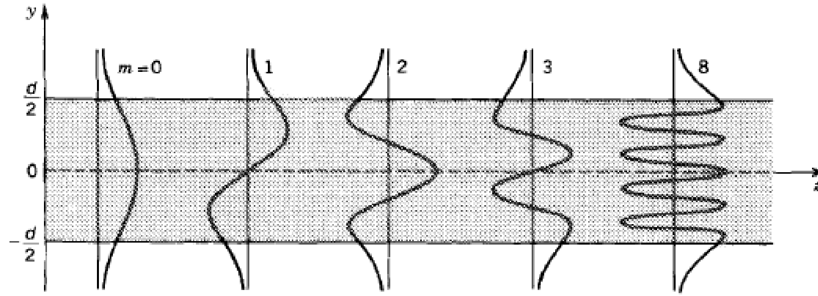

Figure 2.4: The field distributions for TE guided modes in a dielectric waveguide, from p. 254 [1].

it moves through the waveguide resulting in a decrease in power. The attenuation coefficient is a summation of the propagation loss in the waveguide and is defined as

$$\alpha = \frac{1}{L} 10 \log_{10} \frac{P(L)}{P(0)} \tag{2.2.7}$$

where L is the length of the waveguide and P is the power. The attenuation is typically measured as decibel per centimetre $\frac{dB}{cm}$. The resulting power is therefore

$$P = P_0 e^{-\alpha z} \tag{2.2.8}$$

where $P(0)$ is the initial power. Interaction between light and the medium leads to energy transfer which can be elastic or inelastic. Material absorption is an inelastic effect where the energy of the wave is not conserved but transferred to the surrounding medium. The material absorption is dependent on frequency as materials has different transparency windows due to bonds and charges present in the material, [18].

One of the largest losses occurs at the interface between the cladding and the core. This is mainly due to side-wall roughness caused by poor fabrication which results in large scattering. The contribution of such a loss is numerically described in Grillot et al. (2004) [19]. Scattering losses increase with increasing index contrast as Δn^4, Melloni et al. (2009) [20]. Waveguides with small index contrast, typically $\Delta n = 0.01$, have very low losses, a large mode area, low birefringence and are repeatable, reliable and stable in time. One disadvantage with decrease in index contrast is that the minimum achievable bend radius get quite large, as there will be a high amount of loss due to radiation. Radiation depends on light confinement and bend radius. With higher index contrast, the dimensions becomes smaller and

the integration on circuits gets easier. The bend radius is minimum 30μm for silicon nitride strip waveguides found in Melloni et al. (2009) [20]. There is also a loss in power when coupling light from one mode to another. Coupling between a single-mode fibre to a waveguide is explained in section 2.2.5.

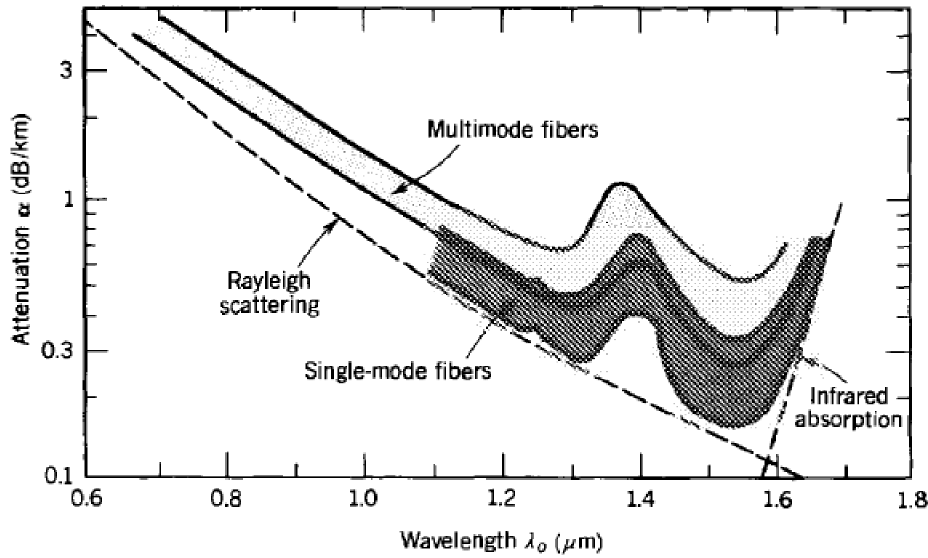

Figure 2.5: The ranges of attenuation coefficients of SiO_2 single-mode and multimode fibres, from p. 298 [1].

In fused silica glass (SiO2), there are two strong absorption bands. Vibrational transition results in a middle IR absorption band and an ultraviolet absorption band is caused by electronic and molecular transitions. These two bands combined give a window in the near-IR region where there is a low absorption coefficient resulting in essentially no intrinsic absorption, see figure 2.6. Another effect that contributes to the attenuation of light in glass is Rayleigh scattering. This is an intrinsic effect where there are random localised scattering points because of variations of the molecular positions and imperfections which give rise to inhomogeneities of the refractive index.

2.2.3 Silicon-on-insulator

Silicon is almost transparent to near-IR wavelengths and has therefore a low absorption loss in this region. Wavelengths such as 1310 and 1550 nm are typically

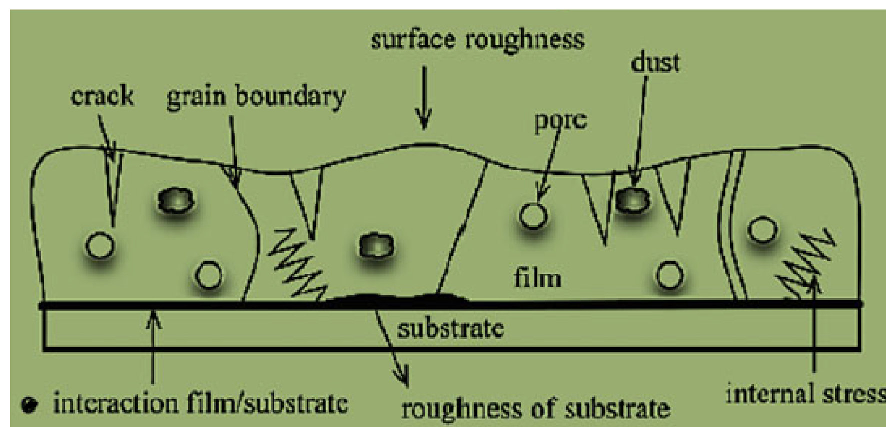

Figure 2.6: Examples of defects in a structure that may result in propagation losses by diffusion, from p. 74 [2].

used in telecommunications, so silicon is a very promising material for efficient communication. Since the RI contrast between silicon (n = 3.47) and silicon dioxide (SiO_2) (n = 1.45) is fairly high, it provides a strong confinement of the light. Silicon is highly compatible with integrated circuit manufacturing processes, so it is possible to use well known and developed fabrication techniques. It is shown in Bogaerts (2005) [21], that advanced CMOS technology is capable of fabrication of nanophotonic structures.

A dielectric waveguide can be a silicon-on-insulator (SOI). This means that the waveguide consists of a silion layer ($n_1 = 3.47$) on top of a cladding of silicon dioxide ($n_2 = 1.45$), see figure 2.7. The top layer is air, but it is also common to have a symmetric waveguide with a silicon dioxide layer as the top layer. To have little propagation loss and to avoid mode mismatch when coupling to other single-mode structures, the thickness of the silicon core has to be sufficiently small to only support a single-mode. We can see from equation 2.2.2 that the number of modes is dependent on the width of the core. The SOI waveguide dimensions should be small enough to be able to be integrated on a chip.

2.2.4 Silicon nitride

Nitrides are known to be hard and wear resistant, they also have high melting points and good chemical resistance, Pierson (1999) [22]. Silicon nitride (Si_3N_4) is light-weight, has high electrical resistivity and good resistance to oxidation up to 1500 °C. It is a dielectric material which can be used as insulation and passivation.

Figure 2.7: A illustration of a SOI structure.

Si_3N_4 is typically used as cutting tools, engine moving- and wear-parts and shaping tools. Silicon nitride is also used in biophotonic and optofluidic biochemical applications since it is transparent in the visible and near-IR regions, Goykhman et al. (2010) [23] and Wang et al. (2015) [24]. It can be deposited using sputtering or chemical vapour deposition (CVD) processes, commonly either with low-pressure chemical vapour deposition (LPCVD) or PECVD. A typical structure used in the integrated circuit industry is silicon wafer with a cladding of SiO_2.

2.2.5 Coupling to waveguides

To be able to excite a mode in the waveguide, the field distribution of the source need to match the specific mode of the waveguide. If two waveguides are brought into close proximity to one another, they can exchange power. A superposition of the modes makes it possible to express the complex amplitude of the optical field as

$$E(y,z) = \sum_m a_m u_m(y) e^{-j\beta_m z} \tag{2.2.9}$$

At the boundary between the source distribution ($s(y)$) and the mode distribution, the boundary conditions give rise to a mode matching condition at the interface

and this results in

$$\int_{-\infty}^{\infty} u_m u_n dy = \begin{cases} 1, & m = n \\ 0, & m \neq n \end{cases}$$

where u_n is the transverse distribution of the source. The degree of correlation between the two distributions is expressed as

$$a_n(z=0) = \int_{-\infty}^{\infty} s(y)u_n(y)dy = \sum_m a_m e^{-j\beta_m \cdot 0} \int_{-\infty}^{\infty} u_m u_n dy \tag{2.2.10}$$

2.2.6 Coupling techniques

The radiation mode for a laser beam cannot propagate directly into a waveguide. The spot-size of a single-mode fibre compared to a waveguide is very large. For an air to waveguide setup, the phase matching condition $\beta_m = kn_{air}\sin\theta_i$, where k is the incident wavevector, cannot be satisfied since the axial component of the wavevector of the incident beam is too small to match the propagation constant of the mode. There are different techniques that make the propagation of guided-modes through the waveguide possible, these techniques confine and couple the laser beam with the waveguide. Some examples are prism coupler, end coupler, launch coupler, tapered coupler and grating coupler. For a description of these techniques, see Tong (2014) [2]. A prism coupler is illustrated in figure 2.8.

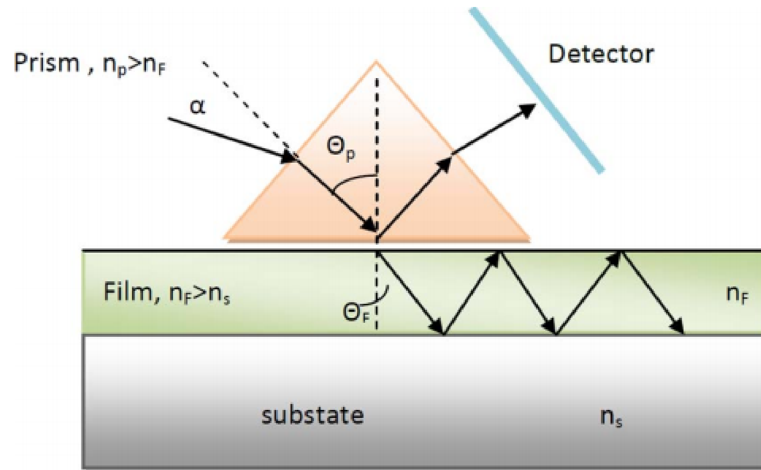

Figure 2.8: A prism coupler, where the phase matching condition is: $\beta_m \approx \beta_{prism} = n_p k_0 \sin\theta_p$, from p. 587 [3].

2.2.7 Tapered coupling

The most common used function of a taper is to change the size and shape of the optical mode and a good taper may therefore act as an efficient spot-size converter between two different sized waveguide cores, Fu et al. (2014) [25]. The single-mode fibre is coupled to a waveguide with a large enough core to ensure efficient coupling, the taper further couples between the two different sized waveguides. There are many different taper designs. A design called adiabatic will insure that the first order mode propagates through the taper without undergoing relativity little mode conversion to radiation or higher-order modes. This is ensured by making sure that the spreading of the side-walls is slower than the spreading of the lowest-order mode [25]. Taper should be relativity long so that the local half angle θ is small. A typical taper is shown in figure 2.9.

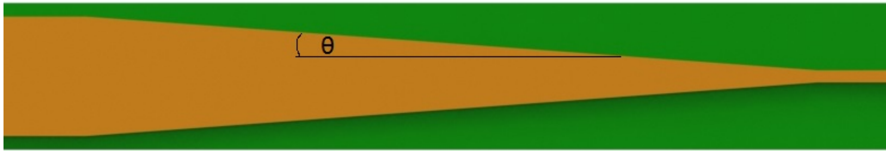

Figure 2.9: A typical taper design, where θ is the local half angle.

2.2.8 Grating coupling

A grating is a periodic structure that can be used to diffract light in and out of a waveguide. A typical setup is illustrated in figure 2.11, where a grating couples light in and out of the waveguide. A light beam travelling through air with a wavevector k_i and incident angle of θ_i interacts with the grating and the light is defused, an illustration is shown in figure 2.10. The grating modulates the incoming wave by a phase factor $\frac{2\pi m}{G}$, where $m = \pm 1$, ± 2, ... and G is the grating period [1]. This modulation makes it possible to

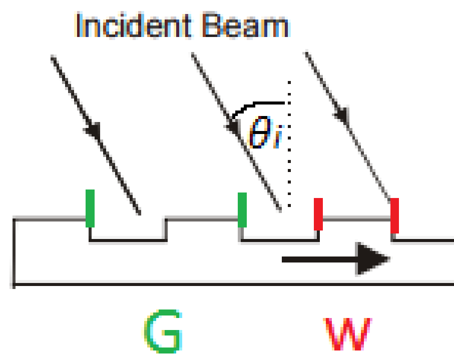

Figure 2.10: An illustration of part of a typical grating coupler where G is the grating period and w the duty cycle [4].

satisfy the phase matching condition, if $\beta_m = n_{air} k_i \sin\theta_i + \frac{2\pi m}{G}$.

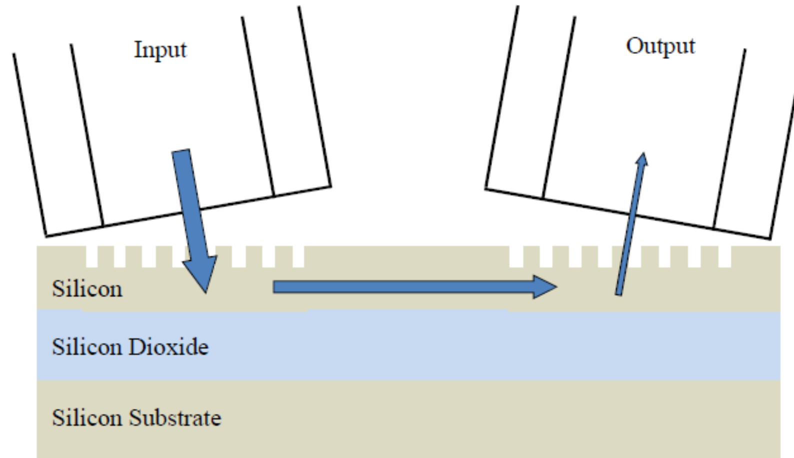

Figure 2.11: A typical experimental setup for grating coupling between a SOI waveguide and an optical fibre, from p. 5 [5].

1D gratings are the simplest grating couplers. The main characteristics of these gratings are that only one polarization is supported and the light is coupled out at an angle as shown in figure 2.11. There are many types of grating with different coupling efficiencies. Coupling efficiency is defined as the ratio between power coupled into the fibre/detector and the power from the waveguide. The different gratings are defined by these characteristics:

- w - the width of the silicon grating tooth, referred to as the duty cycle
- G - the grating period
- *ff* - the fill factor and is defined as the ratio between the duty cycle and the grating period
- *etch depth* - this is the height of the grating
- θ - the incident angle
- *uniform or non-uniform* - the symmetry of the grating
- *number of grating periods* - normally around 20, depending on type of grating

Grating couplers have the advantage that they can couple light into a waveguide from the top of the grating. This makes it preferable when integrated on a chip because it is not dependent on where it is placed. Other coupling methods couples the light at the edge and this requires polishing of the facets. Grating couplers are also fairly tolerant of alignment compared to other techniques like prism coupling.

2.2.9 Floquet theory

The behaviour of light in a grating can also be described as optical Floquet-Bloch waves or modes [26]. The advantage of Floquet theory over coupled-wave theory is that the rays play the same role in a periodic medium as plane waves does in isotropic media. Floquet-Bloch wave have their own independent solution to the wave equation which results in their own polarisation, group velocity and spatial structure. Coupled-wave theory cannot provide a very good description of what is happening inside a periodic structure as it can not exist independently. If we consider a periodic structure that is infinitely long, then we know from Bloch's theorem that the solution to the wave equation takes the form

$$E_{k_z}(z) = u_{k_z}(z)e^{-jk_z z} \tag{2.2.11}$$

where $u_{k_z}(z) = u_{k_z}(z+G)$ stating that u_{kz} is a function with the same periodicity as the grating. There is a function corresponding to each k_z. In a Floquet-Bloch mode, the propagation constant is generally complex

$$k_z = \beta + j\alpha \tag{2.2.12}$$

where α is the coupling strength of the grating and results in an exponentially decaying wave along the propagation direction.

Chapter 3

Methods and Tools

The first section, 3.1, will explain how COMSOL is used to simulate and design waveguide structures. The second section, 3.2, goes through different waveguide characterisation methods. Later, the characterisation tools, fabrication equipment and processes needed to make the structures are described. The final section is about the optical experimental setup.

3.1 Simulations in COMSOL

COMSOL Multiphysics is a suitable tool for the study of optical waveguides and grating couplers because it provides fast calculation and an automatic simulation process. COMSOLs finite element method (FEM) based calculations makes a model of electromagnetic fields based on Maxwells equations and how the fields interact with materials. FEM is a numerical method for mathematical physics that finds approximate solutions for boundary and/or initial value problems for partial differential equations. COMSOL divides the geometry into a finite number of discrete elements and utilise a mesh when simulating the structure. Each mesh element has a set of polynomial functions used to approximate the structural displacement field and the mesh can be specified manually or automatically through COMSOL. More information about COMSOL can be found in their documentation [27].

3.1.1 Simulation methods

COMSOL Multiphysics was used in this thesis to find single mode dimensions for the strip waveguide and dimensions for the minimum bend radius. The dimensions and the bend radius was optimised to get the highest possible transmitted

power. Herlitschke et al. 2011 [28] stated that for waveguides, the longitudinal grid spacings must be larger that $\frac{\lambda}{5}$, where λ is the free space wavelength. In the transversal direction, the grid spacings depend on the electromagnetic mode profile. This implies that a 3D simulation of a millimetre scale waveguide will need millions of nodes. A 3D simulation of an optical waveguide therefore requires a huge amount of computation power and time. It was therefore beneficial to use methods such as the effective index mode method to convert a 3D simulation to an analogous 2D simulation.

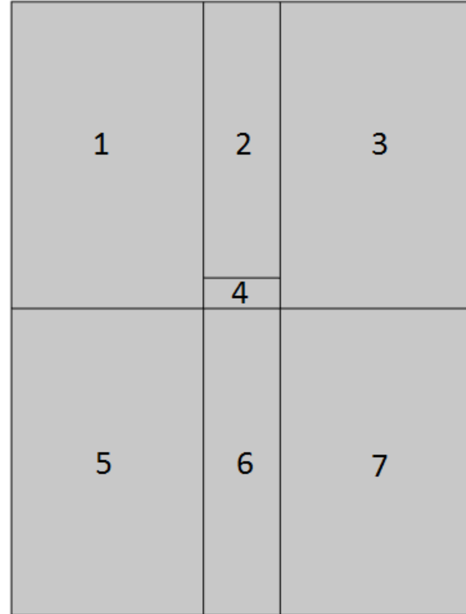

(a) Cross section of a waveguide. Section numbering representing *Surface integration* areas.

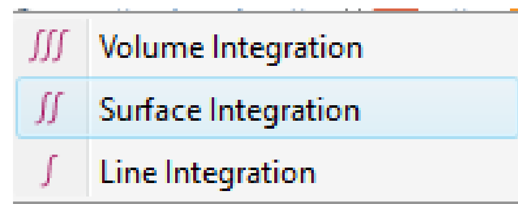

(b) The *Surface integration* function found under "Intergation" when right-clicking "Derived Values".

Figure 3.1: An illustration of how the geometry is divided into sections and the "Surface Integration" function found in COMSOL.

Effective index method

The effective index method was reviewed and applied to uniform rectangular waveguides in the article by Hocker and Burns (1997) [29]. This method looks at the cross-section of the waveguide and provides the set of rules for combining the results from the 1-D dispersion curves so that it is possible to describe dispersion in 2-D waveguides. The steps for creating and simulating the cross-section of the waveguide are explained in appendix D. These are the first steps in finding the effective index which will be used when simulating the whole waveguide structure. We want to analyse the result by using some of the different features COMSOL Multiphysics can provide.

The first step in finding the effective RI is to divide the cross-section into regions and the different refractive indices are constant in these regions. First, the weighted

RI is found in the section composed of region 2,4 and 6 in figure 3.1a. Section 5,6 and 7 is the cladding, 4 is the core and 1,2 and 3 is air. This is the area where we will have the highest effective RI since it is where the Si_3N_4 is found and therefore this is where the confined mode most likely will be. The refractive indices for each region are found in the table 3.1.

Table 3.1: The refractive indices in the different regions.

Region	1	2	3	4	5	6	7
Refractive index	1	1	1	1.98	1.438	1.438	1.438

Then we use the "Surface Integration" function found under "Integration" when right-clicking "Derived Values" in the "Model Builder". This is to find how much of the electric field is located in each area. By doing an integration of the electric field in each region and dividing it with the total surface integrated electric field in section 2,4, and 6, we get the percentage for each region. Take each RI and times it with this percentage found. If there are many modes listed, choose the mode from the list presented in COMSOL with the largest RI. The effective refractive index is then given by:

$$n_{eff(2,4,6)} = \frac{n_2 \cdot E_{integral-2} + n_4 \cdot E_{integral-4} + n_6 \cdot E_{integral-6}}{E_{integral-total}} \tag{3.1.1}$$

The "Expression" added in COMCOL is $abs(ewfd.normE)^2$. After doing the same for the two other regions, (1,5) and (3,7), we obtain three effective indices to be used in the next representation of the waveguide. This representation sees the waveguide from above. This model is build in appendix D, section D.2. To find the transmitted power in the waveguide, the "Boundary Mode Analysis" is used. This study enables ports to be added at the beginning and end of the waveguide. Port 1 can then be excited, sending an electromagnetic wave that travels through the waveguide as if a fibre has been coupled to the waveguide. It is then possible to add an expression in "Derived Values" that measure for example the transmitted power. The ports needs to be placed at the boundaries of the simulation space. The waveguides width and bend radiuses can be changed to see how it affects the transmitted power.

Mesh

The mesh is important for the simulation since the size of the mesh affects how accurate the simulation is. The mesh is made up of many small elements, so if there are minute details, the mesh needs to be small to accurately represent that

area. It is not possible however to have indefinitely small elements as this will require huge amounts of computational power. Therefore it is important to find a mesh that is fine enough for accurate simulations but does not require too much memory. An example of a predefined ”Physics-controlled mesh”, ”Extremely fine” is shown in figure 3.2. There, the mesh is not very coarse in the core area. It is however a function available, the ”User-controlled mesh”, so that one can add different sized mesh and geometries to various features of the structure. For more information on meshing, see the COMSOL documentation [27].

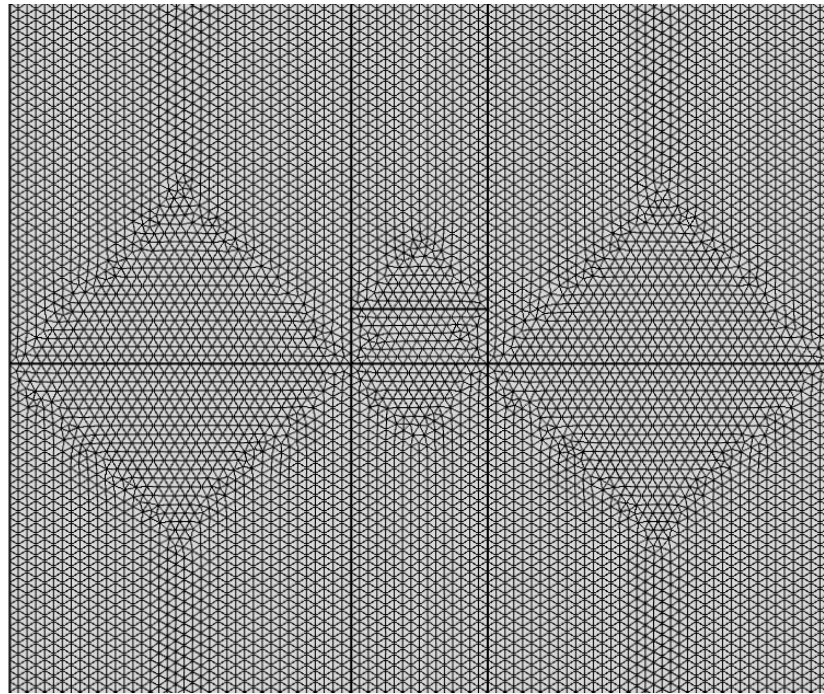

Figure 3.2: A cross-section waveguide mesh with a predefined ”Physics-controlled mesh”.

Perfectly matched layers

Perfectly matched layers (PML) are added on the outer boundary to make the structure seem infinite. The electromagnetic wave would otherwise be reflected at the outer surface back into the simulation and make the result inaccurate. Perfectly matched layers (PML) are basically an extra domain that absorb the radiative modes giving a more realistic simulation.

3.2 Waveguide characterisation methods

To have an efficient and functional optical structure, the transmission loss needs to be as low as possible. Techniques for measuring and estimating the different losses in a waveguide are presented in this section. Insertion loss is the sum of coupling loss and propagation loss.

3.2.1 The cut-back method

The cut-back method is a technique for calculating the propagation loss. By assuming the coupling loss is the same for all waveguides with the same cross-sectional dimensions, the variation in loss observed over length is mainly due to the propagation loss. By cutting a waveguide to different lengths and measuring the change in loss, one can create a model for how the loss changes with length of the waveguide. This requires cutting and polishing of the waveguide which can be difficult as it is time-consuming and impossible to polish and cut with the same quality each time. Therefore a ”virtual” cut-back method is proposed.

The paper-clip layout

To avoid having to cut and polish the waveguide, a mask layout with many different waveguide lengths is designed. This is to make sure the fabrication process is the same for all waveguides, as it would have been if one did the measurement on the same waveguide just cut to smaller lengths. The coupling loss and surface roughness loss are assumed to be the same for the different waveguides, making it possible to make a propagation loss relation. A design called paper-clip is proposed in Lim et al. (2000) [30] and Levy et al. (2011) [18]. Other work using a proposed cut-back method to measure optical loss in nanowire waveguides is Mattalib et al. (2013) [31]. A paper-clip has the shape shown in figure 3.3, which results in two bends at 180° for every waveguide making the bend loss constant for all of them. This shape is also a good way to make sure that the input and output of the waveguide are not directly opposite each other, but separated horizontally. This is to ensure that the light beam grazing across the surface of the waveguide does not hit the detector. Only the light coupled into the waveguide and transmitted through, will hit the detector.

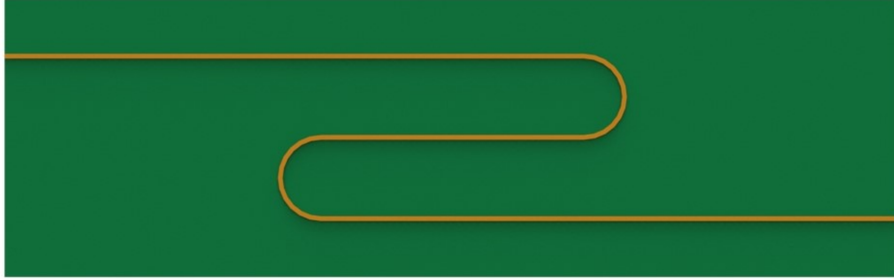

Figure 3.3: An illustration of a waveguide shaped as a paper-clip.

3.2.2 Alternative methods for measuring loss in waveguides

The Fabry-Perot resonance method is used for propagation loss measurements. This method can be more stable and accurate, but also more complicated than the cut-back method. The waveguide's two polished facets act as two mirrors and light will be reflected back and forth. R denotes the facet reflectance and the power ratio is:

$$\frac{P_{out}}{P_{in}} = \frac{(1-R)^2 e^{-\alpha L}}{(1-Re^{-\alpha L})^2 + 4Re^{-\alpha L}\sin^2(\phi/2)} \tag{3.2.1}$$

where R for TM and TE modes is given by Fresnel's equations [32]. ϕ is the phase difference, L the length of the waveguide and α is the attenuation coefficient. Using this method, the propagation loss of the TE and TM mode is found separately.

A third method used to measure propagation loss in waveguides is scattered light measurements. It is assumed that the amount of light scattered from the surface is proportional to the light propagation inside the waveguide [32].

3.2.3 Propagation loss due to waveguide dimension reduction

It is possible to determine scattering loss due to side-wall roughness by measuring the transmitted power for waveguides with different core widths, similar to the cut-back method. In the article Lee et al. (2000) [33], it is found that when the dimensions are reduced, the propagation loss becomes greater due to more scattering because of side-wall imperfections and interaction between the guided modes

in the waveguide.

3.3 Fabrication equipment and processes

As part of this master thesis, the samples have been processed in the NTNU Nanolab. Here the different equipment and methods used to fabricate the samples are presented.

3.3.1 Plasma enhanced chemical vapour deposition

Plasma enhanced chemical vapour deposition (PECVD) is a method for depositing thin films of various materials, such as silicon nitride, silicon dioxide, amorphous silicon and silicon carbide. In this master thesis, thin films of silicon nitride and silicon dioxide are deposited.

The PECVD process deposits thin films at low temperatures at a pressure of approximately 0.5-2 Torr. The equipment available at Nanolab is *PlasmaLab System 100-PECVD* provided by Oxford Instruments [34]. Gases available are: SiH4, NH3, N2O, N2, Ar, CF4, CH4, 10%PH3/Ar and 0.10%B2H6/0.23%H2/Ar. The PECVD machine is made up by a process chamber and a load-lock. The load-locks function is to make sure that when loading and unloading the sample, the process chamber remains uncontaminated. In the process-chamber in figure 3.4, there are two electrodes, a gas inlet and an exhaust/outlet. The *top electrode* has two power supplies, one radio frequency (RF) source at a high frequency (HF), 13.56 MHz, and one source between 50-460 KHz which is low frequency (LF). The bottom electrode is part of the *heated table* and is grounded. The gas

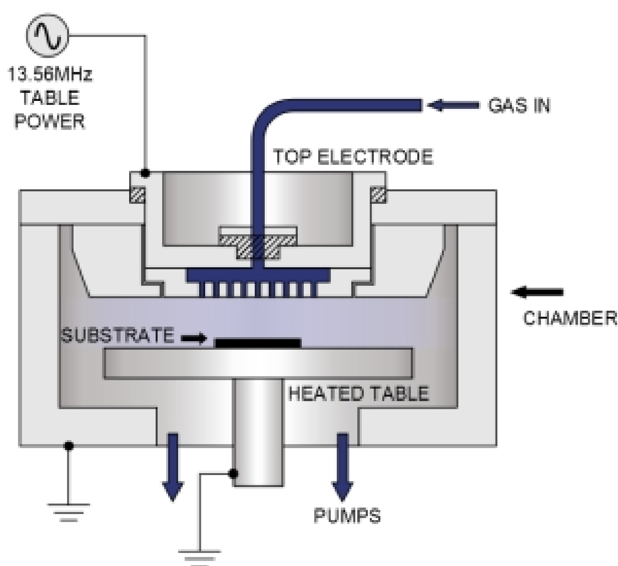

Figure 3.4: An illustration of the PECVD machine [6].

is ionized and plasma is created because of the oscillating electric field. The bottom electrode is at the sample stage and can be heated to a maximum of 700 °C. Electrons are absorbed on the bottom electrode which results in a DC voltage of 10-20V. The gas mixture interacts with the substrate and a thin film is deposited.

Various recipes will give different material characteristics, so the recipe needs to be optimised to get the intended properties. The gas ratios, flow rates and RF frequency will give varying film stress, optical and mechanical properties, stated in the recipe sheet by Oxford Instruments and shown in Gorin et al. (2008) [35]. Some common problems when depositing thin films with PECVD are surface interactions, pinholes, particles due to gas leaks or poor cleaning of chamber, and poor adhesion due to bad pre-clean and use of wrong cleaning chemicals. Poor uniformity is also a well known problem in the PECVD process.

3.3.2 Inductively coupled plasma- reactive ion etching

Dry etch is mostly an anisotropic etching process where ions are accelerated and ”shot” at the wafer surface. Gases are used to achieve a selective etching process but because of the high energy, the mask can have traces of etching on materials that were not the target of the etch.

Inductively coupled plasma (ICP) is an anisotropic dry-etching process where chemically reactive plasma under low pressure is used to remove material typically deposited on a wafer. Inductively coupled plasma-reactive ion etching (ICP-RIE) has two separate RF sources, one ICP-generator at 3000 W that strikes plasma in a gas mixture, see figure 3.5. The other RF source at 300 W creates a DC bias which results in radicals and ions being extracted and accelerated from the plasma towards the wafer surface. At NTNU Nanlolab they have Oxford Instrument’s *Plasmalab System 100 ICP-RIE 180* [36], and gases available are: H_2, O_2, N_2, Ar, CF_4, SF_6, CHF_3, He, CH_4, Cl_2 and BCl_3. Some advantages with the ICP-RIE process are high etch rates, and that low ion energy results in control over selectivity and damage to sample. The use of the instrument is similar to the PECVD with a loadlock to achieve a safe loading of the sample and a computer with an interface similar to the PECVD.

3.3.3 Electron beam lithography

To make the desired pattern, a patterning method is used. An Elionix ELS-G100 electron beam lithography (EBL) system is installed at the NTNU Nanolab [37].

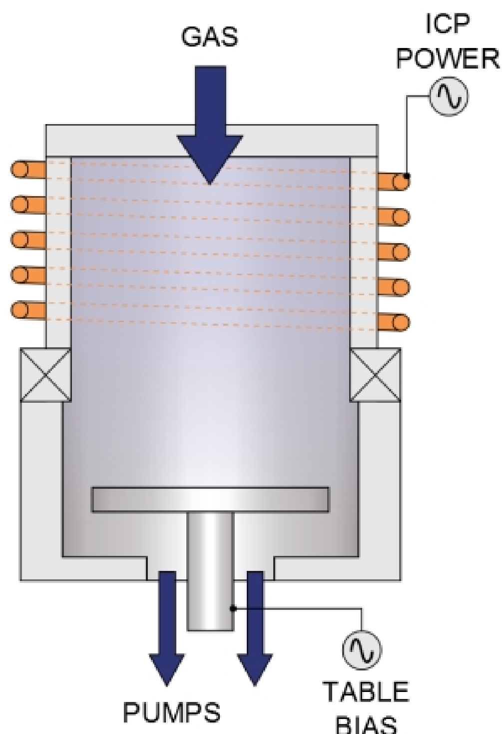

Figure 3.5: An illustration of the ICP-RIE machine [7].

A schematic diagram of the EBL is shown in figure 3.6. EBL is a patterning technique where the resist is scanned with a highly focused electron beam. The masks are made with Clewin 4, a layout editor [38].

EBL can create two-dimensional patterns down to sub-10 nm. The most important determinants are the quality of the electron optics, the chosen resist, developer, and process conditions such as electron beam energy and dose, and development time and temperature, Mohammad et al (2012) [39]. The Elionix EBL avalible at NTNU Nanolab runs at an acceleration voltage of 100 kV and has a 100 MHz pattern generator. At this acceleration voltage, the write field sizes available are 100μm, 250μm, 500μm and 1000μm. A write field is one of the areas that the software has split the mask into since the machine exposes smaller segments instead of exposing the whole sample at once. With a higher acceleration voltage it is possible to draw finer patterns uniformly. To keep the sample in focus during the exposure, the EBL has two secondary electron (SE)- and one backscattered electron (BSE) detectors and a height sensor. The minimum beam current available is 20 pA and the highest is 100 nA. At a given amount of time, the number of electrons hitting the sample is given by the beam current. Depending on the

selected beam current, the beam diameter is given. A small beam current will give finer details but will take more time. More details are given in at the Elionix Inc website [40].

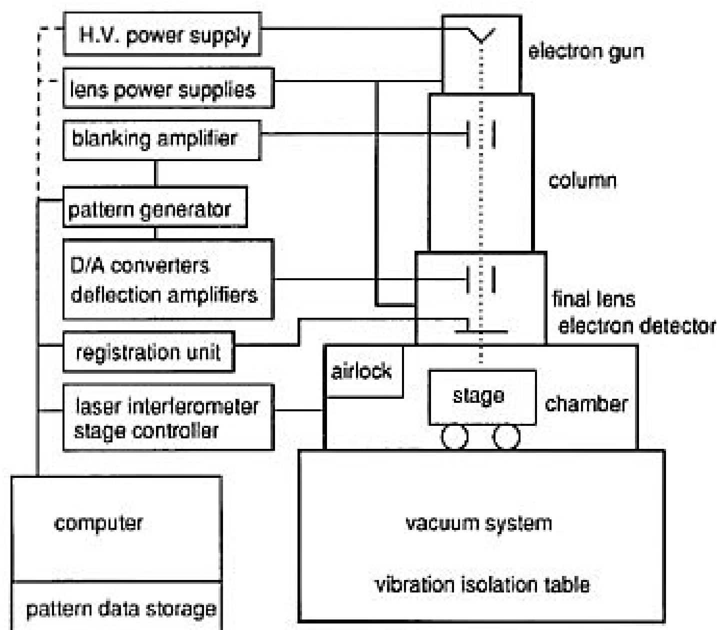

Figure 3.6: A schematic diagram of an EBL, [8].

Another mentioned determinant is the dose and this is the process of activating the resist so that the developer works on the chosen areas. The dose has the unit of $\frac{\mu As}{cm^2}$ and the ideal dose depends on factors such as the resist type and thickness, acceleration voltage, desired minimum structure size and the developer. A too high dose might make some electrons migrate into neighbouring areas leading to either an area becoming exposed which should be unexposed or over-expose another area leading to structures collapsing in the worst case.

Positive E-Beam Resist AR-P 6200 (CSAR 62), Developer AR-546 and Remover AR 600-71

The resist used for EBL patterning in this thesis is the CSAR 62, a positive e-beam resist. The one available at the NTNU Nanolab is the AR-P 6200.13, which means it has a solid content of 13 %. It has characteristics such as high resolution (≤ 10

nm), very high contrast, high sensitivity and is highly process stable. The spin curve graph for the resist is shown in figure 3.7 and more process information and characteristics are found in the product information [9].

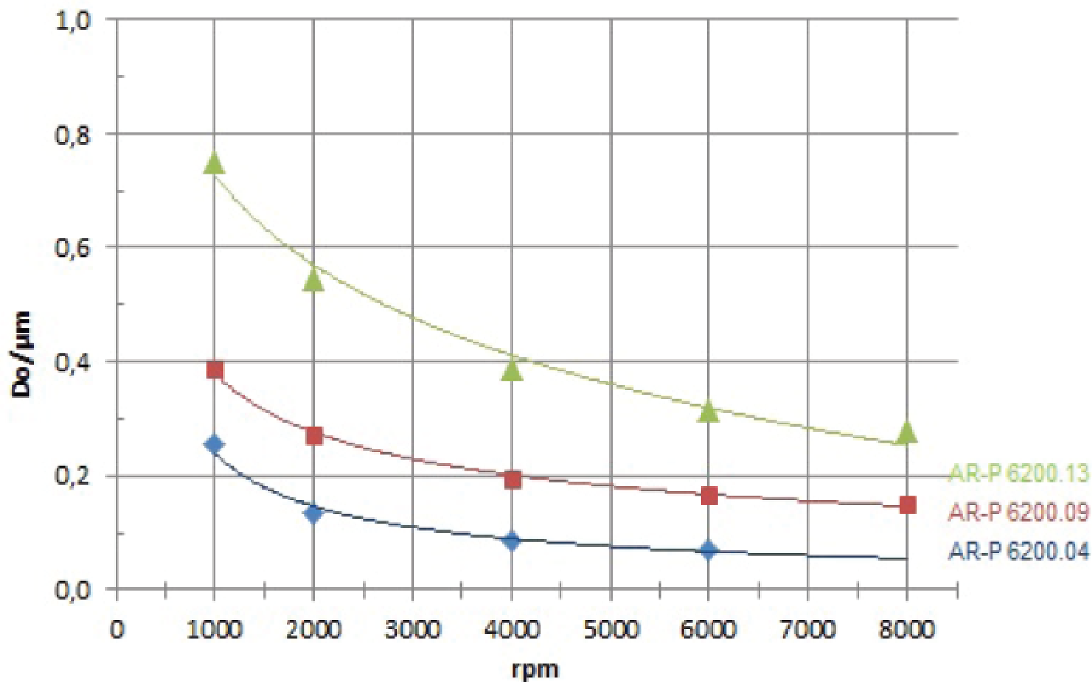

Figure 3.7: Spin curves: the resist thickness dependence on the spin speed for the CSAR 6200(.4, .9 and .13) [9].

After exposure, the resist is developed. The AR 600-546 developer, [41], is a weaker developer than the other available such as AR 600-548 and AR 600-559 so it provides a wider process window. The process should be stopped quickly, so a rinsing step of first 1 minute in isopropanol (IPA) then 30 seconds rinse in distilled (DI) water is necessary. A post-bake at 130° C can be useful for improving etch stability during plasma-chemical and wet-chemical processes.

When the etching process is over, the rest of the resist is removed with the AR 600-71 remover, [42]. This remover is described as an efficient all-rounder. The sample is immersed (puddle or dip) into the remover and the time is dependent on the type of resist, resist thickness and the temperature of the soft bake. The remover is rinsed off by either DI water or clean remover.

3.3.4 Scriber

A scriber machine is used to divide a 4″ wafer into many small pieces of a chosen size, which for example are to be used as samples. The machine used in this work is the Dynatex DX-III [43]. First, the wafer is scribed with a diamond tip scriber and then broken with an impulse bar. The impulse bar will hit the scriber line with a force that cleanly separates the pieces. An administrator defined file is loaded before starting the process and the user can further change parameters such as scribing speed, scribe and break force, and what angle it will hit the sample with.

3.4 Characterisation equipment

The various characterisation equipment used to verify and investigate the fabrication methods used in the thesis are presented here.

3.4.1 Scanning (transmission) electron microscope

A scanning (transmission) electron microscope (S(T)EM) scans a sample with a focused electron beam which results in an image of the sample. The S(T)EM available at NTNU Nanolab is a Hitachi model S-5500, [11]. The S-5500 S(T)EM is an in lens cold field emission electron microscope and the maximum resolution of 0.4 nm is achieved at an acceleration voltage of 30 kV. The electron gun shoots electrons at the sample and as they hit the sample surface, some of them are backscattered and others are absorbed and re-emitted as secondary emitted electrons. The backscattered electron (BSE) provide information about the materials at the surface since it gives an ”elemental” contrast, heavier materials reflect electrons better. The secondary electron (SE) will give information about the geometry and shape of the material.

The acceleration voltage of the electrons can be changed and depends on the desired information needed. A higher acceleration voltage, highest possible with the S-5500 is 30 kV, will give a larger specimen interaction and the electrons will penetrate deeper into the material. See an illustration of the physical S(T)EM process in figure 3.8. The SE will then originate from a location deeper in the specimen and give a smoother appearance. When having a lower acceleration voltage, here the smallest is 0.5 kV, the SE will be scattered and interact only with the surface. This means that when looking at features at the surface, a lower acceleration voltage is desirable.

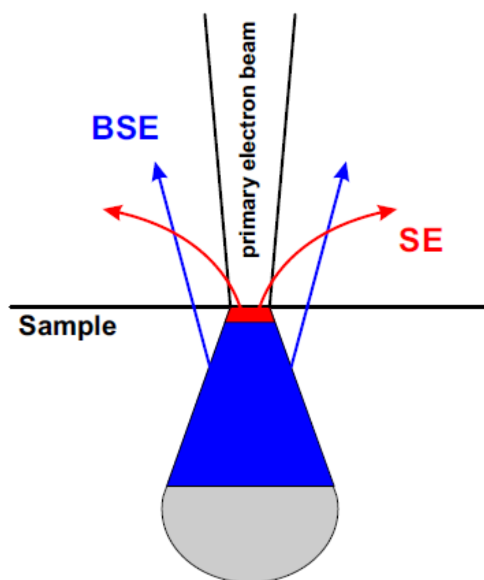

Figure 3.8: An illustration of the physical process in the S(T)EM, [10].

The S(T)EM is also equipped with a transmission setup. It is positioned below the sample stage, seen at the bottom of figure 3.9. Here, a dark field (DF) detector detects electrons scattered under a certain angle when passing through a thin sample, and the electrons that passed through without being scattered is collected by the bright field (BF) detector. In this thesis, the SEM function is used to check the deposition rate, waveguide profile and etch quality. The cross-section holder available is useful as it gives the opportunity to inspect the samples cross-section and layers. The thickness of the deposited layers are investigated using this holder.

3.4.2 Reflectometer

The film thickness of SiO_2, the resist and Si_3N_4 can be measured using a reflectometer. At the NTNU Nanolab, the F20 Filmetrics [44] is available for quick thin film measurements. This instrument uses the spectral reflectance technique, where light is reflected from a surface and analysed giving the film thickness, as well as information about the optical constants (RI and the wave vector). It can be used for many different applications, such as investigating semiconductor fabrication like photoresist, oxides and nitrides, investigating cell gaps and polyimide in liquid crystal displays, measuring optical coatings and in biomedical application it can investigate parylene, membrane thickness and nitrocellulose.

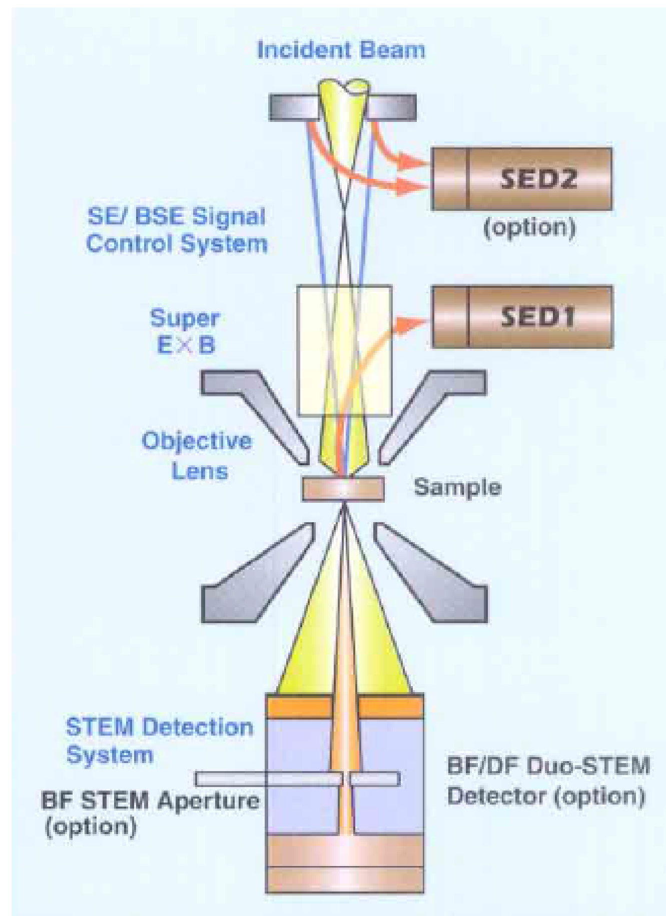

Figure 3.9: An illustration of the mechanism and parts in the S(T)EM, [11].

Since the technology used depends on the reflections at the interface between different materials, the technique is sensitive to roughness and defects in the material. It is also more difficult to measure thin films if the materials used have a RI very close to one another and if there are multiple layers of different thin films. The instrument make many assumptions about the material, so if the users material does not have exactly the same properties, the result can be wrong. It is also necessary for the user to provide the approximate thickness of the material. If the software does not know this, it is impossible to find the thickness.

3.5 Experimental setup

The structures need to be tested and characterised experimentally. An optical characterisation setup was built to test the structures and is illustrated in figure 3.10. A list of all equipment used is provided in table 3.2. We configured the setup with three different lasers to allow characterisation at different wavelengths, as shown in figure 3.10. One laser at 1550 nm, a tunable laser with central wavelength at 1550 nm and a HeNe-laser at 632.8 nm. In this work, since we are working with a biological application and Si_3N_4, the 632.8 nm laser is the laser of choice.

The laser is coupled to a fibre and the light is transmitted through a single-mode fibre and a polarisation controller before being coupled to the sample through a taper. This is to achieve a smaller and more focused spot to easier couple to the sample. Then the light on the back-side of the sample is butt-coupled to a tapered fibre. The light then is transmitted through an in-fibre polariser and into a photodetector. The light is amplified and the signal is displayed on the oscilloscope.

The separate mount stages make it possible to move the fibres in all directions to easier line up the fibres and the sample. The sample can be moved horizontally and vertically with high precision, it can also be tilted with a screw. It is very important that the fibres are moved carefully to not break them, as they are very fragile. When removing or placing the sample-holder on to the stage, the fibres should be move to the sides so they are out of the way. It is difficult to see the tips of the fibres when moving them very close to the sample. There is therefore an IR camera mounted on a movable stage to help monitor the coupling. For the 632.8 nm laser, it is easier to see the light as it is in the visible range.

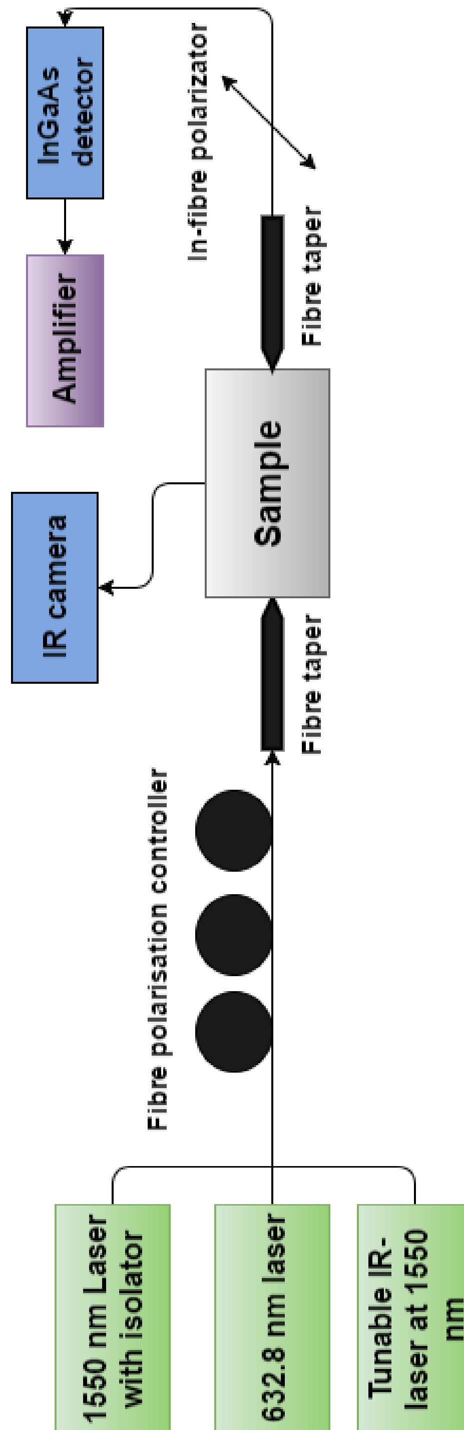

Figure 3.10: An illustration of the experimental optical setup.

Table 3.2: List of equipment comprising the optical characterisation setup

- HeNe - Laser at 632.8 nm
- Tunable Laser Kit - *Thorlabs TLK-L1550R, Central Wavelength 1550 nm, Typical Power 35 mW and Typical 10 dB Tunin 120 nm*
- Distributed feedback laser (DFB) m/APC - *Anritsu GB5A016 S/N D07731*
- Laser Driver - *Newport Model 505*
- Laser mounting *Thorlabs LM14S2*
- Laser Temperature controller - *Newport Model 325*
- Polarization controller - *Thorlabs 973/579-7227*
- Non-PM Coupler - *CWDALSOM221035 NC/NC*
- PM Coupler with FC/APC - *AC Photonics 2x2 50/50 PM coupler S/N 400d4*
- Tapered Fibre - *Nononics with PM fibre and APC 6μm wd, 2μm spot*
- Fibre FC/PC - FC/APCR - *Foss 8-1A5D-1015*
- Fibre FC/PC - FC/APCR - *Foss 8-1A55-1015*
- In-Fibre Polarizer - *Chiral Photonics IFP-155D-SM/SM, IFP-10072*
- Flexure stages XYZ Coordinate System - *Elliot Scientific Ltd. MDE122*
- IR camera - *Hamamatsu C2400 Control system and camera head*
- TV - *Hitachi*
- Microscope
- Fine thread focus tube (C-mount) - *Edmund optics F03-625*
- Double thread rings (male-male) - *Edmund optics F03-629*
- Digital oscilloscope - *Tektronix TDS2004B*
- DC-voltage supply - *FE FC3048*
- Function generator - *InSTEK GFG-8215A*
- InGaAs photo-detector

Chapter 4

Design and simulation

In this chapter, the results from various simulations are used to design the optimal waveguide. Simulations together with a literature study give a good foundation for designing a single-mode waveguide with low loss. Later, the various mask designs are presented.

4.1 Waveguide design

Silicon dioxide was used as the cladding and will act as an optical isolator so that there will be little or no leakage into the substrate. The substrate was a 500 μm thick silicon wafer. It was shown in Subramanian et al. (2013) [45] and [30], that to avoid substrate leakage, the cladding needs to be thicker then 1.5 μm. The SiO_2 layer was therefore chosen to be 2 μm thick.

In section 3.1.1, the effective index method is described. An effective index of 1.8503 was found and applied to the 500 nm wide waveguide core when the laser source had a wavelength of 632.8 nm. The two areas on the sides were found to have an effective index of 1.078. The refractive index found with a 400 nm wide core was 1.84. It was therefore possible to use the same RI for all the widths as the effective refractive indices were very close and for these simulations accurate enough to get a reasonable result.

It was found in this thesis, that the largest width that gave single-mode was 550 nm. In figure 4.1, the first 6 modes for a waveguide 200 nm x 500 nm are shown. Here, one can see that no multi-mode is supported in the core. This way we can conclude that with a width of 500 nm, the waveguide will guide only a single-mode. This was checked for many widths, resulting in 550 nm as the largest single-mode waveguide. The height of 200 nm was taken from literature, Subramanian et al. (2013) [45].

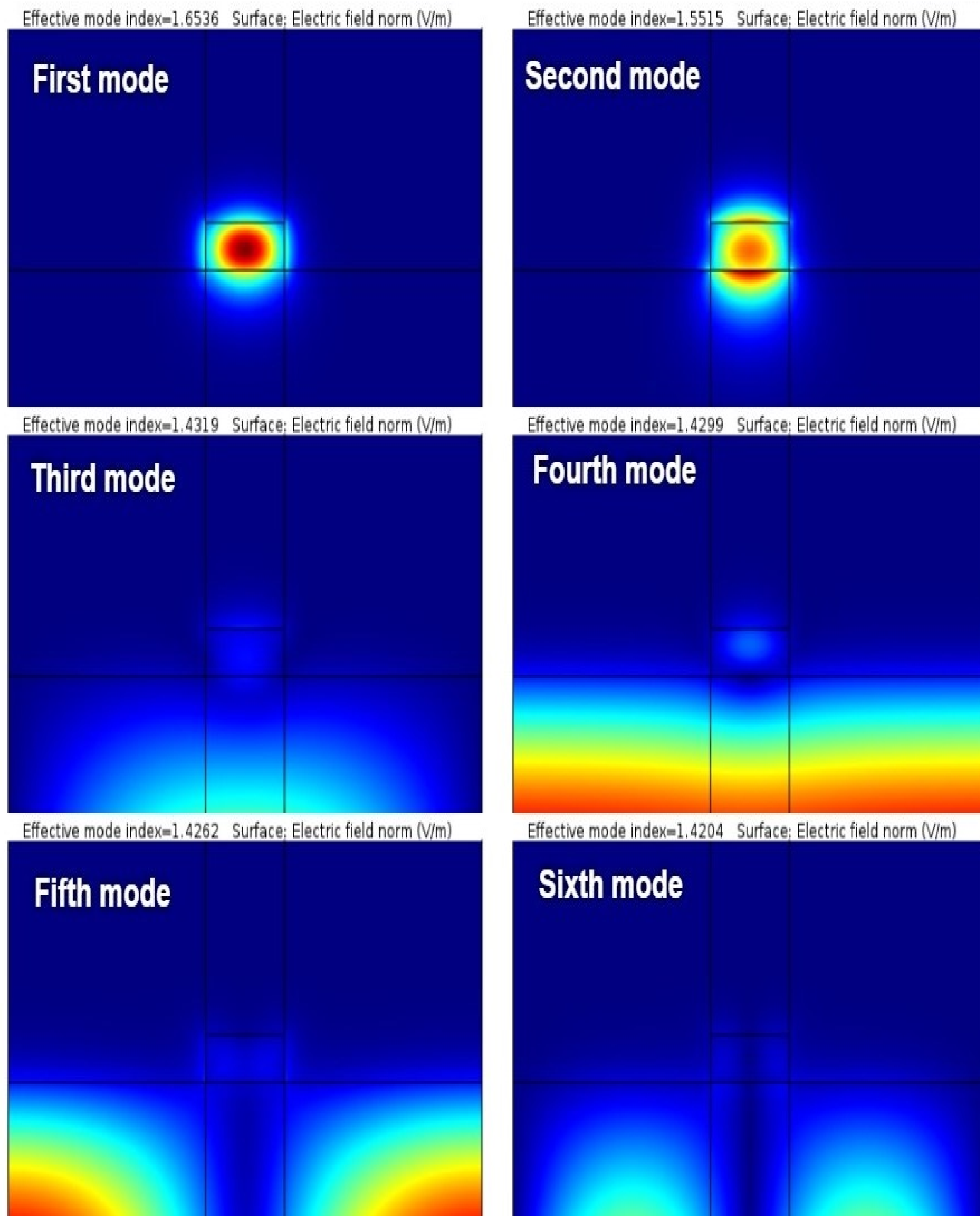

Figure 4.1: Mode plot of the first 6 modes with a Si_3N_4 core of 200 nm x 500 nm.

4.2 Test structure design

A test plan with six different paper-clip sizes was proposed. The straight waveguide will be cm long. The five others will stretch out for 1 cm as well but have variable physical length. As seen in figure 4.2, the two waveguides will have the same distance between input and output but have different physical lengths. This makes it easier to carry out the experimental test as one can have many waveguides in parallel on the same sample. This will also make the coupling loss as stable as possible across the waveguides since the waveguides are scribed and broken in to pieces at the same time. In table 4.1, the six lengths that will be used in the mask design are presented.

Table 4.1: The actual waveguide length with bends. The length from input to output is kept at 1 cm for all waveguides. The various widths investigated to find the loss due to side-wall roughness are also presented.

Physical length [cm]	1	1.15	1.3	1.45	1.6	1.75
Waveguide widths [nm]	400	450	500	550	600	700

The relationship between the dimensions of the paper-clip is illustrated in figure 4.3. x is the length of half of the short waveguide in between the longer waveguides. x is then varied to obtain the physical length desired. y is the bend radius. These lengths are added up to give the total length expressed as:

$$L_{tot} = 2 \cdot 0.5cm + 2 \cdot \pi \cdot y + 4 \cdot x \tag{4.2.1}$$

By adding bends to the simulation of a straight waveguide, it was possible to simulate the propagation loss caused by bends. The bend simulation model is shown in figure 4.4. The loss in a 180° bend was found for different bend radiuses. This method was also used in article Neutens et al. (2014) [46].

The results from a parametric sweep are presented in table 4.2. From the bend radius loss simulation, a 35 μm bend radius was shown to have very little loss and was therefore chosen as the bend radius in the paper-clip waveguides. It was also important to look at a minimum distance between waveguides so that they will not couple power to each other. After the bend radius and the lengths were chosen, the x could be solved for each length required.

The minimum distance was found by having two waveguides parallel to each other and varying the distance between them. A port was excited in one of the waveguides. Then the power difference between this port at the input of waveguide

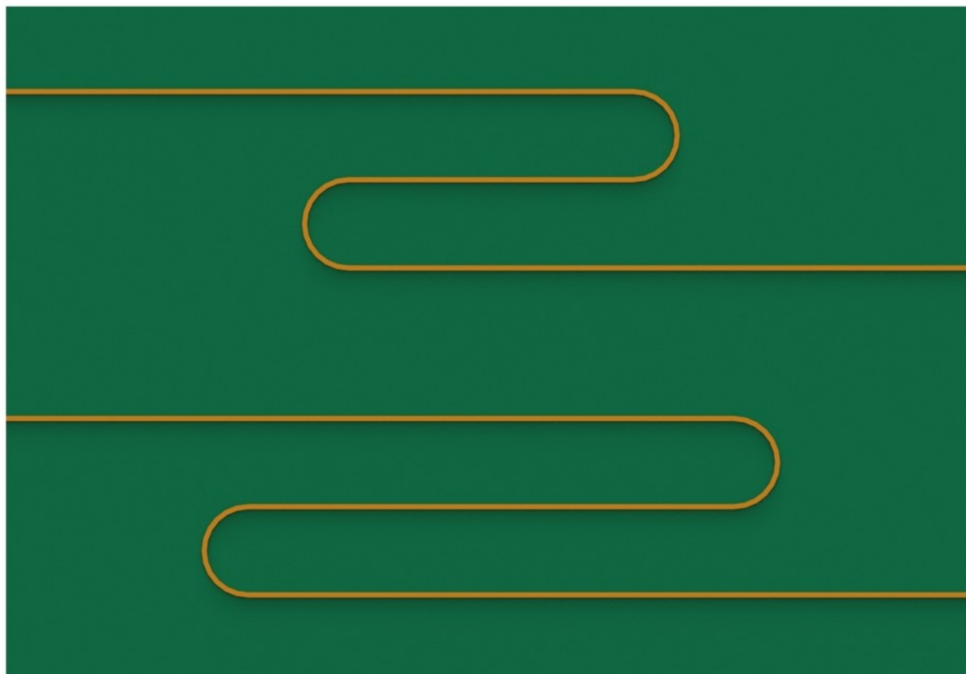

Figure 4.2: An illustration of two waveguides with different physical lengths but the same distance between input and output.

Table 4.2: The power ratio between the input and the output port is presented. 1 = 100 % transmission. The results are from COMSOL "Derived values" when performing a parametric sweep over the bend-radius's listed.

Bend radius [m]	freq [Hz]	abs(ewfd.S21)^2\Transmitted power
2.0000E-5	4.7376E14	0.99998
2.5000E-5	4.7376E14	0.99997
3.0000E-5	4.7376E14	1.00000
3.5000E-5	4.7376E14	0.99996
4.0000E-5	4.7376E14	0.99972
4.5000E-5	4.7376E14	1.00000
5.0000E-5	4.7376E14	1.00000

1 and the port at the output of waveguide 2 were measured. The goal was to have no power in the output port. Before the simulation, we could say that the minimum distance had to be at least 10 μm since that is approximately the spot size of the single-mode fibre. It was therefore necessary to take the coupling into

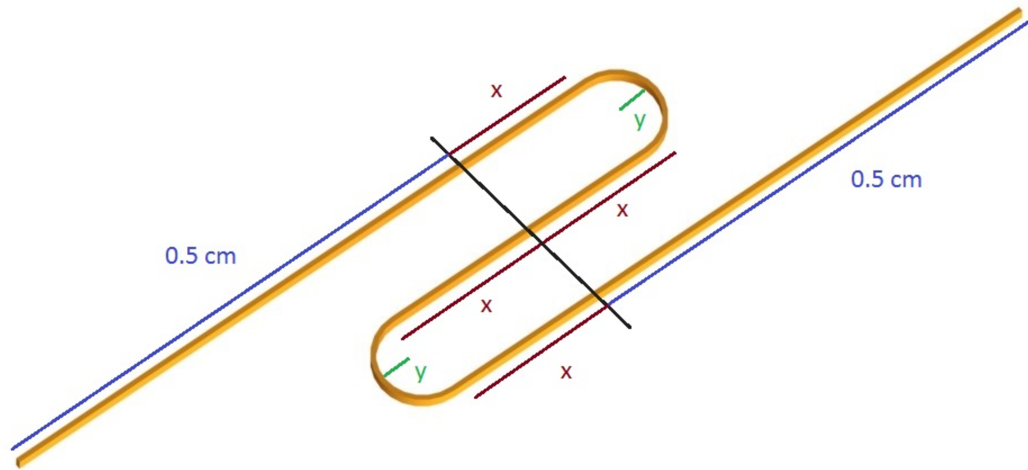

Figure 4.3: The paper-clips dimensions. x is half of the length of the short straight waveguide and y is the bend-radius.

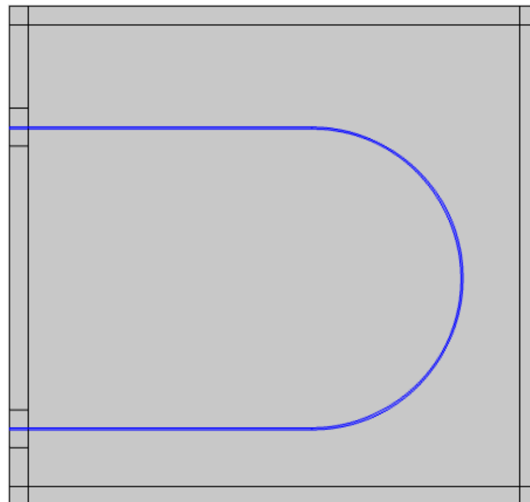

Figure 4.4: A waveguide with a bend with 35 μm bend radius. The bend is 180° and the waveguide dimensions are 200 nm x 500 nm.

account as well to not couple light into both waveguides with the fibre. The results from a parametric sweep with distances between the two waveguides of 10 μm to 100 μm are shown in table 4.3. For 70 μm, which is the distance between two waveguide with the chosen bend radius of 35 μm, the coupling was 5.1×10^{-69}%. This meant that extremely little to no power was coupled between the waveguides.

Table 4.3: The percentage of power coupled out at the output of the second waveguide when light is coupled into waveguide number one. 1 = 100%

Distance between waveguides [m]	Frequency [Hz]	abs(ewfd.S41)^2\Transmitted power
1.0000E-5	4.7376E14	1.9177E-35
2.0000E-5	4.7376E14	2.8879E-47
3.0000E-5	4.7376E14	5.7577E-50
4.0000E-5	4.7376E14	5.1859E-61
5.0000E-5	4.7376E14	8.0320E-65
6.0000E-5	4.7376E14	1.0110E-64
7.0000E-5	4.7376E14	5.0970E-69
8.0000E-5	4.7376E14	7.7149E-74
9.0000E-5	4.7376E14	2.2652E-72
1.0000E-4	4.7376E14	8.1394E-77

To measure the propagation loss due to side-wall roughness, the width of the waveguide will be varied. Instead of making the waveguide shorter or longer to find propagation loss per length, we will find a relation between width and propagation loss. A design with six different widths was therefore proposed. The widths are listed in table 4.1. For the widths smaller than 550 nm, we will have one guided single-mode. The 600 nm and the 700 nm were included to see how multi-modes will affect the light transmission.

4.2.1 Taper design

To help couple the light from the larger spot-size of a fibre via butt-coupling, a taper will convert the mode so it has a smoother transition to the guided mode in the waveguide. The design was taken from an article by Muttalib et al. (2013) [31]. They used a 5 μm wide taper which is hundreds of μm long. The length is dependent on the width of the waveguide core since the local half angle of the taper should be constant when varying the width [31]. To keep the whole length across the sample equal to 1 cm, there will be an input-waveguide on the outside

of the taper with a core-width of 5 μm, see figure 4.5. This is because the length of the actual wavelength needs to be constant. Article [31] gives the relation:

$$T_{length} = (In - W_{Width} - W_{Width}) \times 500 \tag{4.2.2}$$

where T is the taper, *In-W* the input-waveguide and W the waveguide core. The number 500 can be changed as long as it stays constant, it will ensure a constant adiabatic taper angle (θ). In this work, the constant 500 was considered too large as the tapers would then take up a large part of the sample length. The material used in Muttalib et al. (2013) [31] had a very large refractive index compared to Si_3N_4, so the design was therefore used just as a guidance. Many millimetres of taper will shorten the length of the waveguide to be characterised and a long taper will give rise to a larger propagation loss coming from areas not part of the intended investigation. Therefore, a *factor* of 200 was chosen instead and this led to the various lengths presented in table 4.4.

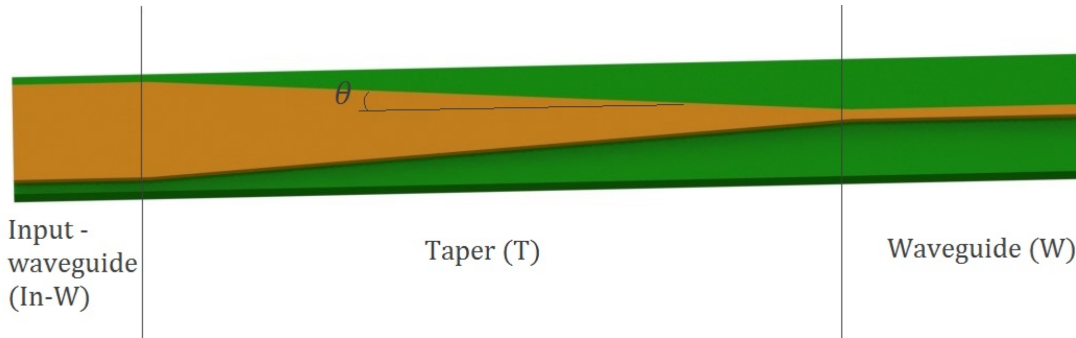

Figure 4.5: An illustration of a tapered waveguide. First, there is an input-waveguide before it narrows slowly down at an angle θ to the height of the main waveguide core.

Table 4.4: The various lengths of the taper (T) and the input-waveguide (In-W) ensure that the angles and the waveguide (W) and sample lengths are constant. The lengths are found using equation 4.2.2 with factor 200 instead of 500.

Sample width	$\mathbf{W}_{length}$	$\mathbf{W}_{width}$	$\mathbf{T}_{length}$	$\mathbf{In\text{-}W}_{length}$
10 mm	7.5 mm	700 nm	860 μm	390 μm
		600 nm	880 μm	370 μm
		550 nm	890 μm	360 μm
		500 nm	900 μm	350 μm
		450 nm	910 μm	340 μm
		400 nm	920 μm	330 μm

Tapers contribute to the transmission loss as it behaves as a mode converter where modes are lost due to effects such as destructive interference and leakage to the cladding, resulting in power losses. Therefore a test with different taper lengths was proposed to experimentally find the ideal *factor*. It is also important to see if 200 gives a sufficient taper length. The main waveguide for the taper-test mask will have a core width of 450 nm and a length of 4 mm. The different taper and input-waveguide lengths were found using equation 4.2.2 with various *factors* instead of 500, and are presented in table 4.5. The *factor* changed the length of the taper and therefore also the local half angle as the waveguide widths were kept constant. By doing a paper-clip cut-back on a 5 μm wide waveguide, the propagation loss in the input-waveguide can be estimated and subtracted from the result. The coupling loss and propagation loss in the main waveguide will be the same for all the waveguide structures, and they will be treated as an off-set.

Table 4.5: The taper-test lengths and the input-waveguide lengths when the main waveguide is 4 mm long and 450 nm wide. The lengths are found using equation 4.2.2 with *factor* instead of 500.

Factor	$\mathbf{W}_{length}$	$\mathbf{W}_{width}$	$\mathbf{T}_{length}$	**In-W**$_{length}$
100			455 μm	2545 μm
200			910 μm	2090 μm
300	4 mm	450 nm	1365 μm	1635 μm
400			1820 μm	1180 μm
500			2275 μm	752 μm
600			2730 μm	270 μm

4.2.2 Propagation loss measurements in bends

Since there are two 180° bends in the waveguide structure to be characterised, the loss in the bends need to be measured as well. This was done by measuring the transmitted power through various sized bends, these are listed in table 4.6.

Table 4.6: The various bend radiuses which will be used in a bend-loss measurement.

Bend-radius [μm]	65	55	45	35	25	15	10	5

4.3 Mask design

With the different lengths, bend-radius's and taper sizes in the previous section, masks were made. In Clewin 4, the masks were drawn with the tools and features available. Four different masks were made to achieve the desired loss measurements; propagation, bend, side-wall roughness and taper loss.

Mask 1: The first mask is the paper-clip design shown in figure 4.7. The green coloured areas are exposed by the EBL. These areas are 8 μm wide on all the sides of the waveguide, the waveguide is in between as shown in figure 4.6. The designed mask has six sets of six waveguide lengths. For each width, there will be six waveguides with the lengths proposed in table 4.1. In the paper-clip method, only the waveguides with the same widths can produce a propagation loss estimate, so tapers are added to these waveguides and treated as part of the constant coupling loss. The structures are spaced 200 μm apart to easier couple light into each individual waveguide. The taper dimensions for each width is found in table 4.4. Numbers are added next to each waveguide to help navigating when trying to couple light into the waveguides.

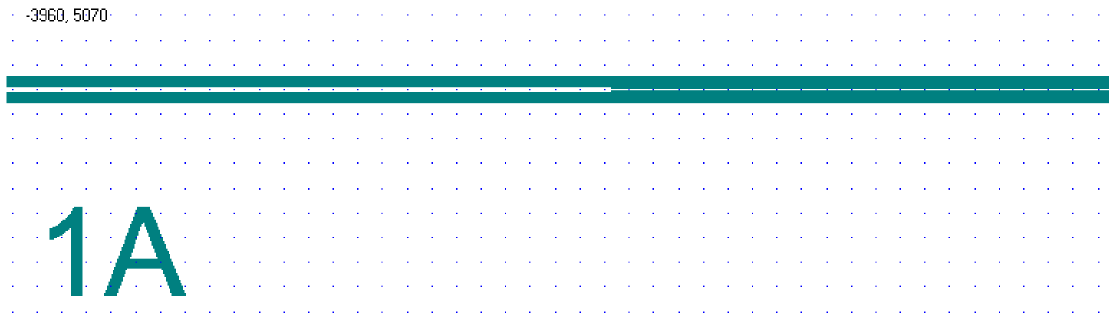

Figure 4.6: A clipping of a taper at the beginning of a waveguide. The white part is the waveguide and the green part on the sides are the 8 μm wide exposed area.

Mask 2: This mask measures the side-wall roughness loss and is exactly like the paper-clip mask but without tapers. Instead of tapers, there are straight waveguides. This is because the tapers will have different sizes for each width, meaning the coupling loss will not stay constant, making the result inaccurate.

Mask 3: The third mask tests the loss due to tapers and this information is also used to find the ideal *factor* value. The main waveguide in the middle is kept at a width of 450 nm, so only the parameter *factor* is changed. The various lengths are found in table 4.5. All together, there are six different taper lengths and the

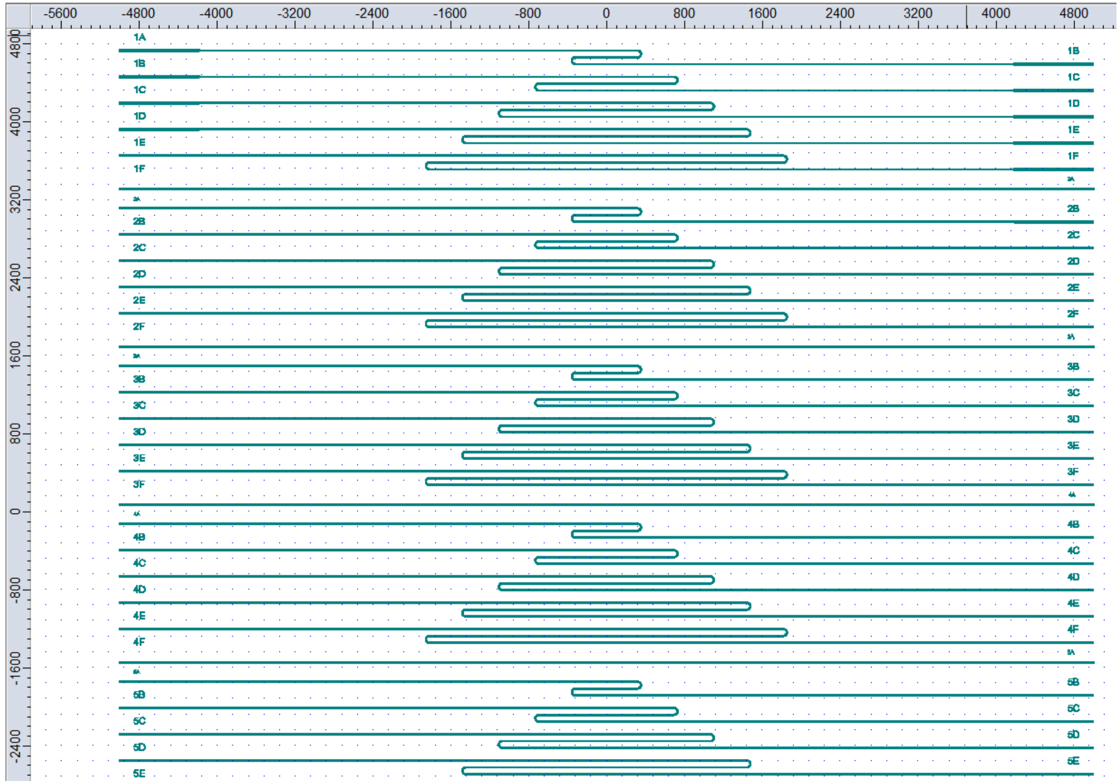

Figure 4.7: The paper-clip tapered mask created in Clewin 4.

sequence is repeated twice to have a back-up waveguide in case a waveguides get destroyed during fabrication. A paper-clip layout with a waveguide of width 5 μm can also be added to this mask, but it is not added for the mask shown in figure 4.8.

Mask 4: The last mask design is the bend-radius test. Eight radiuses are shown in table 4.6. Three widths are chosen since the bends will result in different loss depending on width. Tapers are added as before, depending on width with a *factor* of 300. The taper, input-waveguide and waveguide lengths for each width is given in table 4.7. The mask is shown in figure 4.9.

Table 4.7: The taper, input-waveguide and waveguide length for each width with a *factor* of 300.

Factor	$\mathbf{W}_{length}$	$\mathbf{W}_{width}$	$\mathbf{T}_{length}$	$\mathbf{In\text{-}W}_{length}$
300	7 mm	400 nm	1380 μm	120 μm
		450 nm	1365 μm	135 μm
		500 nm	1350 μm	150 μm

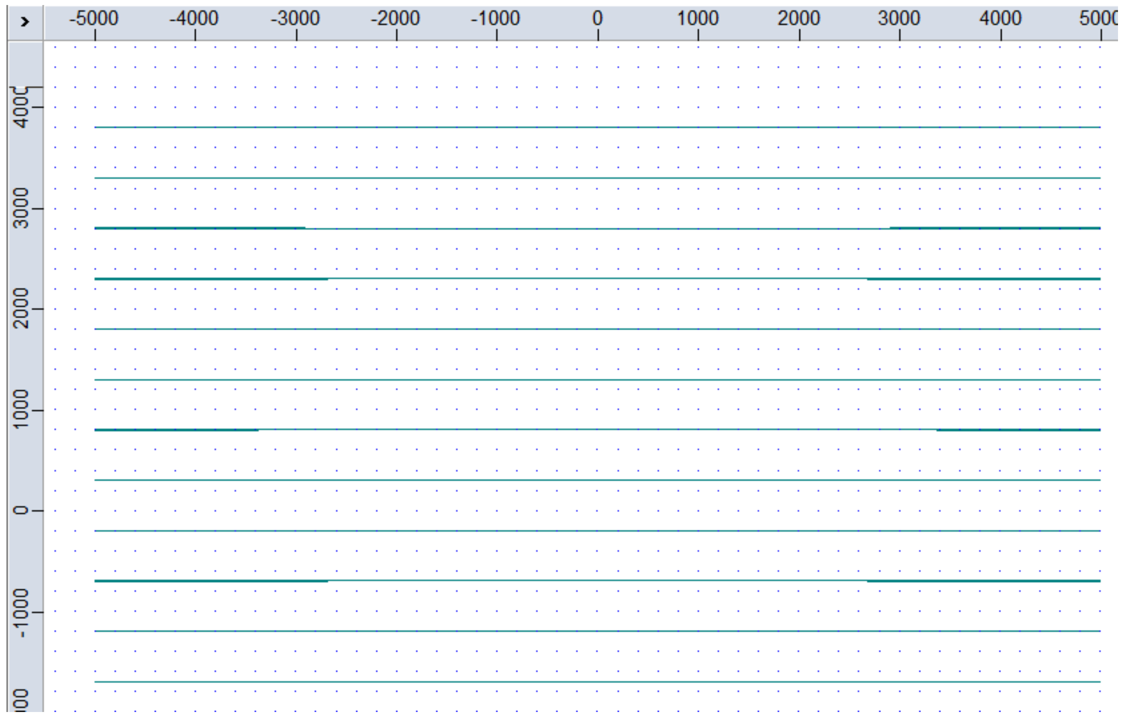

Figure 4.8: The taper test-mask created in Clewin 4.

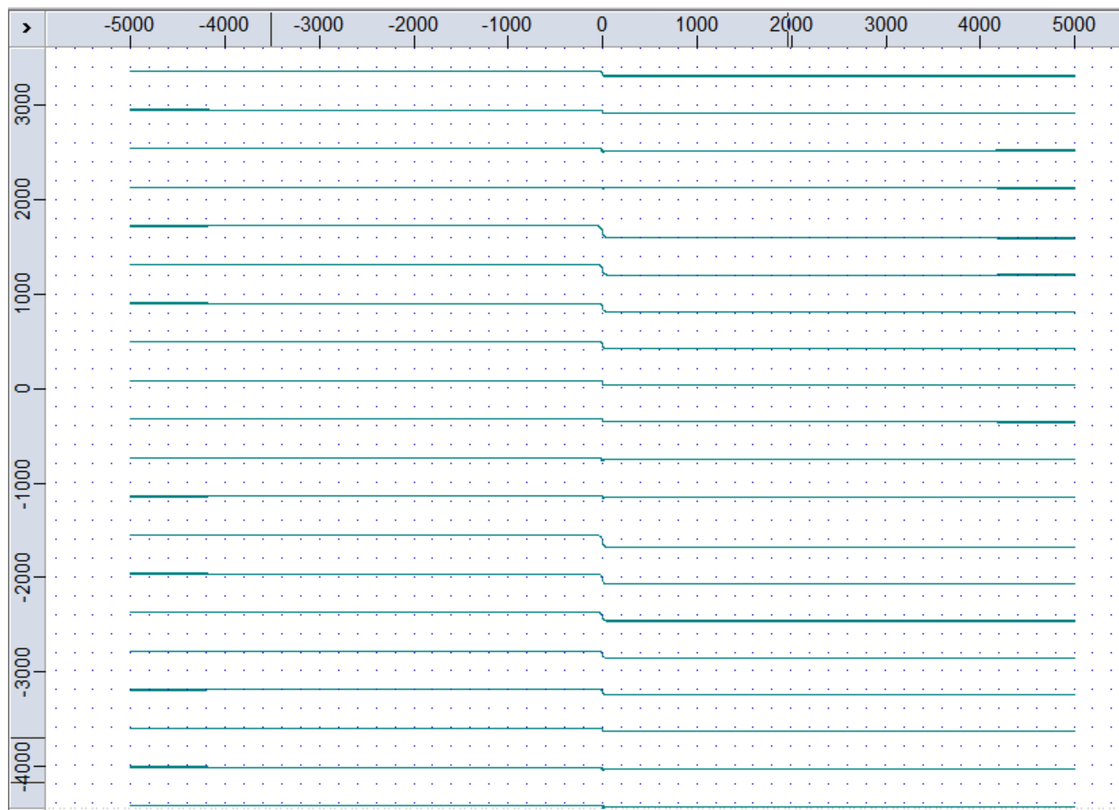

Figure 4.9: The bends loss test-mask created in Clewin 4.

4.4 Grating coupler

As part of the project thesis [16], a grating coupler was designed and simulated in COMSOL Multiphysics. Further simulations were done in this thesis. The grating coupler was not fabricated in this thesis due to time constrains, but was included as it has potential as a coupling technique and can be interesting for future work. A summary of what was done in the project thesis is presented here. The complete design and simulation method is found in the project thesis [16].

4.4.1 Grating coupler simulations

Floquet theory was used to find the correct grating period and duty cycle which satisfy the mode matching condition. A fill factor of 80% was found to ensure a forward propagation TE-polarised wave. An angle of 10° was set as the incident angle, and the wavelength was 1550 nm. To find the ideal grating period and duty cycle, only one period of the grating was simulated. Boundary condition defined by floquet theory on each side of the grating period is periodic and makes the grating appear infinite, see figure 4.10. In COMSOL, an eigenfrequency simulation was run and the grating period and duty cycle were changed to get an eigenfrequency as close to the free space wavelength (1550 nm) as possible.

After having optimised the grating parameters, the full grating coupler was simulated. It is easier to simulate coupling from the grating to the fibre as the wave is excited inside the waveguide and coupled through the grating and detected in a port acting as a fibre. The power transmitted from the port in the waveguide to the fibre was measured and the coupling efficiency was found. A third port was added to determine how much power was transmitted through the grating either to a waveguide or air. In this case it was a waveguide. See figure 4.11 for an illustration of the grating structure simulated.

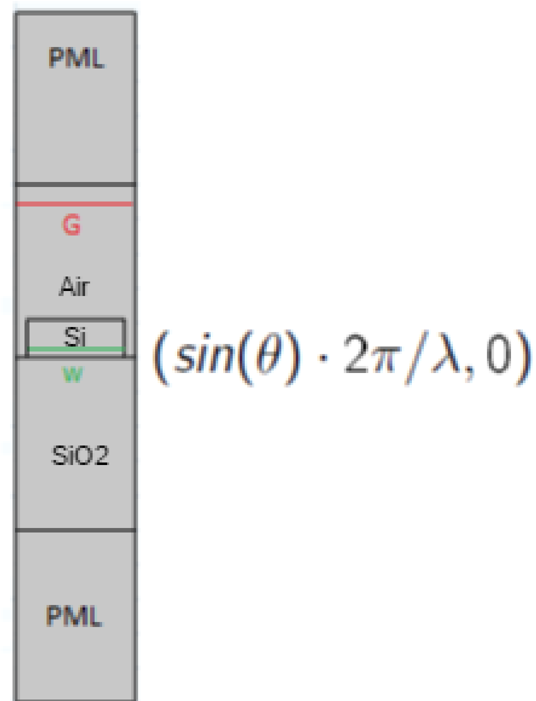

Figure 4.10: One grating period of the proposed grating. Perfectly matched layers are defined at the outer layers at the top and bottom and on the left and right side, a Floquet boundary condition of $\vec{k_f}(x, y) = (\sin\theta \cdot 2\pi/\lambda, 0)$ is added. G is the grating period and w is the duty cycle.

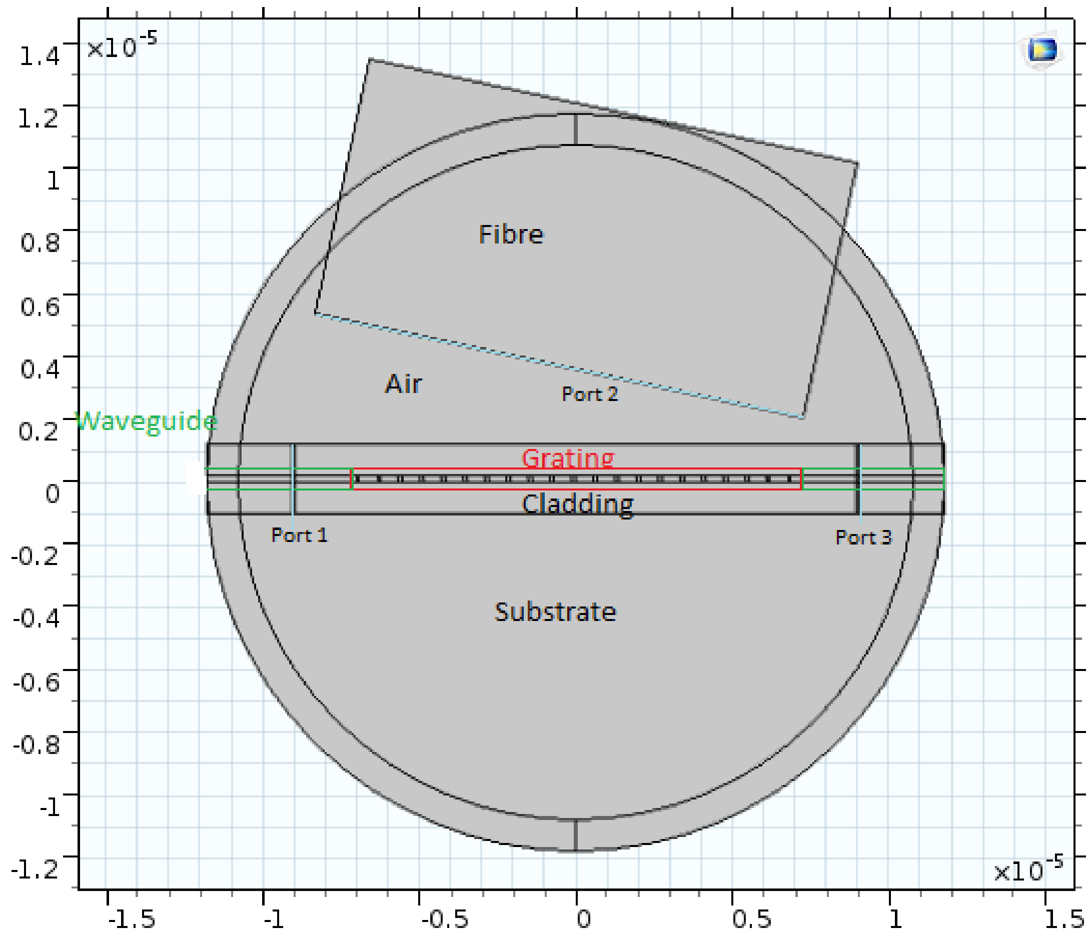

Figure 4.11: The study space for the simulation of the finite grating. The grating is the periodic structure in red, the fibre is the rectangle where the light is detected, air is at the top of the grating, the waveguide is highlighted green before and after the grating, and the substrate is at the bottom of the structure.

Chapter 5

Fabrication Process

Most of the previous work done with optical waveguides at NTNU Nanolab has been made with the the SOI platform and a short-wavelength IR laser source. In this work, a laser at 632.8 nm will be used as the source as this wavelength is more useful for applications such as biological sensing. Visible and near-IR sources enables fluorescence and surface enhanced Raman spectroscopy. Si_3N_4 is therefore taking silicon's place in the SOI structure. Silicon is only transparent for larger wavelengths than 1.1 μm and it is therefore not possible to use silicon which is commonly used in other optical applications. For the visible and near-IR spectrum region, silicon is opaque. This is a feature that is unwanted as it reflects, scatters, or absorbs most light, resulting in no transmitted light.

Another reason why silicon nitride was preferred over silicon in this case, is that its refractive index contrast to SiO_2 is not as high as the index contrast between silicon and SiO_2. This reduces scattering losses and two-photon absorption. Between silicon and SiO_2 the index contrast is $\Delta n = 2$ as opposed to an index contrast of $\Delta n \simeq 0.5$ between SiO_2 and Si_3N_4. A lower refractive index contrast also results in a device more tolerant to fabrication dimension errors. Silicon nitride is compatible with CMOS technology, Romero et al. (2013) [47].

The Si_3N_4 platform is not as well investigated as the SOI, neither at the NTNU Nanolab or in literature. Therefore, much of the work done in this thesis has been on developing and optimising methods using Si_3N_4.

5.1 Fabrication process

First, the scriber machine was used to dice a 4 inch wafer into pieces of 1.5 cm×1.5 cm to ensure that the 1 cm long waveguides will have room in the middle of the sample. The masks were designed not to exceed 1 cm in any direction. The edges may have become damaged throughout the fabrication process making them unsuitable to be part of the waveguide structure.

Next, the samples needed to be covered with the materials SiO_2 and Si_3N_4. The SiO_2 layer was chosen to be 2 μm, see figure 5.1 for a graphic representation of the first step in this process. The PECVD SiO_2-recipe used is found in appendix A, table A.1. The deposition rate needs to be determined by running the recipes multiple times. Before every deposition, a dummy-sample run with the same recipes was done since it is recommended to deposit a layer of approximately 0.2 -0.5 μm as a conditioning step. The sample also had to be properly cleaned with acetone for five minutes in an ultrasonic bath and rinsed with ethanol and isopropanol. This is important to ensure good adhesion as mentioned in section 3.3.1. All chemicals used are listed in table 5.1.

Figure 5.1: SiO_2 PECVD deposition on top of a 500 μm thick silicon wafer. The SiO_2 is 2 μm thick. Not to scale.

The next step in the process was to deposit the 200 nm thick silicon nitride layer, see figure 5.2. This layer will later become the strip waveguide. The recipe in the recipe book at NTNU Nanolab has a HF only process option and a pulsed HF/LF option. The recipe can be found in appendix A, table A.2. It is advised to alter

Table 5.1: List of chemicals used in the NTNU Nanolab.

- Ethanol
- Isopropanol
- Acetone
- CSAR AR-P 6200.13 [9]
- Developer AR 600-546 [41]
- Remover AR 600-71 [42]
- Fomblin oil

the recipe to get the desired film properties. The ratio between SiH_4 and NH_3 can be adjusted to get different refractive indices, but was is not done in this work due to time constraints and down-time on the PECVD machine. The deposition rate was documented to be larger than $10\frac{nm}{min}$. This rate needs to be verified by running the recipe a few times. The recipe states that the resulting film will have low mechanical stress, uniform optical properties and the same properties from run to run.

Figure 5.2: Si_3N_4 PECVD deposition on top of the 2 μm thick SiO_2 film. The Si_3N_4 is 200 nm thick. Not to scale.

The EBL and etching process

With the material structure done, the mask was patterned on the sample. Resist was spun on and soft baked before exposure. After exposure, the resist was developed to remove the resist exposed, leaving some areas without resist which will be etched with ICP-RIE. The sample was fastened to the carrier wafer used during ICP-RIE using fomblin oil. As with the PECVD processes, the ICP-RIE recipes in appendix B need to be tested and an etch rate found. A dummy-run with the recipes was also run first as a conditioning step. Finally, the resist was removed using a remover. Details about all these steps are found in table 5.2 and illustrations are shown in figure 5.3.

Table 5.2: Steps included in the pattering of the sample presented as a recipe.

Step	**Action**
1. Cleaning	Wash the sample with acetone in a ultrasonic bath for 5 min. Rinse with ethanol and isopropanol, blow dry with O_2. Bake at 150 °C for 5 min on a hot plate.
2. Resist coating	Spin coat the sample with CSAR (AR-P 6200.13) for 60 seconds at 4000 rpm for a layer of thickness 0.4 μm.
3. Soft bake	Bake at 150 °C for 1 min.
4. Exposure	Acceleration voltage - 100 kV, beam current - 5 nA, write field size - 1000 μm, number of dots - 500.000, area dose - 350 $\frac{\mu C}{cm^2}$ object aperture - 120 μm, beam diameter - 5 nm.
5. Development	Cover the sample with AR 600-546 for 1 min. Move the sample to a bath of acetone for approx. 1 min and finally into a bath of water.
6. Post-bake (optional)	Bake for 1 min at 130 °C.
7. Etch	Etch with a recipe from appendix B, with the time estimated to get the desired etch depth. Use Fomblin oil to fasten the sample to the carrier.
8. Removal	Pool the sample with remover AR 600-71 for 5 min. Rinse in DI water.

(a) Step 2 and 3 in table 5.2, CSAR 62 is spin coated on the sample followed by a soft-bake.

(b) Step 4, 5 and (6) in table 5.2, the resist is exposed with the EBL and developed with AR 600-546. This can be followed by an optional post-bake.

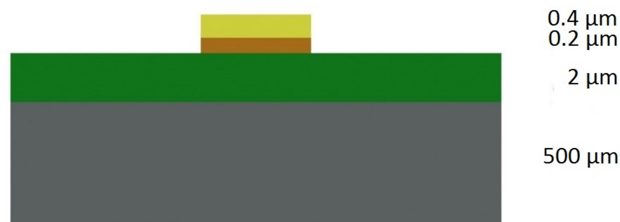

(c) Step 7 in table 5.2, ICP-RIE etch.The exposed Si_3N_4 will be etched away leaving only the waveguide left.

(d) Step 8 in table 5.2, the resist is removed using AR 600-71.

Figure 5.3: Some of the steps in the EBL and etch process, not to scale.

Chapter 6

Results and Discussion

This chapter will present and discuss the results obtained in this thesis. Since some of the work was dependent on the discussion from earlier work, the results and discussion sections are combined to better represent the flow of the work. Results from the simulations are presented first and discussed before presenting the results from the fabrication processes. Thin film deposition, patterning and etch processes are evaluated and discussed.

6.1 COMSOL simulations

To be able to fabricate a working waveguide, the design needs to be optimised. The dimensions, bend-radius and fabrication error sensitivity are important to estimate. Perfect fabrication techniques will not be enough to ensure a working waveguide, the design is equally important.

6.1.1 Waveguide design and propagation loss simulations

Since a 3D model simulation of a waveguide is difficult to perform due to computation, the effective mode index method makes it possible to simulate the waveguide in 2D. As described in section 3.1.1, an effective index was calculated for the three different sections of the waveguide, seen from above. The "Surface integrals" calculated in COMSOL for a waveguide with core width 500 nm are listed in table 6.1. These results were used as input in equation 3.1.1 from section 3.1.1, so for a waveguide with a width of 500 nm and a height of 200 nm, the effective RI in the core region (2,4 and 6) will be $n_eff_{2,4,6} = 1.8503$. Similar, the effective RI in the two areas on the side of the core will be $n_eff_{1,5} = 1.078$. Checking the

effective indices for the other widths, showed that their effective refractive indices were relatively close to 1.85. The effective RI for a core width of 400 nm will be $n_eff_{2,4,6} = 1.842$. This shows that if the width is in the order of 500 nm, 1.85 is a good approximation of the effective RI.

Table 6.1: The "Surface Integrals" ($\iint$) of the electric field distribution in each region of the waveguide as shown in figure 3.1b. The dimensions are 200 nm x 500 nm, height and width respectively. The unit is $\frac{kg^2 \times m^4}{(s^6 \times A^2)}$.

Region	1(3)	2	4	5(7)	6	1 and 5	2,4 and 6	Total
$\iint [10^{-12} \frac{kg^2 * m^4}{(s^6 * A^2)}]$	2.04	4.03	58.20	0.45	9.99	2.49	72.21	77.18

6.1.2 Dimensions

The dimensions of the strip waveguide are important when single-mode condition is required. The height and width need to be carefully chosen. By reading various articles it was interpreted that with air as the cladding, the dimensions 200 nm × 700 nm should only support the first TE and TM modes, TE0 and TM0. In article Subramanian et al. (2013) [45], three dispersion diagrams were shown for Si_3N_4 waveguide at wavelengths 532 nm, 780 nm and 900 nm. These diagrams were studied to find an approximate single-condition width of 700 nm for wavelength 632.8 nm. Dhakal et al. (2014) [15] stated that for free space wavelengths 750-1200 nm, a width of 700 nm yields a single-mode waveguide. It is therefore only used as a guideline for what range the width typically will be. Simulations, showed that 700 nm with a wavelength of 632.8 nm does most likely not give single-mode conditions.

When simulating the waveguide cross-section to find the effective index, the mode profiles were also looked at for the different waveguide widths. The first six modes for a waveguide with a width of 500 nm is shown in figure 4.1 in section 4.1. It was found that 550 nm is the largest width where no guided multi-modes are observed, starting at 700 nm going down with 50 nm intervals until single-mode conditions were found. A multi-mode in the core of a waveguide with a width of 600 nm was found when looking at an electric field plot of the third mode, the mode is shown in figure 6.1. This result is a rough estimate as it only checks for every 50 nm.

The article closest to the single-mode condition found in this thesis is Neutens et at. (2014) [46]. In their work, they found single-mode conditions for a Si_3N_4 strip waveguide with wavelengths 532 nm and 900 nm. For 532 nm, the air cladded waveguide showed single-mode operation up to a core width of 530 nm. For

wavelength 900 nm, it was 1100 nm. The simulations are therefore realistic as the core width for single-mode condition increases with higher wavelengths, resulting in an approximately single-mode condition of a 550 nm core width for a wavelength of 632.8 nm.

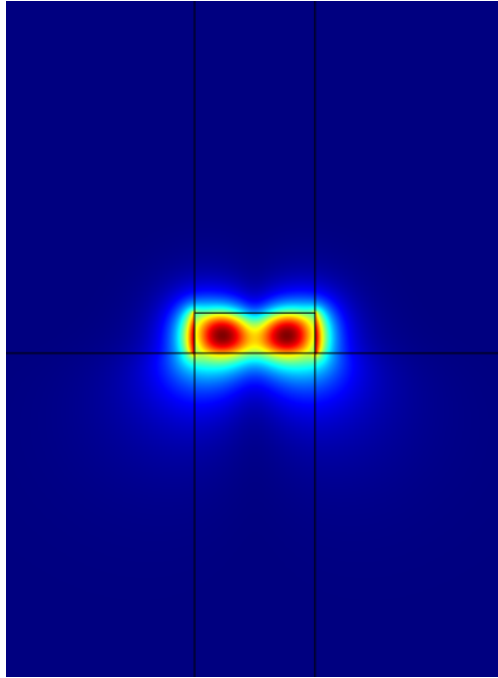

Figure 6.1: The third mode, showing that two modes are guided in the core, for a waveguide with dimensions 200 nm $\times$ 600 nm.

6.1.3 Fabrication effects on a fully etched slot grating coupler

The grating coupler design in the project thesis [16] is shown in figure 6.2. As mentioned, a grating coupler was not fabricated in this work, but further simulations following the work in the project thesis were done to estimate how sensitive the design is to fabrication error. Processes and methods need to be optimised so that the final result is within the dimensions ensuring correct behaviour.

The simulations done in COMSOL showed that with a $\pm$ 5% deviation from the ideal duty cycle, the optimal free space wavelength coupled with the grating was about 40 nm larger or smaller. It can be seen from figure 6.3 that there is an almost linear relationship between the change in duty cycle and free space wavelength.

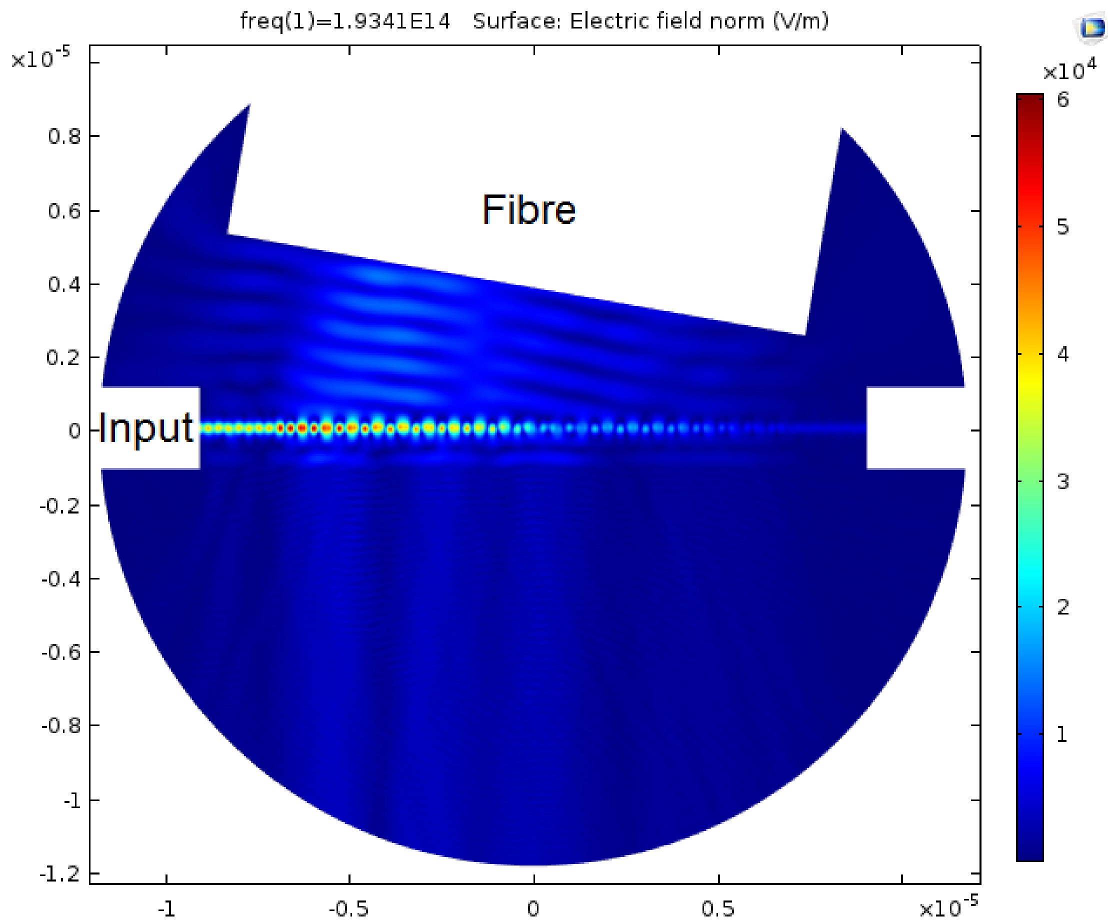

Figure 6.2: A graphic of the simulated gratings normalised E-field. The wave is excited at the input and is coupled out through the grating. The transmitted power is detected at the fibre. This simulation was done in the project thesis [16].

Per 1% change in the duty cycle from the original duty cycle, we got a wavelength shift of 0.68%. This resulted in a change from the optimised simulated free space wavelength of 1550 nm with 10.5 nm per 1% change in duty cycle.

Here the effect of change in incident angle is presented. A change of 1 degree in the incident angle gave a change between + 3.9 and -5.2 nm, as shown in figure 6.4. When the duty cycle is 5% smaller than designed, the change in angle needs to compensate for an approximately 53 nm change in free space wavelength. This is possible because there is a relationship between duty cycle, incident angle and wavelength in free space. It was however shown that it is not possible to change the angle enough to achieve the desired wavelength in free space of 1550 nm when the

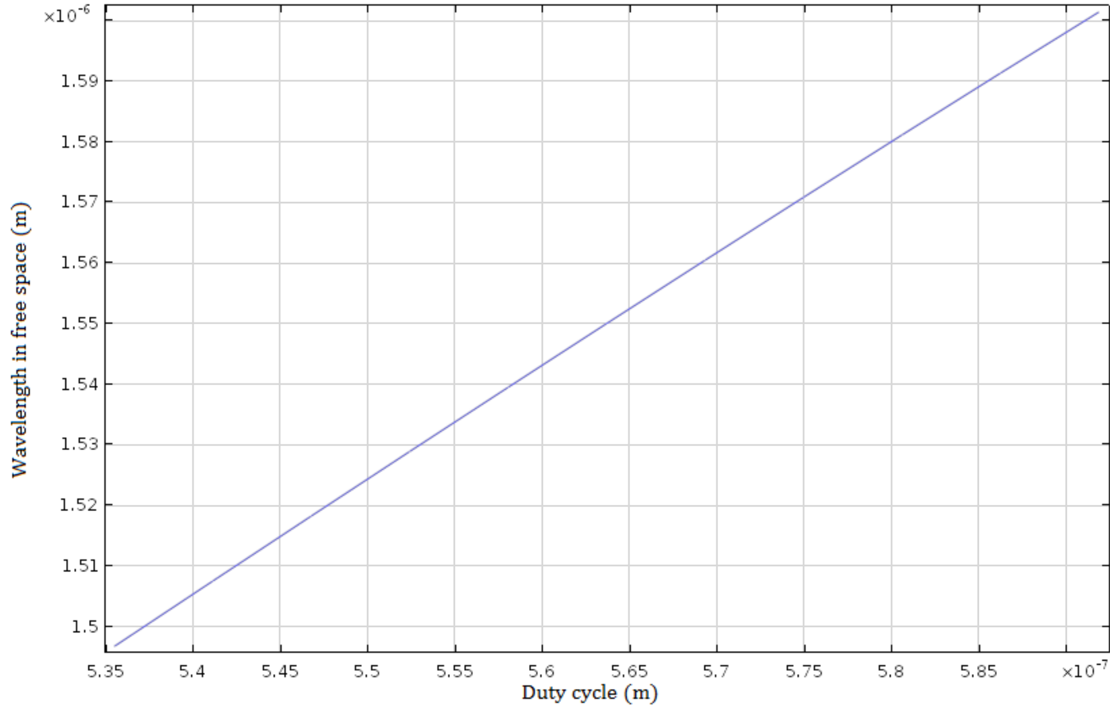

Figure 6.3: Free space wavelength dependence on duty cycle. The total duty cycle shift is ± 5%

duty cycle is 5% too small. It was found that the maximum wavelength achieved with any angle will be 1518 nm when the duty cycle is 5 % smaller than the original design, see figure 6.5. Further simulations showed that only a 2% smaller duty cycle can be compensated with a change in incident angle. For a 5% larger duty cycle than designed, an incident angle of 19° was needed to get a free space wavelength of 1550 nm. For larger duty cycles than the original design, the angle will quickly become very large.

A final simulation showed that if the angle was kept constant, the total light coupled from waveguide to fibre will be significantly reduced in power for each 1% smaller duty cycle, see figure 6.6. The results found in the simulations showed that the grating is quite sensitive to fabrication error as the duty cycle can only be 2% smaller than the original design in this work, before the angle can not compensate for the error. A tunable laser can be a solution as this will not require a change in incident angle.

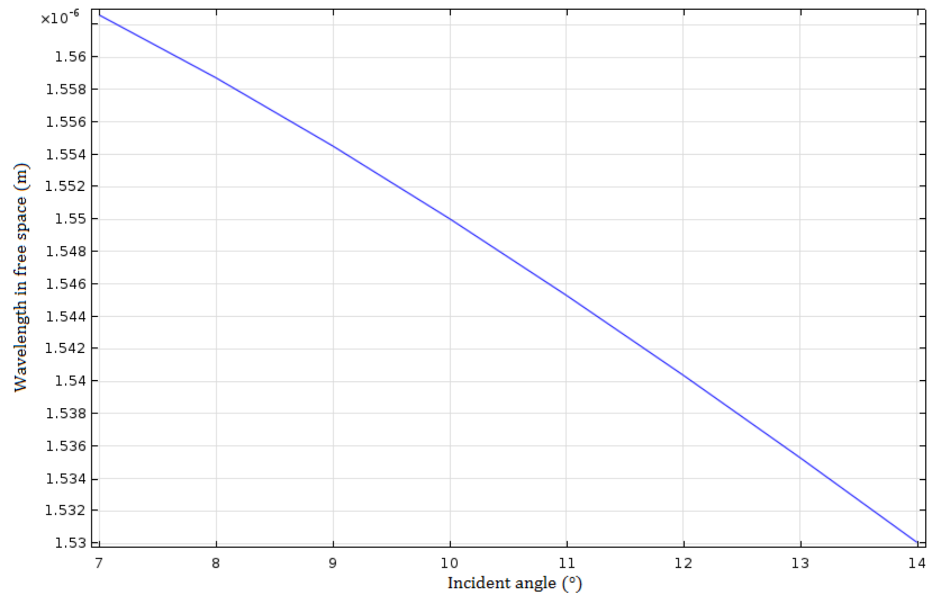

Figure 6.4: Free space wavelength dependence on incident angle.

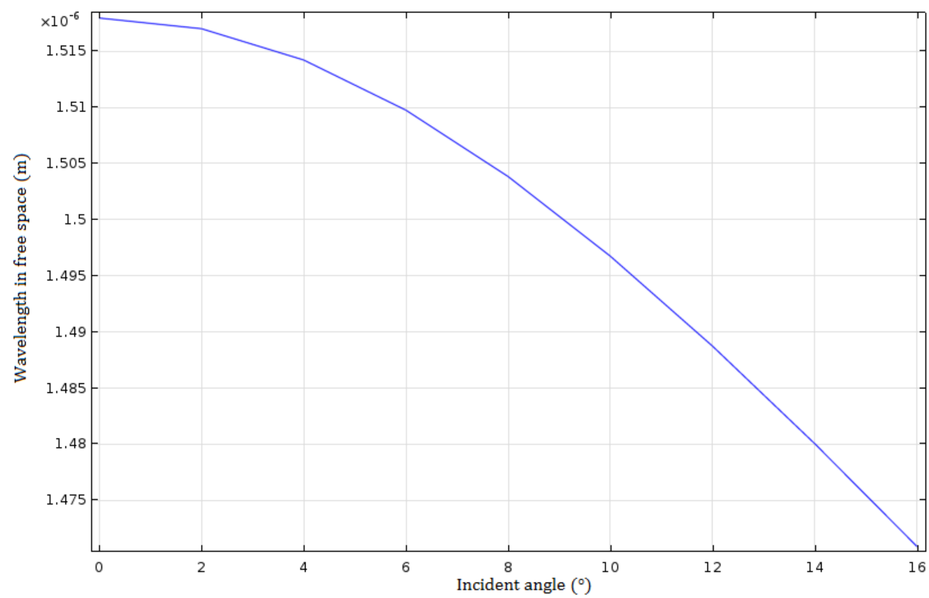

Figure 6.5: Plot of incident angle vs. the wavelength in free space when the duty cycle is 5% smaller than original design duty cycle of 535.52 nm.

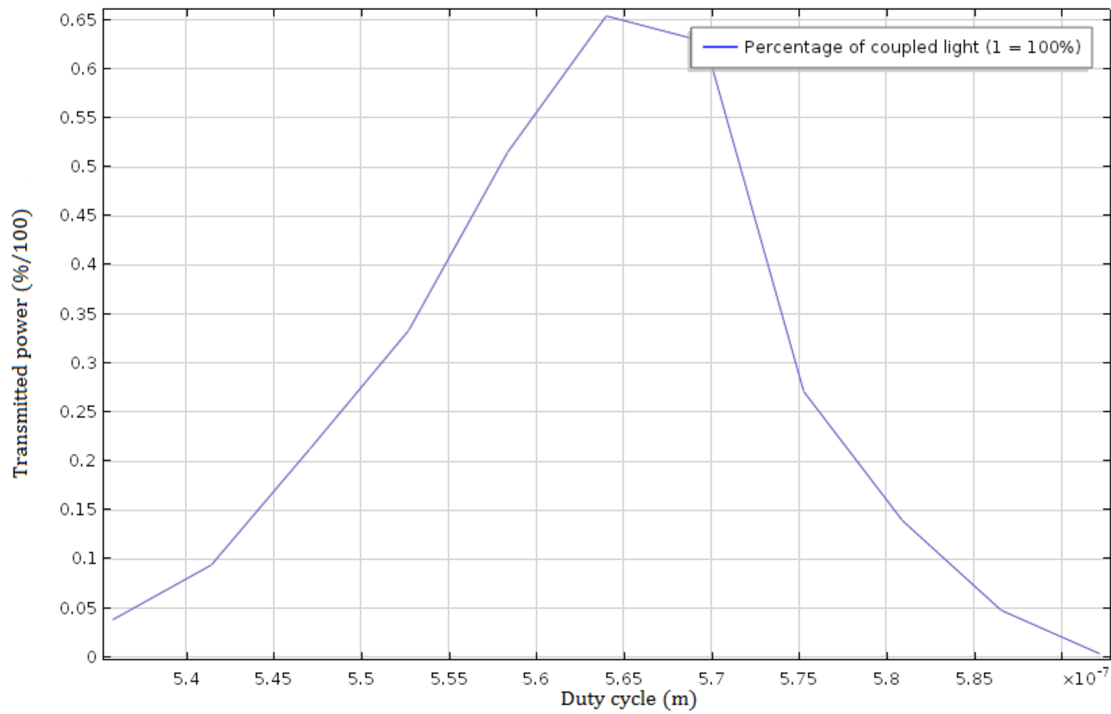

Figure 6.6: Duty cycle vs. the percentage of light coupled from the waveguide to the fibre.

6.2 Processes and fabrication

A significant part of the work done in this thesis is performed in the NTNU Nanolab. This section will present the results obtained in the cleanroom and discuss these.

6.2.1 Silicon dioxide deposition

The first layer deposited was the SiO_2 film. The cladding target thickness was designed to be 2 μm. The growth rate is therefore investigated to achieve this thickness. The recipe used is found in appendix A, table A.1. The recipe has been used and investigated by other PECVD users, so the growth rate was easy to obtain. The growth rate was approximately 1.25 $\frac{nm}{s}$, which is 75 $\frac{nm}{min}$. The first run, sample 1, was run for 26 min and 33 s. The sample numbers and their growth times and thicknesses are presented in table 6.2 and a full overview is found in appendix C, figure C.1. The results show that the growth time of sample 1 gave the desired thickness. The thickness was measured at the centre of the sample and towards the edges. This showed that the film was a little thicker towards the edge. The recipe does not give a perfectly uniform film. A uniform film is a desired feature.

Table 6.2: Growth times and the thicknesses of SiO_2 measured by the reflectometer. The thickness is measured at the centre of the sample and the number in the parenthesis is the thickness measured towards the edge of the sample.

Sample no	**Growth time**	**Thickness**
1	26 min + 33 s	1995 nm (2055 nm)
2	26 min + 34 s	1998 nm (2083 nm)
3	26 min + 34 s	2004 nm (2068 nm)
4	26 min + 34 s	1994 nm (2042 nm)
5	26 min + 34 s	1999 nm (2072 nm)
6	26 min + 34 s	1996 nm (2081 nm)

The thickness of the SiO_2 layer for sample 1 found using the reflectometer was also verified by looking at the cross-section in the S(T)EM. A photo was taken of the region where the SiO_2 thickness was most apparent and this photo is shown in figure 6.7. An exact thickness was difficult to obtain but it verifies that the SiO_2 will at least have a thickness larger than 1.5 μm which is the minimum cladding thickness to achieve no power leakage to the substrate.

Figure 6.7: A cross-section picture of sample 1. The sample here is shown upside down with the SiO_2 film on the top and the Si_3N_4 film at the bottom.

The next run was done with five samples in the PECVD chamber, sample 2-6 in table 6.2. The recipe seems to be constant from run to run since it gave approximately the same thickness for the same time. This verifies the repeatability.

Morten Hage, a fellow master student, checked the surface roughness of a SiO_2 film deposited in a separate run but with the same growth time as sample 2-6. He used the AFM equipment and found an average roughness for SiO_2 of 3.1 nm compared to 0.17 nm for silicon (wafer) and 0.44 nm for Si_3N_4. This large roughness is undesirable. During the deposition of the SiO_2 for this sample, the pump in the PECVD stopped working as it should, so there might have had an effect on the SiO_2 resulting in such a large surface roughness. A high surface roughness might have caused the Si_3N_4 to be deposited unevenly creating propagation losses such as scattering loss in the waveguide. There are evidence that the recipe A.1 in appendix C creates films with high surface roughness, so some cleanroom users buy silicon wafer with a thermally grown SiO_2 film already deposited on top with lower surface roughness.

6.2.2 Silicon nitride deposition

In this thesis, a recipe proposed by Oxford instruments was used. The target thickness was designed to be 200 nm. To find the deposition rate, a 10 min process with the recipe in appendix A, table A.2 was done. A film of 145.38 nm was deposited, checked with the reflectometer. The growth rate is then 0.2423 $\frac{nm}{s}$. Next, samples 7-9 in table 6.3 were processed. The final growth rate found was $0.254\frac{nm}{s}$, ending with 13 min and 7 s as the ideal time for achieving 200 nm of Si_3N_4. It seems like the growth rate slows down somewhat over time, this is why it is important to check each time for each new thickness fabricated.

Table 6.3: Growth times and the thickness of Si_3N_4.

Sample no	Growth time	Thickness
-	10 min	145.38 nm
1	13 min + 8 s	Approx 200 nm
2-6	13 min + 7 s	Approx 200 nm
7	14 min + 32 s	223.5
8	13 min	198.7 nm
9	13 min + 20 sec	204.8 nm

To verify the thickness of the Si_3N_4 film, the film was deposited directly on to the silicon wafer. This was done because the reflectometer could not measure the SiO_2 and Si_3N_4 thicknesses simultaneously. For sample 1, the reflectometer measured 181 nm for the Si_3N_4 and 2031 nm SiO_2. Since this measurement was performed in the centre of the sample, which earlier was measured to be 1995 nm for the SiO_2 layer, it looked like the reflectometer struggled to find the exact transition from one material to the other. This is possible because the RI contrast is low, only $\Delta = 0.5$. The index contrast between silicon and Si_3N_4 is higher, making it a more accurate measurement. This is however the reason why it says approx. in table 6.3 for some of the thicknesses. It was therefore easier to look at the Si_3N_4 in the S(T)EM when it was deposited directly on to the silicon wafer, see 6.8.

The Si_3N_4 recipe

The same recipe was used for all samples and was not optimised in the framework of this project due to time constraints. It was not possible to carry out much optimisation on the PECVD recipes as the PECVD had a couple of months downtime. A literature study was therefore conducted to find important features and parameters for future work. The process sheet detailing the recipe gave a pulsed

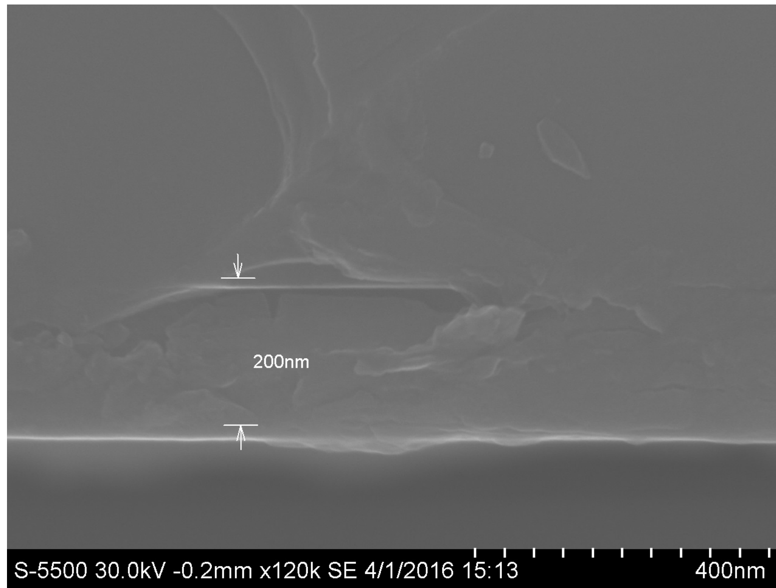

Figure 6.8: A S(T)EM photo of the cross section of a 200 nm Si_3N_4 layer on top of a silicon wafer, sample 8.

LF/HF option, presented in table A.2 in appendix A. It is stated in the process sheet found in NTNU Nanolab by Oxford Instruments, that the ratio between SiH_4 and NH_3 affects the RI of the Si_3N_4. This was further confirmed by Oxford Instruments PECVD documentation [48] and by Gorin et al. (2008) [35]. Gorin found a relationship between the ratio NH_3/SiH_4 and the refractive index, absorption coefficient and the propagation loss. The article also looked at the consequences depending on the use of either a LF or HF process. The results showed that a higher refractive index normally meant a higher absorption coefficient and propagation loss, especially when using HF. Their conclusion was that thin films deposited with LF-PECVD have better optical properties in the visible range (633 nm) [35].

Other work which deposit Si_3N_4 with PECVD was Wang et al. (2015) [24], using a HF process with SiH_4:NH_3 = 25:40 sccm at 300°. A larger HF power is shown in Oxford Instruments (2003) [48] to result in a higher deposition rate, lower frequency, lower uniformity rate and lower film stress. Larger NH_3:SiH_4 ratios would on the other hand give a larger film stress. From [35], [24] and [48], a trade-off must be found between having a high refractive index and low film stress, and low propagation loss which is a result of a larger ratio.

6.2.3 Electron beam lithography procedure

A 400 nm thick CSAR AR - 6200.13 was spun on the samples following the steps in table 5.2. The Elionix EBL was available at the NTNU Nanolab from February 2016. A beam current of 5 nA was selected because this would ensure a large enough resolution for the structures designed. Bojko et al. (2011) [49] and Yagnyukova (2013) [50] have fabricated similar sized structures as the ones in this thesis, and they have used beam currents of 5 nA and 2 nA. The bends were the most crucial part of the structure. By looking at figure 6.9, the bend looks smooth, with no sharp edges.

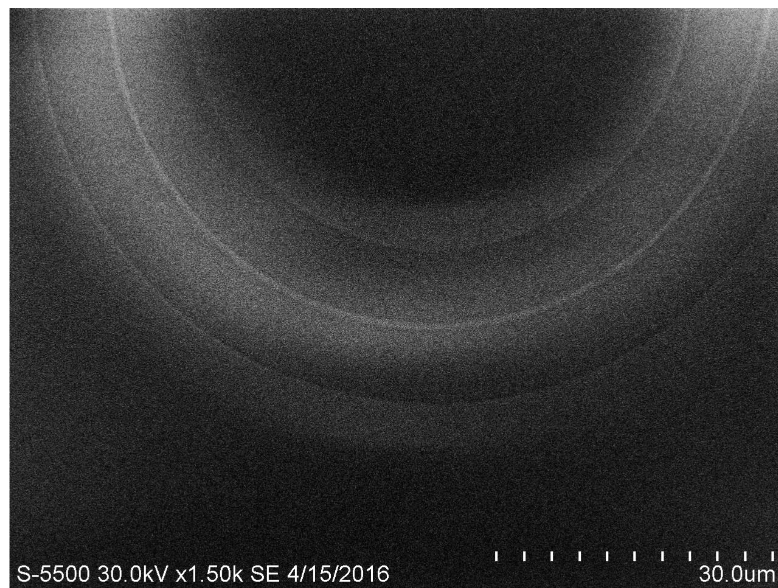

Figure 6.9: A S(T)EM photo of sample 1, a waveguide with a bend radius of 35 μm.

Figure 6.10 shows a section of the waveguide for sample 1 and 6. Small dirty spots can be seen next to the structures. These may arise from underexposure. The dose used for the first few samples was 300 $\frac{\mu C}{cm^2}$, including sample 1 in figure 6.10a. By studying the figure, dirty spots with an approximate diameter of 100-250 nm are observed. The edges of the waveguide are also very uneven with bumps which also can be a sign of underexposure. The developer does not function as it should if the resist is not correctly exposed. Overexposure could lead to changes on the structure, like undercuts and other features ruining the intended shape of the waveguide.

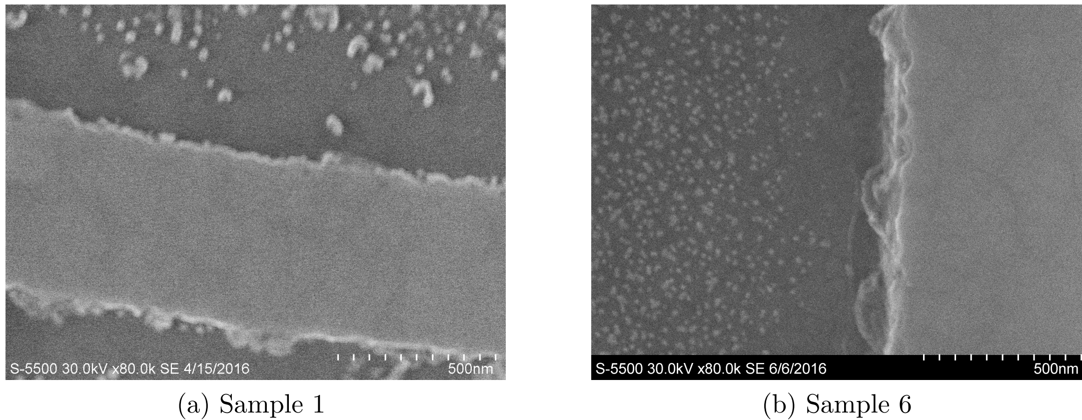

(a) Sample 1 (b) Sample 6

Figure 6.10: S(T)EM picture of sample 1 and sample 6 showing a section of the waveguide.

Master student Lars Grønmark Holmen performed a study on various exposure doses and beam currents. He found that with a 500 nm thick resist, 300 $\frac{\mu C}{cm^2}$ showed signs of underexposure. The smallest dose found that did not show signs of underexposure were 350 $\frac{\mu C}{cm^2}$. Therefore, samples 6 and 8 where exposed with 350 $\frac{\mu C}{cm^2}$. The S(T)EM photo of sample 6 in figure 6.10b still show dirty spots, but to a lesser extent. The spots were found to be approximately 50-100 nm in diameter.

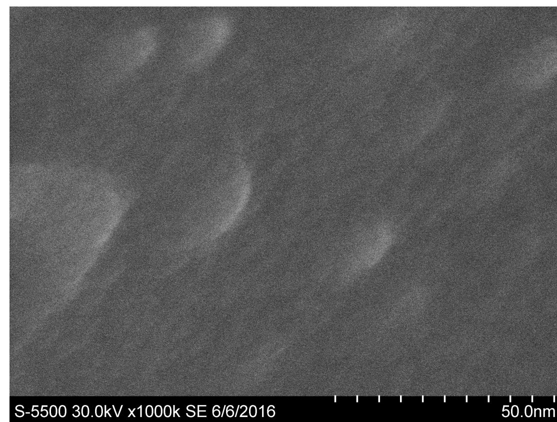

Figure 6.11: A S(T)EM photo of sample 6, a close up of the dirty spots found in the exposed areas next to the waveguide.

6.2.4 Etching procedure

Not all samples gave good photos when studied with the S(T)EM due to charge effects discussed later. To study the etch recipes found in appendix B both a cross-section study and a study looking from above were done. Only two samples that gave good photos when looking at the cross-section were samples 1 and 8. The cross-section photos taken of the waveguide edge are shown in figure 6.12. The etch recipe used on sample one is called (Jens) nitride etch and it is shown that it has an etch rate of 1.9 $\frac{nm}{s}$. It was found by running dummy etch on a sample with a nitride film with a known thickness. The thickness was again measured after the etch. This was the only etch process run with the ICP-RIE chiller. All other runs were run on the ICP-RIE cryo machine using hydrogen cooling.

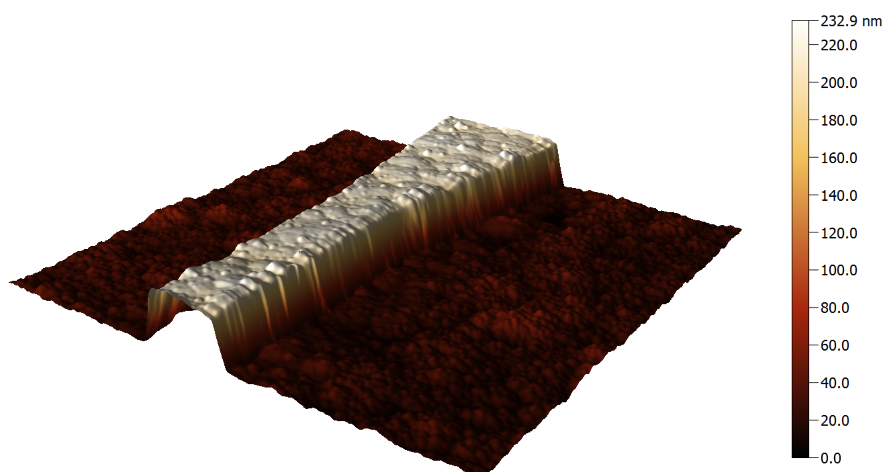

Figure 6.12: An AFM photo of sample 2 showing the taper and part of the main waveguide. The height of the waveguide was found to be 183 nm.

Master student Morten Hage (MH) needed an etch with a lower etch rate because he is only etching about 30 nm which is much less than 200 nm which is the targeted height in this thesis. Therefore a second etch recipe, (Peter) Si_3N_4 etch (OI) was investigated. The first rate found was 1.6 $\frac{nm}{s}$ which is only marginally smaller than the previous recipe. MH checked sample 2 to estimate how much was etched. It was found that the height of the waveguide was only 183 nm, which is smaller than the desired height of 200 nm. The Si_3N_4 film was verifyed through an inspection in the S(T)EM, so it was likely that the etch rate is slower than expected. The new etch rate was then calculated to be 1.385 $\frac{nm}{s}$. This rate was used when processing samples 6 and 8. The result is shown in 6.13b. The etch looks like it was etched all the way down creating an anisotropic shape, but for

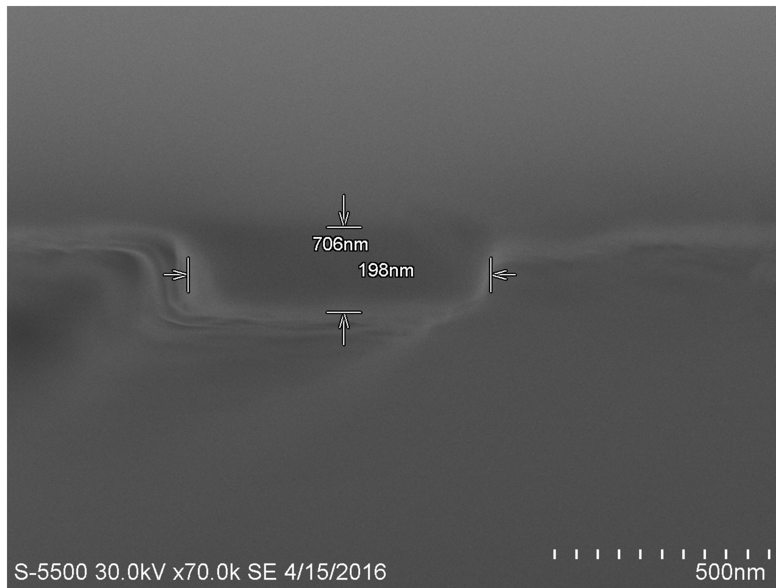

(a) A cross-section S(T)EM photo of sample 1 showing the end of the waveguide and its dimensions (upside down).

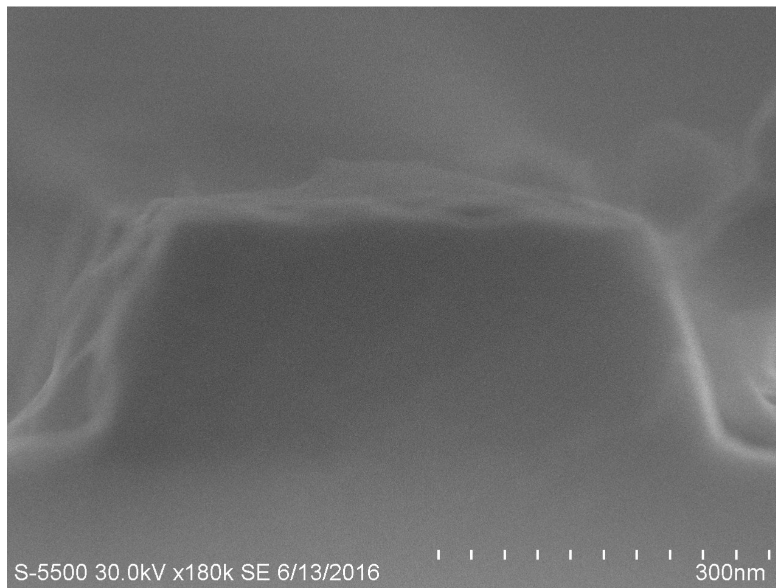

(b) A cross-section S(T)EM photo of sample 8 showing the end of the waveguide.

Figure 6.13: Cross-section S(T)EM photos of samples 1 and 8.

both samples the walls were not 90°. They are also quite ”round” at the bottom. There are signs of edge roughness on the sides and some roughness on the top. This can also be observed in figure 6.10 The roughness might be due to poor etch or Si_3N_4 recipe. The high surface roughness found in the SiO_2 film could also cause roughness in the Si_3N_4 film. It is important to reduce this sidewall roughness as it leads to high scattering losses.

As mentioned earlier, it was quite difficult to get good photos of the sample. If Si_3N_4 was the only material exposed by the beam, strange effects like the ones that can be seen in figure 6.14 were observed. This was much due to a charge effect disturbing the S(T)EM characterisation. Wibbeler et al. (1998) [51] state that if parasitic charges come onto the dielectric layer of the sensor in an uncontrolled manner during handling and operation, they inevitably distort the electric field and change the device characteristics. It was demonstrated in Subramanian et al. (2013) [45] and Khanna et al. (2014) [52] that depositing a thin layer of gold prior to S(T)EM characterisation can reduce the charging effect.

Figure 6.14: A S(T)EM photo where charge effects can be seen.

While inspecting sample 8 in a microscope after resist removal, a section quite in the middle of the sample did not have complete waveguide structures. Figure 6.15a shows the part of the sample which looked good and figure 6.15b shows the part of the sample where something were not fabricated correctly. Looking at the

figures, the broken section looks much dirtier than the one with the intact one. Since the deposition of Si_3N_4 is not 100% uniform, the film was likely to be thinner in the middle. The etch could have only managed to etch all the way down in this specific area. If the Si_3N_4 is not properly adhered to the underlying SiO_2 film, the part where the waveguide was etched all the way down could have been broken off, either during the etch process step or during the ultrasonic resist remover bath. Figures 6.15d and 6.15c show S(T)EM photos taken of two different places on sample 8 where part of the waveguide was missing. The reason why this happened is not verified due to time constraints.

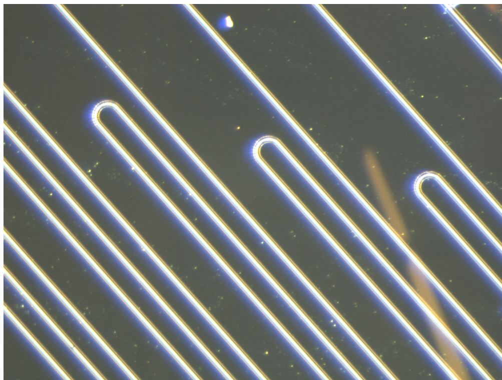

(a) Properly fabricated waveguide on sample 8

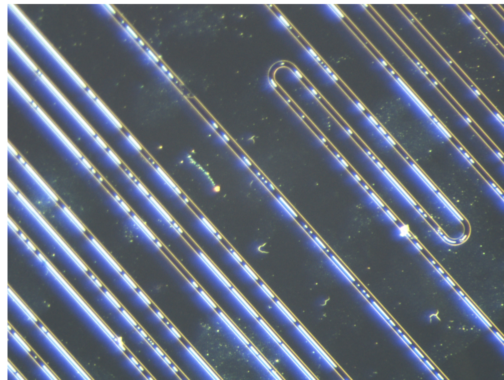

(b) The part of sample 8 where the waveguides are damaged.

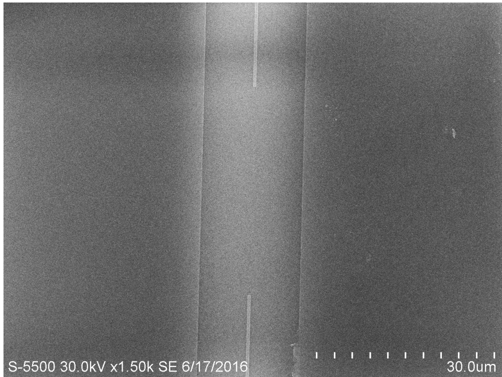

(c) A photo of a section where it should have been a complete waveguide.

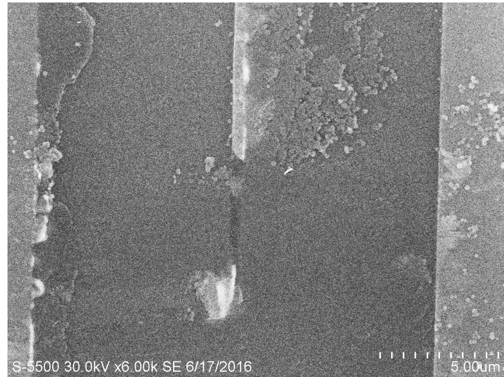

(d) A part of the waveguide where a part of it is missing.

Figure 6.15: Photos of sample 8 taken with an optical microscope and photos of the broken waveguides taken in S(T)EM.

6.3 Characterisation and coupling

It was hoped that the work would result in functioning waveguides, but there is still work to be done. Using the setup in the laser characterisation lab, three samples were tested using the newly configured 632.8 nm laser. The setup was originally built for an IR source, so the setup was reconfigured for a visible laser source. A fibre was connected to the laser and since the polarisers are designed to work for IR light, these were not included and the 632.8 nm laser was connected directly to the tapered fibre. We could see that this worked, as it is easy to see visible light.

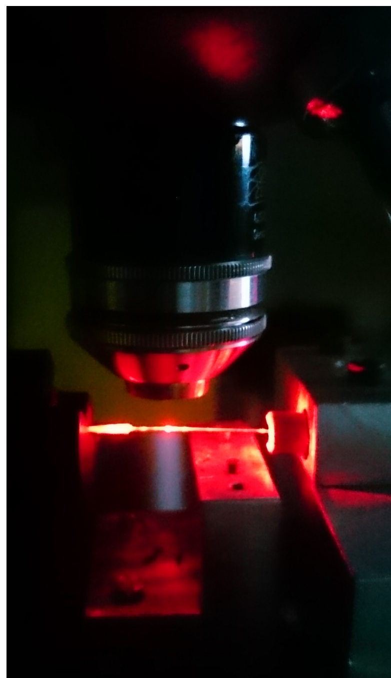

(a) The coupling setup where the left fibre is the fibre coupling light into a sample and the right fibre couples light out.

(b) The two fibres in close proximity to test a direct coupling.

Figure 6.16: Direct fibre coupling configuration.

A coupling test was done to try and directly couple the input fibre to the output fibre. This was done to check if the output fibre could couple visible light and further see if the photo-detector could detect it. The setup is shown in figure 6.16a. The two fibres were brought in very close proximity to each other and the vertical and horizontal distance adjusted to try and see if any light came out of the output fibre. It was very difficult to get the correct alignment for coupling. Eventually

some light appeared at the output of the output fibre but when the photo-detector was connected, it could not detect the signal to any large degree. In figure 6.16b, one can see the two fibres. The input fibre is now on the left as the camera inverts the image. A bright red spot can be seen. Some of the light appears to be coupled into the output fibre.

Table 6.4: Description of samples investigated in the coupling experiments.

Sample no	Coupling type	Waveguide type
6	Normal waveguide	Strip
8	Adiabatic taper	Strip
MH	Normal waveguide	Rib

Without the photo-detector being able to detect the transmitted visible light very well, no proper characterisation could be done. It was however possible to see with the IR camera if light coupled into the sample, to some extent. A photo-detector being able to detect light with wavelength 632.8 nm could have been easy to obtain but time did not permit further configurations to be done. The samples we tried to couple light into are listed in table 6.4. One of the Si_3N_4 samples fabricated by Morten Hage, MH, was a rib waveguide, not a strip. The testing was done by the author with support from Jens Høvik.

Samples were fastened to a sample-holder, which is shown in figure 6.17. The holder was then placed on the stage between the two fibres. The only sample where it was possible to see evidence of some light being coupled into the sample was the rib waveguide. The light was coupled in but it rapidly faded. The propagation of the light in the rib waveguide is shown in figure 6.18. This might indicate that there is much loss in the Si_3N_4 and that recipe needs to be improved as discussed in section 6.2.2.

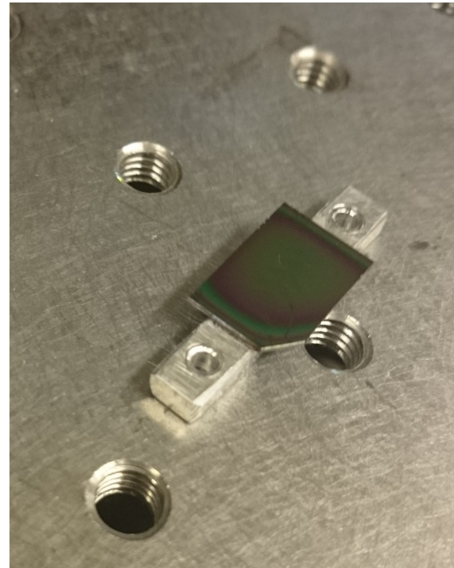

Figure 6.17: The sample holder.

It was expected to be more difficult to couple light into samples 6 and 8, as these are strip waveguides. This means

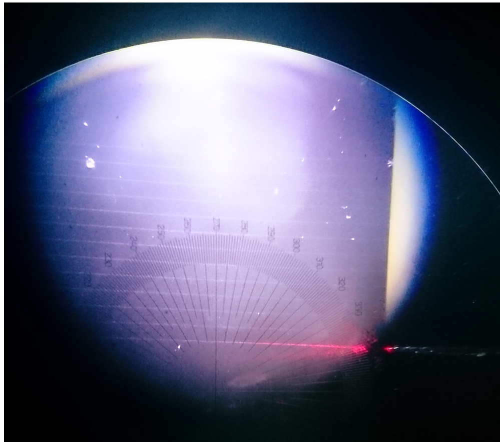

(a) When coupling to sample MH, the red light is observed to propagate a short distance. The photo is taken through the IR camera lens. The thin white horizontal lines are rib waveguides.

(b) The light coupled to sample MH.

Figure 6.18: The coupling achieved into the rib waveguide.

that the cross-section of the waveguide is smaller than a rib waveguides. The consequence of this is a larger difference in spot-size between the fibre and the waveguide resulting in more loss. Sample 8 had a taper with a core width of 5 μm to make coupling easier but there might be too much loss in the taper for the light to propagate. Another factor was that the scriber line did not look very good. It was not straight and the edges looked flaked. The strip waveguides and the experimental setup were not ready for proper characterisation. However, to see some light propagating in the Si_3N_4 waveguide using a laser source at 632.8 nm is very promising.

Chapter 7

Conclusions

The motivation for this thesis was to design, fabricate and characterise silicon nitride nanophotonic components to be part of an interferometric biosensor. These biosensors have the potential to become a highly sensitive, selective and robust miniaturised diagnostic device. Prior to this work, silicon has been the main choice when fabricating optical waveguides at NTNU Nanolab so initial research on Si_3N_4 was performed.

Designing a waveguide structure in Si_3N_4 and simulating loss in bends were the first work done in this thesis. The design and simulations have been carried out using COMSOL Multiphysics and literature has been used as inspiration and support. Finding the single-mode conditions, bend radiuses and taper-dimensions were done to achieve an optimal waveguide for further waveguide characterisation. For a Si_3N_4 waveguide with SiO_2 cladding and air top-cladding, the largest core width found giving single-mode conditions with a core height of 200 nm, was 550 nm.

Finding ways to experimentally characterise these structures was one of the main goals of this thesis. Masks were designed so propagation, surface roughness, bend and taper losses could be found. The paper-clip method was proposed as a test layout for propagation loss investigation. Bend radius and surface roughness losses were found by measuring propagation loss on various bend radiuses and waveguide core width respectively. Tapers were added to easier couple light from the single-mode fibre to the waveguide. A long taper was designed to ensure adiabatic behaviour.

Further simulations performed on the grating coupler showed that the transmitted power was quite sensitive to fabrication errors. It was however found that it is possible to compensate with either a change in incident angle of the in-coupled

light or using a tunable laser source. Optimising fabrication methods are therefore very important when making detailed components since these methods have limited effect. Only a 2% smaller duty cycle than originally designed will make the grating useless if a tunable laser source is not available.

Work on configuration of the characterisation lab was started. Characterisation of the photonics component was not successful due to large losses in the Si_3N_4 film, difficult coupling from a larger spot size to the small strip waveguide and that the experimental setup was not fully optimised to work for the visible laser source. Further, when coupling light into Si_3N_4 rib waveguide fabricated by Morten Hage, some light was seen propagating but faded quickly. The SiO_2 film was shown to have large surface roughness which could affect the Si_3N_4 waveguide because of large scattering losses. The Si_3N_4 recipe should also be optimised to achieve better optical properties.

A 300 $\frac{\mu C}{cm^2}$ exposure dose was found to create many dirty spots on the SiO_2 surface. A higher dose of 350 $\frac{\mu C}{cm^2}$ was therefore tried resulting in smaller dirty spots. The etch looked anisotropic, but it did not produce 90° wall. The walls were also quite rounded at the bottom. By investigating the walls of the waveguide in the S(T)EM, large surface roughness of 3.1 nm was observed caused either by the etch or poor PECVD recipes.

7.1 Future work

It is hoped that this work will be useful for further work involving design, fabrication and characterisation of Si_3N_4 waveguides. Here, a few key things which are suitable for future work are listed.

- Find ways to decrease the surface sidewall roughness through improving the etch process.
- Decrease the propagation and scattering loss in the Si_3N_4 by improving the PECVD Si_3N_4 recipe.
- Optimise the characterisation setup for a laser with wavelength 632.8 nm.
- Investigate why some waveguides were broken.

Acronyms

AFM	atomic-force microscopy.
BF	bright field.
BSE	backscattered electron.
CVD	chemical vapour deposition.
DF	dark field.
DI	distilled.
EBL	electron beam lithography.
EM	electromagnetic.
FEM	finite element method.
HF	high frequency.
ICP	inductively coupled plasma.
ICP-RIE	inductively coupled plasma-reactive ion etching.
IPA	isopropanol.
IR	infra-red.
LF	low frequency.
LPCVD	low-pressure chemical vapour deposition.
MH	Morten Hage.

PECVD plasma enhanced chemical vapour deposition.

PML perfectly matched layers.

RF radio frequency.

RI refractive index.

S(T)EM scanning (transmission) electron microscope.

SE secondary electron.

Si_3N_4 silicon nitride.

SiO_2 silicon dioxide.

SOI silicon-on-insulator.

TE transverse electric.

TEM transverse electromagnetic.

TM transverse magnetic.

Bibliography

[1] B. E. Saleh, M. C. Teich, and B. E. Saleh, *Fundamentals of photonics*. John Wiley & Sons, 1991.

[2] X. Tong, *Advanced Materials for Integrated Optical Waveguides*, ch. 2 Characterization methodologies of optical waveguides, pp. 65–66, 71–72. Springer International Publishing, 2014.

[3] W. Li, S. E. Webster, R. Kumaran, S. Penson, and T. Tiedje, "Optical wave propagation in epitaxial Nd:Y2O3 planar waveguides," *Appl. Opt.*, vol. 49, pp. 586–591, Feb 2010.

[4] C. Peng and W. A. Challener, "Input-grating couplers for narrow gaussian beam: influence of groove depth," *Opt. Express*, vol. 12, pp. 6481–6490, Dec 2004.

[5] J. C. Wirth, *Silicon grating couplers for low loss coupling between optical fiber and silicon nanowires*. PhD thesis, Purdue University West Lafayette, 2011.

[6] O. Instruments, "Plasma enhanced chemical vapour deposition." "http://www.oxford-instruments.com/products/etching-deposition-and-growth/plasma-etch-deposition/pecvd". Online; accessed 15.03.2016.

[7] O. Instruments, "Inductively coupled plasma (ICP) etch." "http://www.oxford-instruments.com/products/etching-deposition-and-growth/plasma-etch-deposition/icp-etch". Online; accessed 30.03.2016.

[8] M. A. McCord and M. J. Rooks, "Spie handbook of microlithography, micromachining and microfabrication," in *SPIE, Bellingham*, 2000.

[9] "Positive e-beam resists AR-P 6200." "http://www.allresist.com/wp-content/uploads/sites/2/2015/12/allresist_produktinfos_ar-p6200_englisch.pdf". Online; accessed 22.04.2016.

[10] A. Heinze, "S(T)EM introduction course." "http://www.ntnu.no/nanolab".

[11] "Ultra-high resolution scanning electron microscope s-5500." "http://www.spectral.se/spectral.nsf/f164f3e9b82f0febc1256dcc004611c1/973be1ca97284456c1256f4a007aadc6/$FILE/S-5500%20brochure.PDF". Online; accessed 11.04.2016.

[12] "Key enabling technologies." "http://ec.europa.eu/growth/industry/key-enabling-technologies/index_en.htm". Online: accessed 12.06.2016.

[13] L. Tsybeskov, D. J. Lockwood, and M. Ichikawa, "Silicon photonics: CMOS going optical [scanning the issue]," *Proceedings of the IEEE*, vol. 97, no. 7, pp. 1161–1165, 2009.

[14] A. González-Guerrero, S. Dante, D. Duval, J. Osmond, and L. M. Lechuga, "Advanced photonic biosensors for point-of-care diagnostics," *Procedia Engineering*, vol. 25, pp. 71–75, 2011.

[15] A. Dhakal, P. Wuytens, F. Peyskens, A. Z. Subramanian, N. Le Thomas, and R. Baets, "Silicon-nitride waveguides for on-chip raman spectroscopy," in *SPIE Photonics Europe*, pp. 91411C–91411C, International Society for Optics and Photonics, 2014.

[16] I. Knain, "Silicon nanophotonic biosensor," 2016.

[17] G. Lifante, *Integrated phonics: Fundamentals*. John Wiley & Sons, 2003.

[18] J. S. Levy, *Integrated nonlinear optics in silicon nitride waveguides and resonators*. PhD thesis, Citeseer, 2011.

[19] F. Grillot, L. Vivien, S. Laval, D. Pascal, and E. Cassan, "Size influence on the propagation loss induced by sidewall roughness in ultrasmall SOI waveguides," *Photonics Technology Letters, IEEE*, vol. 16, no. 7, pp. 1661–1663, 2004.

[20] A. Melloni, R. Costa, G. Cusmai, and F. Morichetti, "The role of index contrast in dielectric optical waveguides," *International Journal of Materials and Product Technology*, vol. 34, no. 4, pp. 421–437, 2009.

[21] W. Bogaerts, R. Baets, P. Dumon, V. Wiaux, S. Beckx, D. Taillaert, B. Luyssaert, J. Van Campenhout, P. Bienstman, and D. Van Thourhout, "Nanophotonic waveguides in silicon-on-insulator fabricated with CMOS technology," *Lightwave Technology, Journal of*, vol. 23, no. 1, pp. 401–412, 2005.

[22] H. O. Pierson, *Handbook of chemical vapor deposition: principles, technology and applications*. William Andrew, 1999.

[23] I. Goykhman, B. Desiatov, and U. Levy, “Ultrathin silicon nitride microring resonator for biophotonic applications at 970 nm wavelength,” *Applied Physics Letters*, vol. 97, no. 8, p. 081108, 2010.

[24] J. Wang, Z. Yao, and A. Poon, “Silicon-nitride-based integrated optofluidic biochemical sensors using a coupled-resonator optical waveguide,” *Front. Mater. 2: 34. doi: 10.3389/fmats*, 2015.

[25] Y. Fu, T. Ye, W. Tang, and T. Chu, “Efficient adiabatic silicon-on-insulator waveguide taper,” *Photonics Research*, vol. 2, no. 3, pp. A41–A44, 2014.

[26] P. S. J. Russell, “Optics of floquet-bloch waves in dielectric gratings,” *Applied Physics B*, vol. 39, no. 4, pp. 231–246, 1986.

[27] COMSOL, “Introduction to COMSOL multiphysics.” ”`http://cdn.comsol.com/documentation/5.1.0.234/IntroductionToCOMSOLMultiphysics.pdf`”, 1998-2015. Online; accessed 10.12.2015.

[28] M. Herlitschke, M. Blasl, and F. Costache, “Efficient simulation of 3D electro-optical waveguides using the effective refractive index method,” in *Proceedings of the 2011 COMSOL Conference in Stuttgart, Germany*, 2011.

[29] G. B. Hocker and W. K. Burns, “Mode dispersion in diffused channel waveguides by the effective index method,” *Appl. Opt.*, vol. 16, pp. 113–118, Jan 1977.

[30] D. R. Lim, *Device integration for silicon microphotonic platforms.* PhD thesis, Massachusetts Institute of Technology, 2000.

[31] M. F. A. Muttalib, R. Y. Chen, S. Pearce, and M. D. Charlton, “Tapered nanowire waveguide layout for rapid optical loss measurement by’cut-back’technique,” in *SPIE LASE*, pp. 86040Z–86040Z, International Society for Optics and Photonics, 2013.

[32] L. Yin, *Study of nonlinear optical effects in silicon waveguides.* PhD thesis, University of Rochester, 2009.

[33] K. K. Lee, D. R. Lim, H.-C. Luan, A. Agarwal, J. Foresi, and L. C. Kimerling, “Effect of size and roughness on light transmission in a Si/SiO2 waveguide: Experiments and model,” *Applied Physics Letters*, vol. 77, no. 11, pp. 1617–1619, 2000.

[34] Nanolab, “Plasma enhanced chemical vapour deposition.” ”`http://ntnu.norfab.no/WebForms/Equipment/EquipmentView.aspx?toolId=33`”. Online: accedded 15.03.2016.

[35] A. Gorin, A. Jaouad, E. Grondin, V. Aimez, and P. Charette, "Fabrication of silicon nitride waveguides for visible-light using PECVD: a study of the effect of plasma frequency on optical properties," *Optics Express*, vol. 16, no. 18, pp. 13509–13516, 2008.

[36] Nanolab, "Inductively coupled plasma-reactive ion etching." "`http://ntnu.norfab.no/WebForms/Equipment/EquipmentView.aspx?toolId=39`". Online: accedded 30.03.2016.

[37] Nanolab, "Electron beam lithography." "`http://ntnu.norfab.no/WebForms/Equipment/EquipmentView.aspx?toolId=87`". Online; accessed 06.04.2016.

[38] "Phoenix software: CleWin 5." "`http://www.phoenixbv.com/product.php?prodid=50010105&submenu=dfa&prdgrpID=2&prodname=CleWin%205`". Online; accessed 21.04.2016.

[39] M. A. Mohammad, M. Muhammad, S. K. Dew, and M. Stepanova, *Fundamentals of electron beam exposure and development*. Springer, 2012.

[40] "Elionix electron beam lithography system." "`http://www.elionix.co.jp/english/products/els_f100.html`". Online: accessed 14.05.2016.

[41] "Developer for AR e-beam resists." "`http://www.allresist.com/wp-content/uploads/sites/2/2015/12/allresist_produktinfos_ar600-50_englisch.pdf`". Online; accessed 22.04.2016.

[42] "Remover for AR resists." "`http://www.allresist.com/wp-content/uploads/sites/2/2015/12/allresist_produktinfos_ar600-70-71_300-76-70-72-73_englisch.pdf`". Online; accessed 22.04.2016.

[43] Nanolab, "Scriber, Dynatex DX-iii." "`http://ntnu.norfab.no/WebForms/Equipment/EquipmentView.aspx?toolId=42`". Online: accessed 21.05.2016.

[44] Nanolab, "F20 reflectometer." "`http://ntnu.norfab.no/WebForms/Equipment/EquipmentView.aspx?toolId=10`". Online: accessed 21.05.2016.

[45] A. Z. Subramanian, P. Neutens, A. Dhakal, R. Jansen, T. Claes, X. Rottenberg, F. Peyskens, S. Selvaraja, P. Helin, B. Dubois, *et al.*, "Low-loss singlemode PECVD silicon nitride photonic wire waveguides for 532–900 nm wavelength window fabricated within a CMOS pilot line," *Photonics Journal, IEEE*, vol. 5, no. 6, pp. 2202809–2202809, 2013.

[46] P. Neutens, A. Subramanian, M. U. Hasan, C. Chen, R. Jansen, T. Claes, X. Rottenberg, B. Du Bois, K. Leyssens, P. Helin, *et al.*, "Characterization of PECVD silicon nitride photonic components at 532 and 900 nm wavelength," in *SPIE Photonics Europe*, pp. 91331F–91331F, International Society for Optics and Photonics, 2014.

[47] S. Romero-García, F. Merget, F. Zhong, H. Finkelstein, and J. Witzens, "Silicon nitride CMOS-compatible platform for integrated photonics applications at visible wavelengths," *Optics express*, vol. 21, no. 12, pp. 14036–14046, 2013.

[48] O. Instruments, "PECVD of silicon nitride and oxide." "`https://nanolab.berkeley.edu/process_manual/chap6/6.20PECVD.pdf`". Online: accessed 09.06.2016.

[49] R. J. Bojko, J. Li, L. He, T. Baehr-Jones, M. Hochberg, and Y. Aida, "Electron beam lithography writing strategies for low loss, high confinement silicon optical waveguides," *Journal of Vacuum Science & Technology B*, vol. 29, no. 6, p. 06F309, 2011.

[50] M. Yagnyukova, *Modeling, Fabrication, and Characterization of a Bragg Slot Waveguide with a Cavity*. PhD thesis, University of Toronto, 2013.

[51] J. Wibbeler, G. Pfeifer, and M. Hietschold, "Parasitic charging of dielectric surfaces in capacitive microelectromechanical systems (MEMS)," *Sensors and Actuators A: Physical*, vol. 71, no. 1, pp. 74–80, 1998.

[52] A. Khanna, A. Z. Subramanian, M. Häyrinen, S. Selvaraja, P. Verheyen, D. Van Thourhout, S. Honkanen, H. Lipsanen, and R. Baets, "Impact of ald grown passivation layers on silicon nitride based integrated optic devices for very-near-infrared wavelengths," *Optics express*, vol. 22, no. 5, pp. 5684–5692, 2014.

Appendix A

PECVD recipes

Table A.1: Basic silicon dioxide PECVD process by Oxford Instruments, PLASMALAB SYSTEM 100: *Process data sheet* found

Parameters for SiO_2	Value
SiH_4 [sccm]	8.5
N_2 flow [sccm]	161.5
N_2O flow [sccm]	710
Pressure [mTorr]	1000
RF power [W]	20
RF frequency [MHz]	13.56
Temperature [°C]	300

Table A.2: Improved uniformity/high quality silicon nitride PECVD process by Oxford Instruments, PLASMALAB SYSTEM 100: *Process data sheet*

Parameters for Si_3N_4	HF only process	Pulsed HF/LF process
SiH_4 [sccm]	20	20
NH_3 flow [sccm]	20	20
N_2 flow [sccm]	980	980
Pressure [mTorr]	650	650
RF power (13.56 MHz) [W]	20	20 for 13 sec
RF power (100-300 kHz) [W]	-	20 for 7 sec
Temperature [°C]	300	

Appendix B

ICP-RIE recipes

Table B.1: The etch recipes used in this thesis. Taken from the recipe database on the ICP-RIE computer. OI stands for Oxford Instruments.

Parameter	**(Jens) nitride etch**	**(Peter) Si_3N_4 etch (OI)**
O_2 [sccm]	7	5
CF_4 flow [sccm]	10	5
CHF_3 flow [sccm]	50	30
Chamber pressure [mTorr]	22	22
RF power [W]	175	100
ICP-RIE power [W]	0	100
Helium back flow [Torr]	0	10
Temperature [°C]	20	20

Appendix C

Sample fabrication summary

On the next page, a summary of the fabrication processes of the samples investigated and contributing to the results is presented.

Sample no	SiO2 Recipe	SiO2 Time	Si3N4 Recipie	Si3N4 Time
1	(OPT) SiO2	26 min + 33 s	(OPT) Si3N4	13 min + 8 s
2	(OPT) SiO2	26 min + 34 s	(OPT) Si3N4	13 min + 7 s
3	(OPT) SiO2	26 min + 34 s	(OPT) Si3N4	13 min + 7 s
4	(OPT) SiO2	26 min + 34 s	(OPT) Si3N4	13 min + 7 s
5	(OPT) SiO2	26 min + 34 s	(OPT) Si3N4	13 min + 7 s
6	(OPT) SiO2	26 min + 34 s	(OPT) Si3N4	13 min + 7 s
7	*		(OPT) Si3N4	14 min + 32 s
8	*		(OPT) Si3N4	13 min
9	*		(OPT) Si3N4	13 min + 20 s

Sample no	SiO2 Thickness (middle --> edge)	Si3N4 Thickness	Dose	Beam Current
1	1995 nm --> 2055 nm	208 nm	Exposure by Jens Høvik	
2	1998.4 nm --> 2083 nm		300 µC/cm²	5 nA
3	2004 nm --> 2068 nm			
4	1994 nm --> 2042 nm	Approx. 200 nm	350 µC/cm²	5 nA
5	1999 nm --> 2072 nm			
6	1996 nm --> 2081 nm	Approx 200 nm	350 µC/cm²	5 nA
7		223.5 nm		
8		198.7 nm		
9		204.8 nm		

Sample no	Etch Recipe	Etch Time	Characterisation	
1	(Jens) nitride etch	1 min + 46 s	S(T)EM (208 nm + 2.1 µm)	
2	(Peter) Si3N4 etch (OI)	2 min + 10 s	Too much charge effect	
3				
4	(Peter) Si3N4 etch (OI)	2 min + 33 s		
5				
6	(Peter) Si3N4 etch (OI)	2 min + 33 s	S(T)EM	
7				
8			S(T)EM (200 nm)	
9				

Figure C.1: A summary of the samples further investigated. Approx. means that the reflectometer was not able to measure accurately when having both SiO_2 and Si_3N_4 layers on top of the silicon wafer. (*) No SiO_2 layer on these samples.

Appendix D

COMSOL models

The different COMSOL simulation are presented in the next sections. First, the waveguide cross-section is investigated before using the information from this simulation to simulate the waveguide seen from above.

D.1 Waveguide cross-section simulation

This guide will go through the steps of how to build the model of a waveguide cross-section, where the results will later be used in the simulation of the waveguide seen from above. Words with ”” are names of the features and entries in COMSOL and words in cursive, are parameter names and things named by us like various geometries or materials. After starting COMSOL Multiphysics, we create a new model by choosing the ”Model Wizard” option, see figure D.1. Then we choose ”2D” and this will give a list of different physics options.

For this study we want to work with electromagnetic (EM) waves, select ”Electromagnetic Wave, Frequency Domain under Optics”, under ”Wave Optics”, then click add and study. The next step is to choose which studies we wants to conduct. To find the effective refractive index, we want to do a ”Mode Analysis” study, so we add this and click ”Done”, see figure D.1.

Now we want to define some parameters. The parameters that are used in this study are listed in table D.1. Right click on the ”Global Definitions” entry in the left-hand side model builder and choose parameters from the list. This list will contain the information about the size of the structure, refractive indices and fundamental frequency. Adding these global definitions will make it easier to change for example the geometry at a later time.

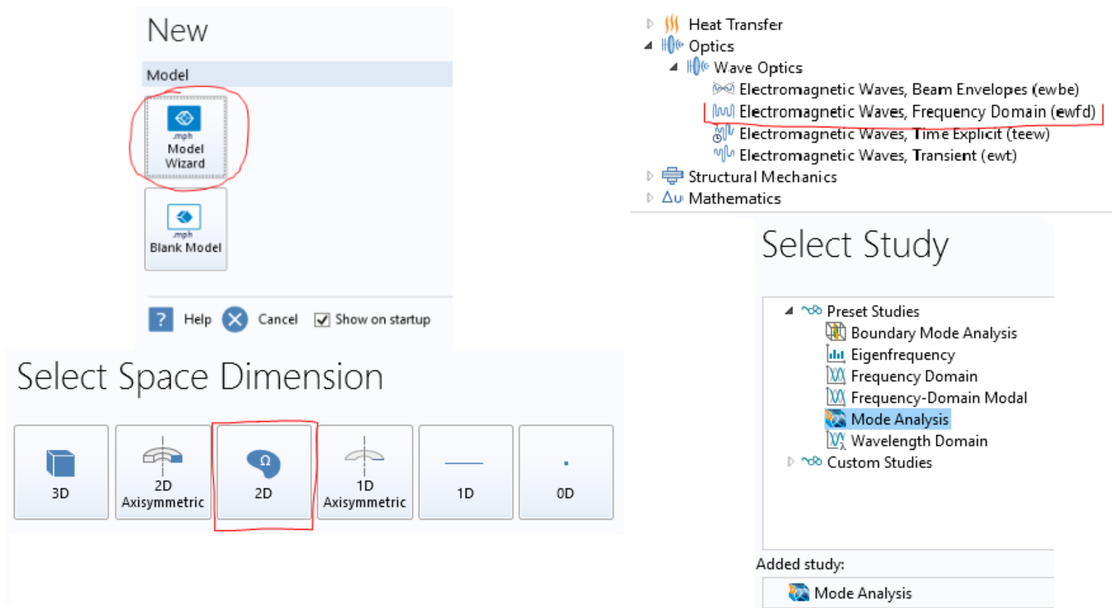

Figure D.1: "New Model" menu and how to choose dimensions, physics model and type of study.

Table D.1: Parameters for the cross section of a waveguide with SiO_2 cladding and a core of Si_3N_4.

Name	**Value or expression**	**Description**
cladding_width	3[um]	The width of the study space
tSi_3N_4	200[nm]	Height of waveguide
tSiO_2	2[um]	Oxide layer thickness
n_SiO_2	1.438	Refractive Index of SiO_2
n_air	1	RI of air
n_Si_3N_4	1.98	RI of Si_3N_4
w_Si_3N_4	500[nm]	Width of waveguide
wl	632.8[nm]	Wavelength
$f0$	c_const/wl	Fundamental frequency

Geometry: After defining the parameters, we can start building the geometry. The structure consist of four rectangles. Right-click on the "Geometry" section and make four rectangles, calling them *Cladding*, *Waveguide*, *Airspace* and *Rectangle 4* as in figure D.2. The first rectangle is the cladding. The *Width* will equal *cladding_width*, and the *Height* = $tSiO_2$, see figure D.3a. For all the rectangles, the position should be "Corner" in the field *Base*. The next rectangle will be the waveguide. This should be positioned in $x = cladding_width/2 - w_Si3N4/2$ and $y = tSiO_2$. Continue to fill in the *width* and *height* with $w_Si_3N_4$ and tSi_3N_4.

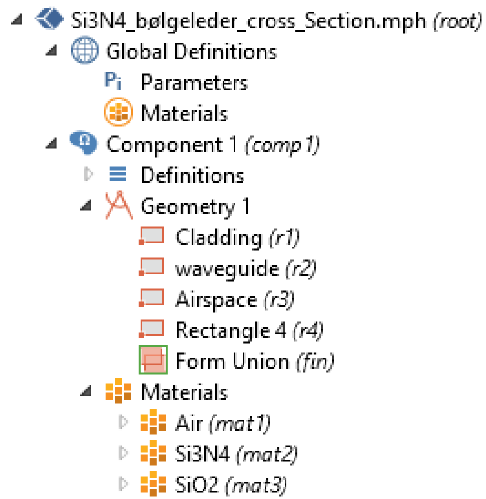

Figure D.2: "Model builder".

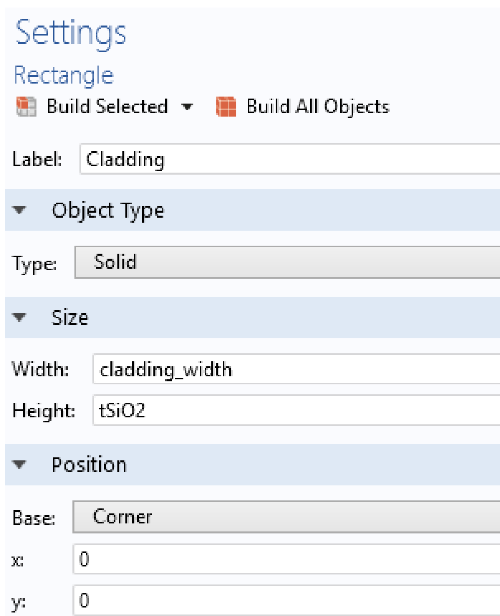

(a) Geometry settings for the study space.

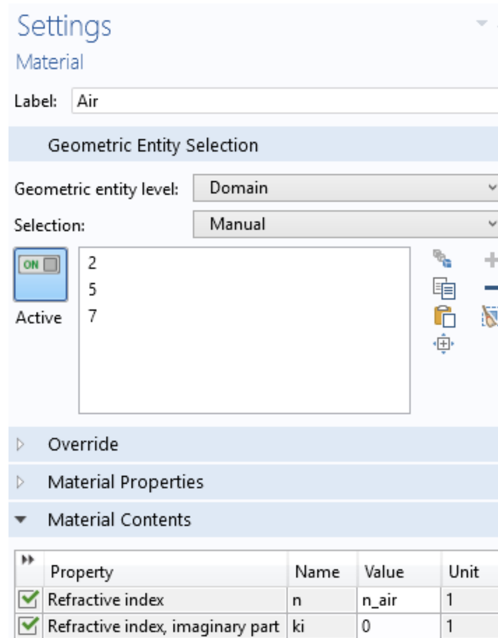

(b) Material settings for air.

Figure D.3: Geometry settings and material settings for air.

The *Airspace* rectangle will be the top cladding above the waveguide. This rect-

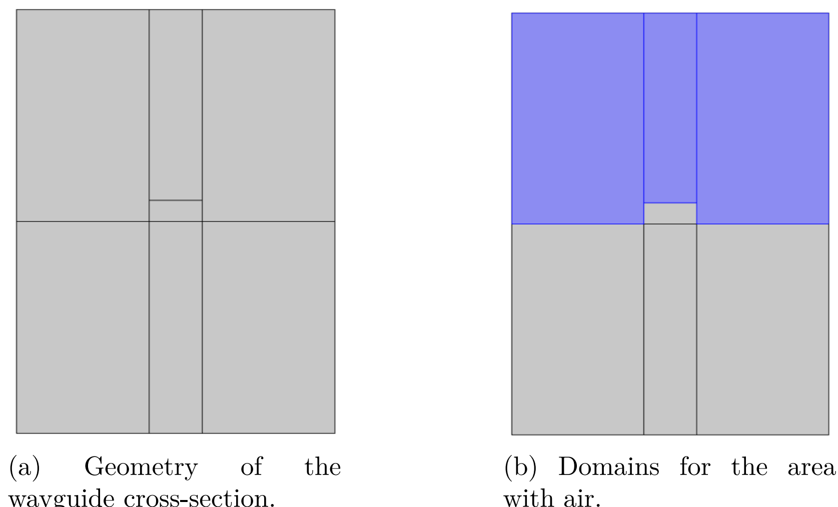

(a) Geometry of the wavguide cross-section.

(b) Domains for the area with air.

Figure D.4: The entire geometry for the waveguide cross-section and the air domains.

angle will look exactly the same at the *Cladding* rectangle except that the y position is set to $tSiO_2$. The last rectangle is just a means to divide the structure into sections. The rectangle will have a *Width* of $w_\mathrm{Si_3N_4}$ and a *Height* of $2 * t\mathrm{SiO_2}$. Here the x position will need to be $cladding_width/2 - w_Si3N4/2$. These four rectangles result in the structure seen in figure D.4a.

Materials: The next step is to add the relevant materials to the correct domains. Right-click the "Materials" entry in the model builder and add three blank materials. Call the first material *Air* and choose domain *2, 5, 7*, see D.4b. Set the refractive index to *n_air* from the table D.1 like in figure D.3b. Do the same with the two other materials, SiO_2 and Si_3N_4(n_si). $\mathrm{Si_3N_4}$ is only present in the rectangle in the middle, the rest in the bottom half of the geometry is $\mathrm{SiO_2}$.

Mesh: We create the mesh. With a finer mesh, we will get a more accurate result. On the other hand, the size of the simulations increase, so we need to take this into account when simulating large structures. The pre-defined "Extremely fine" mesh can be a good choice since none of the structures are very small compared to the wavelength. In this study, a user defined mesh is used to make sure the smaller structures have a more suitable mesh. This is done by changing the "sequence type" to "User-controlled" mesh. Right-click "Mesh" and add a "Free Triangular which will appear beneath the entry "Size" like in figure D.5a. In "Size", choose "Custom" under "General Physics" and fill in the element sizes as required. The

element sizes chosen for the waveguide domain in this study are shown in figure D.5b. Click on ”Free Triangular 1” and add the desired domain, here it is domain *4*. Next, add another ”Size” and a ”Free Triangular”. This will cover the rest of the geometry not included in the first free triangular. Here the predefined ”Extremely fine” is chosen and in ”Free Triangular 2” the ”Geometry entity level” is set to ”Remaining. These settings creates the mesh shown in figure D.6.

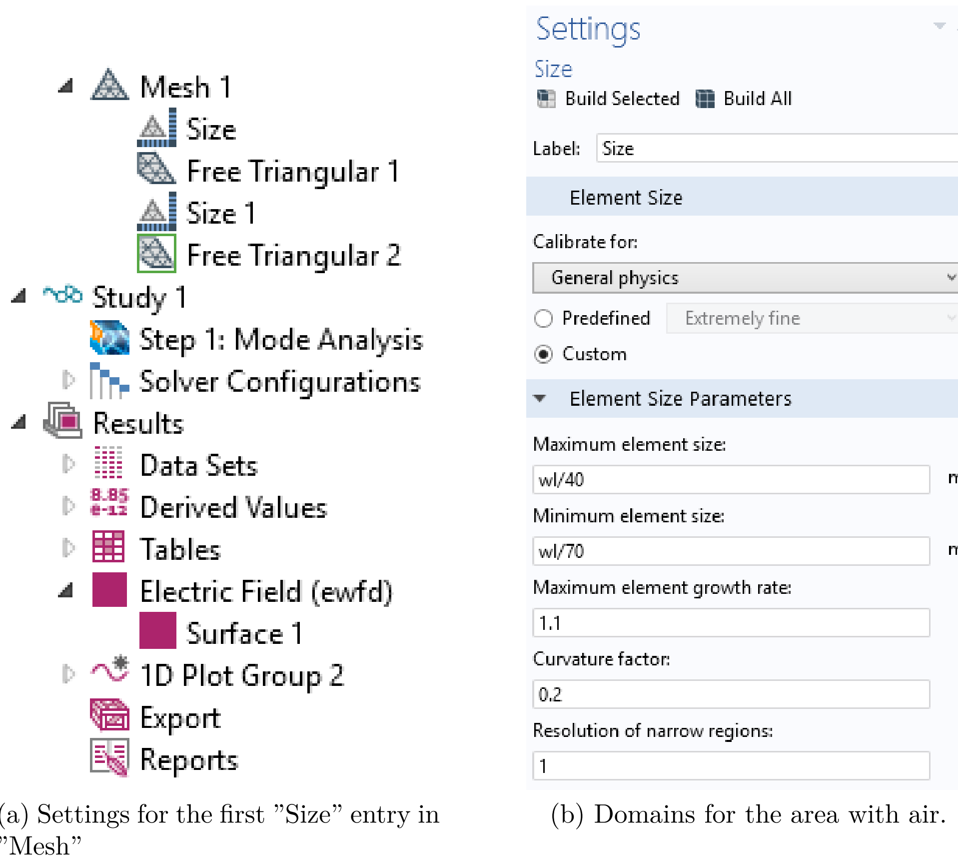

(a) Settings for the first ”Size” entry in ”Mesh”

(b) Domains for the area with air.

Figure D.5: The entire geometry for the waveguide cross-section and the air domains.

Study: In this study we want to find the effective refractive index. In the ”Study” entry in the ”Model Builder”, there should be a ”Mode Analysis” step. Under the ”Mode Analysis” settings, the ”Mode analysis frequency” is set to *f0*, desired number of modes 1 or in this case 10 because it is desired to see if any multi-modes appear in the core. Search around modes is set to 1.8. This is an guess at what

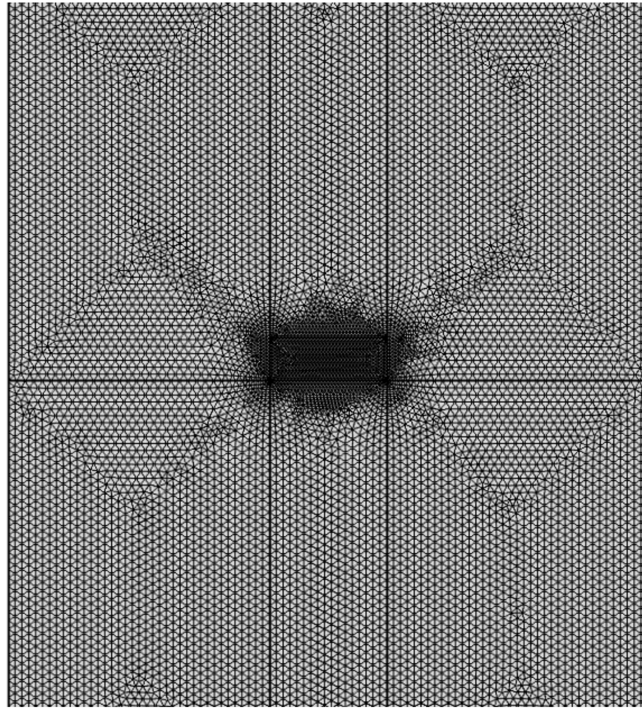

Figure D.6: The mesh created with user settings.

the effective refractive index is, so it will search for modes close to this number. Click on ”Calculate” under ”Study settings”.

D.2 Waveguide simulation with effective index

In this section, a straight waveguide is simulated using the effective index found with the effective index method described in section 3.1.1. Start the same way as for the cross-section simulation in the previous section but when choosing the study, choose "Boundary Mode Analysis" instead. Right click on the "Global Definitions" entry in the left-hand side of the model builder and choose parameters from the list to start defining the refractive indices, sizes and wavelength involved in this simulation. The parameters are listed in table D.2.

Table D.2: The parameters entered in COMSOL for the waveguide simulation.

Name	**Value or Expression**	**Description**
wl	632.8 [nm]	The wavelength
f0	c_const/wl	The fundamental frequency
height	length/2	Height of the study space
length	100 [um]	Length of the waveguide
$n_eff_{2,4,6}$	1.8503	The effective index in the waveguide region
$n_eff_{1,5}$	1.078	The effective index in the air/cladding region
wSi_3N_4	500 [nm]	The width of the waveguide

Geometry: Right-click on the "Geometry" section and make three rectangles, calling them *Studyspace*, *Waveguide* and *Port*. The first rectangle will be the whole study space. The *width* will equal *length* and height has an obvious input-name. We want to add a 5μm layer to the left, right, top and bottom. To add "PML", see the layer drop-down menu far down in the geometry settings. The position should be based in the corner, with $x = 0$, and $y = 0$.

The next rectangle represents the waveguide and the last rectangle is made to define the size of the ports defined later. The settings for the *Waveguide* is found in figure D.7a and the *Port* has the settings found in figure D.7b. When pushing the "Build All Objects" button, the geometry in figure D.8 is created.

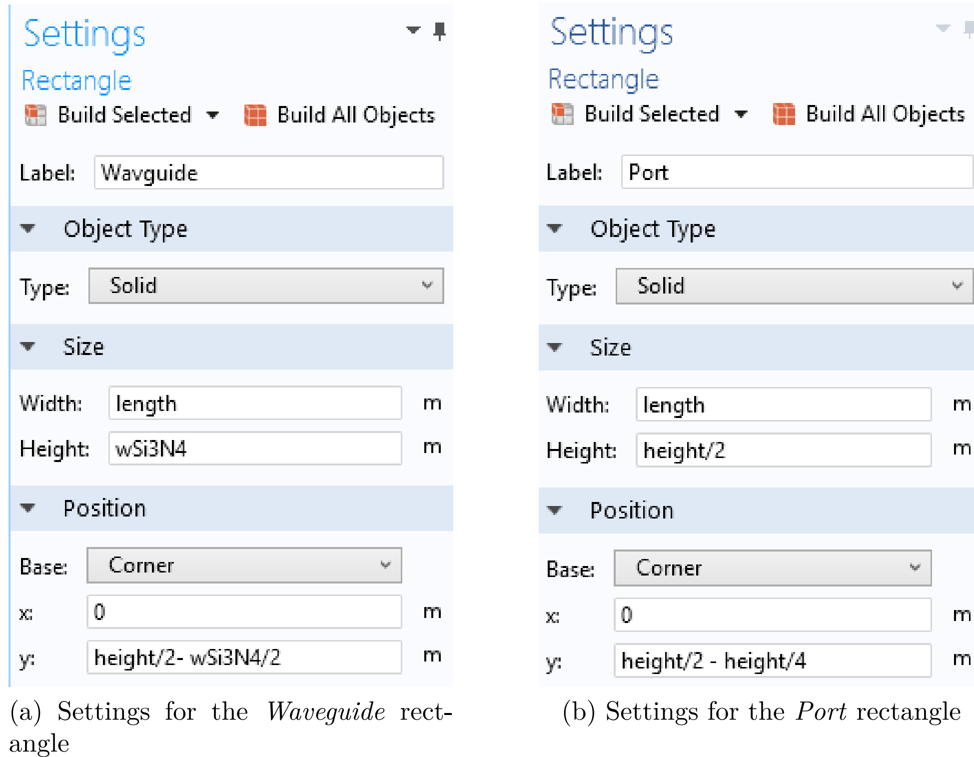

(a) Settings for the *Waveguide* rectangle

(b) Settings for the *Port* rectangle

Figure D.7: The setting for the two rectangles *Waveguide* and *Port* defined under "Geometry".

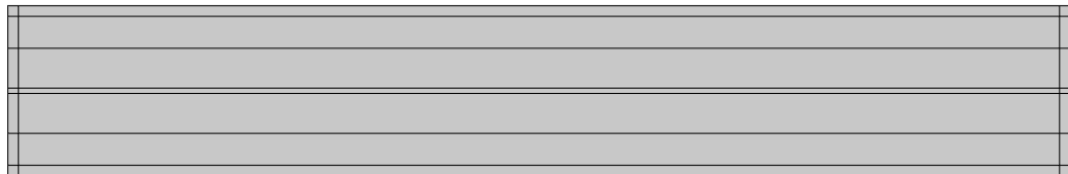

Figure D.8: The complete "Geometry" of the waveguide seen from above.

Materials: The next step is to add the relevant materials to the correct domains. By using equation 3.1.1 defined by the effective index method, the effective indices are found and used in the corresponding areas. The "Surface Integ-

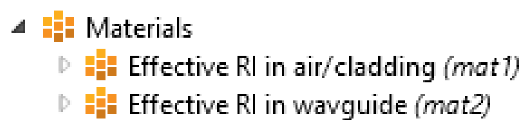

Figure D.9: The "Material" menu in the "Model Builder" showing the two material names for this model.

rals" found in table 6.1 are used in this equation and this results in the effective refractive indices $n_{1,5} = n_{3,7} = 1.078$ and $n_{2,4,6} = 1.8503$ where $n_{1,5}$ means the effective RI found for the area made up of region 1 and 5 in figure 3.1b. Call the two materials *Effective RI in air/cladding* and *Effective RI in waveguide* as seen in figure D.9. The *Effective RI in air/cladding* is the material entered in all domains except the thin waveguide area. Here the effective index for the waveguide is entered.

Ports: Ports are where the electromagnetic wave enters and leaves the simulation space. First, the area not to be included in the simulation needs to be deselected. This is because the ports need to de defined at the simulation boundary. In the physics menu, choose "Electromagnetic Waves Frequency Domain", and deselect the grey area domains in figure D.11. Right-click the same menu and add two "Ports". *Port1* is where the wave will enter the simulation and the waveguide. The port is 9μm in width so that the spot-size of the light is larger than the waveguide spot-size. This is to simulate the spot-size difference between a fibre and a waveguide. Choose boundary *20, 22, 24*, they are found to the left-side of the rectangle called *Port* as seen in figure D.10. Under "Type of port", select *Numeric* and for "Wave excitation at the port", select *On*.

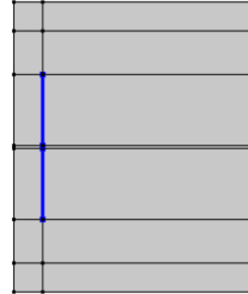

Figure D.10: An illustration of where *Port1* is defined.

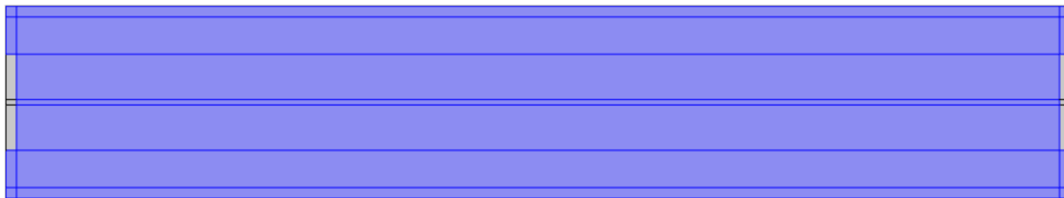

Figure D.11: The grey domains are areas not included in the simulation because the ports need to be defined at the simulation boundary.

Port2 is going to be where the light leaves the waveguide and the simulation. It is placed at the left side of the waveguide opposite *Port1* with domains *35, 37, 39*. Make sure the "Port name" is 2 and "Type of port" is set to *Numeric*. In this port, the "Wave excitation at this port" should be *Off*.

Boundary conditions: We have made an outer layer of 5μm which will be the PML in these simulations. Add these layers by right-clicking the "Definitions" entry under the "Component 1" and add the PML. Choose all outer domains, *1, 2, 6, 7, 8, 14, 15, 16, 20, 21*, leaving out the ones on the outside of the ports.

Mesh: We create the mesh. With a finer mesh, we will get a more accurate result. On the other hand, the size of the simulations get larger, so we need to take this into account when simulating large structures. The pre-defined "Extremely fine" mesh can be a good choice since none of the structures are very small compared to the wavelength. In this study, a user defined mesh is used to make sure the smaller structures have a more suitable mesh. This is done by changing the "sequence type" to "User-controlled" mesh. Right-click "Mesh" and add a "Free Triangular" mesh which will appear beneath the entry "Size" like in figure D.12. In "Size", choose "Custom" under "General Physics" and fill in the element sizes as required. The element sizes chosen for the waveguide domain in this study is shown in figure D.13a. Click on "Free Triangular 1" and add the desired domain, here it is domain *4, 11, 18*. Next, add another "Size" and a "Free Triangular. This will cover the rest of the geometry not included in the first free triangular mesh. Here the predefined "Extremely fine" is chosen and in "Free Triangular 2" the "Geometry entity level" is set to "Remaining".

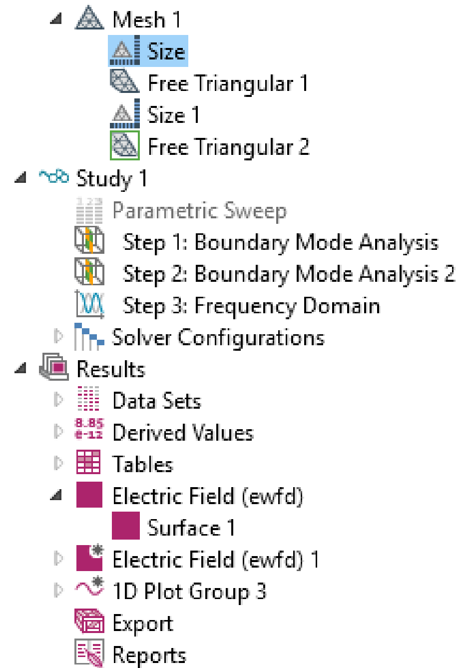

Figure D.12: "Model builder" for "Mesh", "Study" and "Result".

In the "Study" section in the "Model Builder", two sets of "Boundary Mode Analysis are needed as the study has two ports, see figure D.13b. Right-click on "Study" and add a "Boundary Mode Analysis" which is found under "Study Step" → "Other". Also add a study step "Frequency Domain". The first step will have the settings shown in figure D.13c. For the second step, the "Port name" needs to be changed to 2. Here, the "Mode analysis frequency" is also *f0*, "Desired number of modes" is 1, and "Search for modes around" 1.85 which is approximately the effective index in the core. In "Frequency Domain", set the "Frequency" to *f0*.

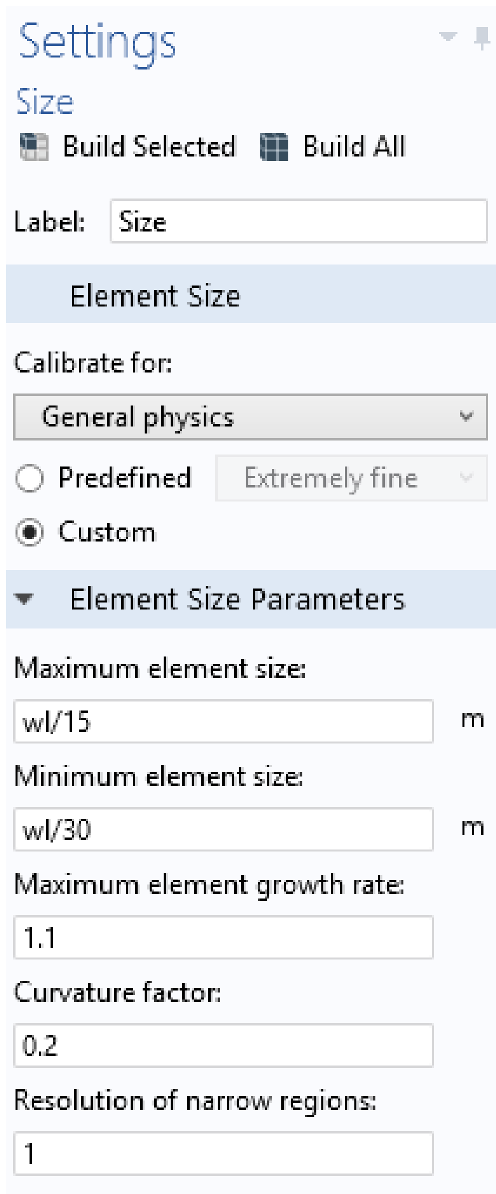

(a) Settings for the first "Size" entry in "Mesh".

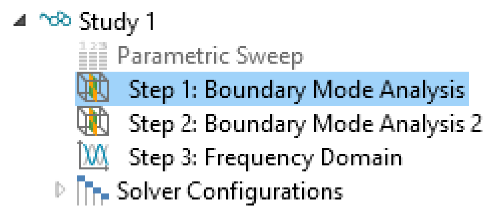

(b) The "Study" menu under "Model Builder".

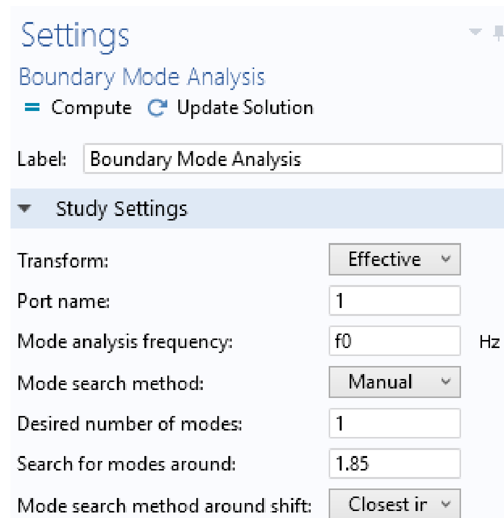

(c) Th "Boundary Mode Analysis" settings for *Port1*.

Figure D.13: The "Size" settings, "Study" entry in "Model Builder" and the settings for "Boundary Mode Analysis" *Port1*.

When all the steps are added and defined, click ”Study” which runs the simulation. Add a ”Parametric Sweep” if it is desirable to simulate different parameters in one simulation.